Development of a single vacuum ultra-violet photon-sensing solution for nEXO

by

Giacomo Gallina

A THESIS SUBMITTED IN PARTIAL FULFILLMENT
OF THE REQUIREMENTS FOR THE DEGREE OF

Doctor of Philosophy

in

THE FACULTY OF GRADUATE AND POSTDOCTORAL
STUDIES
(Physics)

The University of British Columbia
(Vancouver)

April 2021

The following individuals certify that they have read, and recommend to the Faculty of Graduate and Postdoctoral Studies for acceptance, the dissertation entitled:

Development of a single vacuum ultra-violet photon-sensing solution for nEXO

submitted by **Giacomo Gallina** in partial fulfillment of the requirements for the degree of **Doctor of Philosophy** in **Physics**.

Examining Committee:

Prof. Reiner Kruecken, Department of Physics and Astronomy, University of British Columbia, Deputy Director, TRIUMF
Supervisor

Prof. Fabrice Retiere, Department of Physics, Simon Fraser University, Science Technology Department, TRIUMF
Co-Supervisor

Prof. Vesna Sossi, Department of Physics and Astronomy, University of British Columbia
Supervisory Committee Member

Prof. Janis McKenna, Department of Physics and Astronomy, University of British Columbia
Supervisory Committee Member

Prof. Douglas Scott, Department of Physics and Astronomy, University of British Columbia
Supervisory Committee Member

Prof. Scott Oser, Department of Physics and Astronomy, University of British Columbia
University Examiner

Prof. Russ Algar, Department of Chemistry, University of British Columbia
University Examiner

Prof. Daniel McKinsey, Department of Physics, University of California, Berkeley
External Examiner

Abstract

Silicon PhotoMultiplier (SiPM) technology represents an unprecedented attempt to create an ideal solid-state photon detector, combining the low-light detection capabilities of the previous device generations with all the benefits of a solid-state sensor. For this reason, large-scale low-background cryogenic experiments, such as the next-generation Enriched Xenon Observatory experiment (nEXO), are migrating to a SiPM-based light detection system. nEXO aims to probe the boundaries of the standard model of particle physics by searching for neutrino-less double beta decay ($0\nu\beta\beta$) of ^{136}Xe. The nEXO experiment follows the same detection concept as the EXO-200 experiment, but uses 5 tonnes of liquid xenon inside a vacuum cryostat that is expected to be located at SNOLAB, the Canadian underground science laboratory. Decays in the xenon produce both light and ionization and it is important to measure both to achieve sufficient energy resolution and thus background rejection. In particular, electrons from the ionization drift in an applied electric field toward anode pads where they are measured. The light flash is simultaneously detected by an array of SiPMs. The technical goal of the proposed thesis is to study different SiPMs characteristics in order to choose the best SiPM technology for the nEXO experiment. This thesis will also introduce new mathematical models to better understand Geiger mode properties of SiPMs in order to optimize them for the next generations of double beta decay and dark matter experiments.

Lay Summary

Silicon PhotoMultiplier (SiPM) technology represents an unprecedented attempt to create an ideal solid-state photon detector, combining the low-light detection capabilities of the previous generations of devices with all the benefits of a solid-state sensor. The nEXO experiment aims to probe the boundaries of the standard model of particle physics by searching for neutrino-less double beta decay. Different SiPMs characteristics are studied in order to choose the best SiPM technology for this experiment. Moreover, new mathematical models are also introduced to better understand Geiger mode properties of SiPMs to optimize them for the next generations of double beta decay and dark matter experiments.

Preface

The work presented henceforth is original work that was conducted at TRIUMF, the Canadian national laboratory for particle and nuclear physics, located in Vancouver (BC). A version of Chapter 3 has been published in [G. Gallina, and et al. Characterization of the Hamamatsu VUV4 MPPCs for nEXO. Nuclear Instruments and Methods in Physics Research Section A, 940:371–379, 2019. ISSN 01689002.] and in [G. Gallina and F. Retiere. Characterisation of a new generation of VUV low-light sensors. EPJ Web of Conferences, 227, 2020.]. I was the lead investigator, responsible for all the major areas of the experiment, such as setup development, data collection, data analysis and manuscript composition. F. Retiere developed the original setup design and contributed to the data analysis and paper writing. P. Giampa also contributed to the data analysis and paper writing while P. Margetak built the electronics for data taking. The other authors of the papers contributed to the manuscript revision and writing. A version of Chapter 5 has been published in [G. Gallina and et al. Characterization of SiPM Avalanche Triggering Probabilities. IEEE Transactions on Electron Devices, 66(10):4228–4234,2019.]. For this publication I was the lead investigator, responsible for all the major areas of the experiment, such as setup development, data collection, data analysis and manuscript composition. F. Retiere contributed to the derivation of the model, data analysis and paper writing while P. Margetak built the electronic for the data taking and P. Giampa contributed to the paper figures and writing. The other authors of the paper contributed to the manuscript revision and writing. I was the lead investigator for the project presented in Chapter 4, where I was responsible for the development of the setup and for the data analysis. N. Massacret, L. Martin, P. Margetak and R. Maharaj contributed to the development of the software,

hardware and electronic of the setup. F. Retiere contributed to the data analysis. Additionally, I was also the lead investigator for the model presented in Chapter 6. F. Retiere contributed to the model derivation and to the data analysis. M. Mahtab contributed to Fig. 4.2 and Fig. 6.1.

Table of Contents

List of Tables

List of Figures

Glossary

3D B-SiPM 3D integrated Back-side illuminated SiPM

AOI Angle of Incidence

APA Additional Prompt Avalanche

CA Correlated Avalanche

CDA Correlated Delayed Avalanche

CE detector photon Collection Efficiency

CL confidence level

CP charge conjugation parity symmetry

CT CrossTalk

DAQ Data AcQuisition System

DeCT Delayed CrossTalk

DiCT Direct CrossTalk

DN Dark Noise

EXO-200 Enriched Xenon Observatory-200

FBK Fondazione Bruno Kessler

FSRs Field Shaping Rings

FWHM Full Width Half Maximum

LF Low Field

LXe liquid xenon

MC Monte-Carlo model

MIDAS Maximum Integrated Data Acquisition System

MPPC Multi-Pixel Photon Counter

nEXO next-generation Enriched Xenon Observatory

PA Photosensitive Area

PD Photo-Diode

PDE SiPM Photon Detection Efficiency

PE Photo-electron Equivalent

PMNS Pontecorvo–Maki–Nakagawa–Sakata

PMT PhotoMultiplier Tubes

QE Quantum Efficiency

RF Radio-Frequency

RGA Residual Gas Analyzer

RMS Root Mean Square

ROI Region of Interest

SARF Single Avalanche Response Function

SiPM Silicon Photo-Multipliers

SM Standard Model

SPAD Single Photon Avalanche Diode

SPTR Single Photon Timing Resolution

TPC Time Projection Chamber

VERA Vacuum Emission Reflectivity Absorption

VUV Vacuum UltraViolet

Xe xenon

Acknowledgments

I came to Canada 4 years ago to start my Phd at UBC. First of all, I would like to thank Les and Leslie. They welcomed me into their home and made me feel at home. I would then say a big thanks to Maggie. Maggie is a bit *fat* doggy of 4 years old. I came here when she was just a puppy, few months old. I feel now like she is part of my family. I would like to say thanks to her for the endless amount of hours she spent waiting me for little walks, in particular during the months I was studying for the comprehensive exam. I would then say thanks to Digby (the cat) not because I really like him, but otherwise I would feel guilty for the rest of my life. I would then say thanks to Prof. Reiner Kruecken and to Prof. Fabrice Retiere. Reiner because he always helped and supported me during my studies at UBC, Fabrice instead because he allowed me to work in his group and to prove my worth. I think I developed with him, during these years at TRIUMF, a relationship that goes beyond a usual student-supervisor relationship. I would like to say thanks to him for this. I would then say thanks to my colleagues, in particular P. Margetak, N. Massacret, L. Martin, R. Maharaj, P. Giampa, M. Constable and P. Amaudruz, since I drove them crazy with my last minute requests for the last 4 years and, no matter what, they always helped me. I would then say thanks to the Ermenegildo Zegna Founder Scholarship that supported me in paying my tuition fees at UBC. Finally, a heartfelt thanks goes to my parents, my uncle Stefano and my aunt Nadia, and above all to my sister Camilla who supported and encouraged me in all circumstances. Thank you all; you helped make this work better.

Chapter 1

Introduction

It is generally agreed that one of the most promising windows to the properties of neutrinos and a further understanding of their mass would be from the observation of a nuclear decay process known as neutrino-less double beta decay ($0\nu\beta\beta$). This decay can only occur if the neutrino is its own antiparticle, in which case requiring a new mechanism that can give rise to mass [9]. Indeed the observation of ($0\nu\beta\beta$) decay would require lepton number violation and elementary Majorana fermions. This is attractive because the neutrino mass is many orders of magnitude smaller than that of the other fundamental particles of the standard model of particle physics, suggesting some new mechanism is at work and worth searching for [10].

Next-generation liquid xenon (Xe) detectors are emerging as the most promising candidates for neutrinoless double beta decay searches, due to their scalability for very large target masses and potential for extremely low background operations.

Over the last few years, the next-generation Enriched Xenon Observatory (nEXO) collaboration has designed a new tonne-scale ($0\nu\beta\beta$) decay experiment conceived to push the search to the next frontier. Specifically, nEXO aims to probe the boundaries of the standard model of particle physics by searching for ($0\nu\beta\beta$) of ^{136}Xe.

Among the candidate ($0\nu\beta\beta$) nuclei [10], ^{136}Xe is particularly attractive. The ($0\nu\beta\beta$) Q value is high at 2458.07 ± 0.31 keV [9]. Xenon reserves in the atmosphere are practically unlimited and commercial production is sufficient to support

large scale experiments. As a noble gas, isotopic enrichment can be performed efficiently. Xenon is also readily purified of chemical contaminants, resulting in exceedingly low intrinsic radioactive backgrounds [11] and very long electron lifetime [12]. Additionally, as a radiation detector medium, liquid xenon shows high scintillation and charge yield [13]. The high density $\sim 3\ \mathrm{g/cm^3}$ and atomic number ($Z = 54$) result in short attenuation lengths for γ radiation. Finally, the xenon supply can be recycled into upgraded detectors as technology improves.

The current most stringent limit on ($0\nu\beta\beta$) decay in ^{136}Xe is 10.7×10^{25} yr from the KamLAND-Zen experiment, with a corresponding sensitivity exposure of 504 kg $\times$ yr [14]. The diagnostic power of the liquid xenon (LXe) Time Projection Chamber (TPC) allowed the Enriched Xenon Observatory-200 (EXO-200) experiment, the nEXO successful precursor, to reach a competitive sensitivity of 3.7×10^{25} yr with a substantially smaller exposure (178 kg $\times$ yr) and xenon mass (200 Kg) if compared with the KamLAND-Zen experiment [15].

The nEXO detector follows the same concept of the EXO-200 detector, but using 5 tonnes of LXe inside a TPC that is expected to be located at SNOLAB, the Canadian underground science laboratory [2]. At this time the nEXO collaboration is confident that a factor of ~ 25 in the increase of the xenon mass, if compared with EXO-200, represents a natural progression in order to achieve a competitive sensitivity while at the same time relying on a conservative design [2].

The nEXO TPC's multiparameter measurement capability allows the simultaneous determination of event energy, position, site multiplicity, and particle type [10]. Energy loss in xenon produces in fact both light (scintillation) and electron-ion pair (ionization) and it is important to measure both signals to achieve sufficient energy resolution and thus background rejection. In particular, electrons from the xenon ionization drift in an applied electric field towards anode pads where they are measured. Xenon scintillation light is instead detected by an array of Silicon Photo-Multipliers (SiPM)s. In contrast to the widely used PhotoMultiplier Tubes (PMT)s or to the Large-Area Avalanche Photodiodes used in EXO-200, SiPMs are low-voltage powered, optimal for operation at cryogenic temperatures, and have low radioactivity levels with high gain stability over time in operational conditions [16]. For these reasons, not only the nEXO experiment, but also other

large-scale low-background cryogenic experiments, such as DarkSide-20k, are migrating to a SiPM-based light-detection system [17, 18].

The technical goal of the proposed work is to study different SiPMs characteristics in order to choose the best SiPM technology for the light detection in the nEXO experiment. In particular, this work will focus on two aspects that are now under study by the nEXO collaboration: (i) analysis of the characteristics of several SiPMs candidates for nEXO; (ii) Theoretical study of Geiger mode properties (i.e. electric field and noise) of SiPMs. This last aspect will be crucial for the development in the near future of new generations of SiPMs to dramatically improve energy and timing resolution of the next generation of noble liquid detectors.

This work is organized as follows. In Chapter 2 I introduce the physics motivation behind the nEXO experiment. I discuss in particular the design of the nEXO detector, along with the connections with its precursor, the EXO-200 detector. In the same chapter I also present the requirement of the photon-sensor portion of the nEXO experiment and the model used for the estimation of the overall nEXO energy resolution, including the light and charge channel contributions.

In Chapters 3 and 4, I report the characterization of the three most promising SiPMs candidates for nEXO: the Hamamatsu VUV4 MPPC; the FBK VUV HD 1; and FBK VUV HD 3 SiPMs. A significant part of these chapters is devoted to explain the construction of the two setups built for their characterization. Finally, at the end of Chapter 4, I estimate the overall nEXO energy resolution using the data collected in Chapters 3 and 4.

The last two chapters of this thesis (Chapters 5 and 6) are part of a broader study that is not only limited to the nEXO experiment, but it looks forward the next generation of noble liquid detectors. The outcome of this study will be the development of a new back side illuminated SiPM light sensor to dramatically improve energy and timing resolution of future noble-liquid detectors, significantly enhancing their background rejection capabilities relative to the current generation of liquid-based dark matter and double beta decay experiments. More precisely, in Chapters 5 and 6, I discuss the development of a new theoretical framework to better understand and optimize Geiger mode characteristics of SiPMs. In particular, I propose new models that are not only able to explain the wavelength and voltage dependence of the SiPM photon detection efficiency (Chapter 5), but also predict

the voltage and temperature dependence of several noise sources in SiPMs (Chapter 6). These models have been successfully applied to characterize two SiPMs and they can be naturally extended to other SiPMs. Furthermore, they provide key insight into the electric field structure within SiPMs, which can explain the limitation of the existing devices and be used to optimize the performance of the next generation of SiPMs.

Chapter 2

Double beta decay search with the nEXO experiment

2.1 Introduction

Definitive evidence of non-zero neutrino masses from oscillation experiments has been available for nearly two decades [19–22]. However, the incorporation of neutrino masses into the Standard Model (SM) of particle physics remains an open issue [5]. In the SM of particle physics electron (e), muon (μ), tau (τ) and the corresponding neutrinos (ν_e,ν_μ and ν_τ) are spin 1/2 particles that belong to the lepton class. The first three particles are charged (also known as the electron-like leptons) while the last three are neutral. The existence of the neutrino was initially posited in 1930 by Wolfgang Pauli to explain the otherwise missing spin and momentum observed in beta decays and was first detected by Clyde Cowan and Frederick Reines in 1956 [23]. Nevertheless, neutrinos are still poorly known particles. At the moment we know that there are three light neutrinos, much lighter than their charged leptonic partners and they interact weakly with matter [23].

More generally, neutrino phenomenology is described in the SM of particle physics by three quantum flavor states ν_e, ν_μ and ν_τ, coupled to charged leptons via the weak interaction. These states do not have a fixed mass, but they are a quantum mechanic superposition of the three mass eigenstates ν_1, ν_2 and ν_3, with

mass m_1, m_2 and m_3, such that

$$\nu_l = \sum_{i=1}^{3} U_{li}\nu_i \tag{2.1}$$

with $l = e, \mu, \tau$. The transformation between the mass and flavor bases is described by the unitary Pontecorvo–Maki–Nakagawa–Sakata (PMNS) matrix [5]. In the standard parametrization, the PMNS mixing matrix is characterized by: three mixing angles θ_{12},θ_{23} and θ_{13}; a charge conjugation parity symmetry (CP)-violating δ phase; and two possible CP-violating phases λ_2 and λ_3 [3] . Hence we can write

$$U = \begin{pmatrix} c_{12}c_{13} & s_{12}c_{13} & s_{13}e^{-i\delta} \\ -s_{12}c_{23} - c_{12}s_{23}s_{13}e^{i\delta} & c_{12}c_{23} - s_{12}s_{23}s_{13}e^{i\delta} & s_{23}c_{13} \\ s_{12}s_{23} - c_{12}c_{23}s_{13}e^{i\delta} & -c_{12}s_{23} - s_{12}c_{23}s_{13}e^{i\delta} & c_{23}c_{13} \end{pmatrix} D(\lambda_2, \lambda_3) \tag{2.2}$$

with $c_{ab} \equiv \cos\theta_{ab}$, $s_{ab} \equiv \sin\theta_{ab}$ and the matrix D defined as

$$D(\lambda_2, \lambda_3) = \begin{pmatrix} 1 & 1 & 1 \\ 1 & e^{i\lambda_2} & 1 \\ 1 & 1 & e^{i\lambda_3} \end{pmatrix} \tag{2.3}$$

Giving an initial neutrino state ν_l and a final neutrino state $\nu_{l'}$, defined accordingly to Eq. 2.1, the probability for the transition $\nu_l \longrightarrow \nu_{l'}$ in vacuum is given by [3]

$$P(\nu_l \longrightarrow \nu_{l'}) = \left| \delta_{l'l} + \sum_{i \neq k} U_{l'i}(e^{-i\frac{\Delta m^2_{ki} L}{2E}} - 1)U^*_{li} \right|^2 \tag{2.4}$$

where $\Delta m^2_{ki} \equiv (m^2_i - m^2_k)$. L is the distance between the neutrino detector and the neutrino source, and E is the neutrino energy. Equation 2.4 is crucial in neutrino physics because it shows as, in the case of 3-neutrino mixing, neutrinos can transform from one flavor state to another during propagation, giving rise to neutrino oscillation, which remains to date the only observed phenomenon requiring non-zero neutrino masses.

Equation 2.4 depends only on four mixing parameters θ_{12}, θ_{23}, θ_{13} and δ, and on two independent mass squared differences Δm^2_{ki} (Δm^2_{12} and Δm^2_{23}) and not on the

three masses separately. The determination of the three masses is one of the most challenging tasks of contemporary physics and it has fundamental implications not only in particle physics, but also in astrophysics and cosmology [24].

The Δm_{12}^2 and Δm_{23}^2 mass squared differences are often referred as the solar and atmospheric neutrino mass square differences and denoted as Δm_s^2 and Δm_a^2, respectively. Experimentally it has been found that [3]

$$\Delta m_{12}^2 \sim \frac{1}{30}\left|\Delta m_{23}^2\right| \tag{2.5}$$

However the existing data do not allow us to determine the sign of Δm_{23}^2. The two possible signs correspond to the two types of neutrino mass spectrum, generally denoted as :

- Normal hierarchy: $m_1 < m_2 < m_3$
- Inverted hierarchy: $m_3 < m_1 < m_2$

Cosmology is sensitive to the sum of neutrino masses:

$$\Sigma \equiv \sum_i m_i \tag{2.6}$$

for which several upper limits of about 0.1-0.2 eV are set by cosmological observations [25]. Recent experiments also allowed us to constrain the values of Δm_a^2 and Δm_s^2. More precisely, from Super-Kamiokande data Δm_a^2 in the case of a normal (inverted) mass spectrum was found to be [26]

$$1.9(1.7) \times 10^{-3}\mathrm{eV}^2 \leq |\Delta m_a^2| \leq 2.6(2.7) \times 10^{-3}\mathrm{eV}^2 \tag{2.7}$$

at the 90% of the confidence level (CL). From the combined analysis of all the solar neutrino data and the data of the reactor KamLAND experiment, it has been found that Δm_s^2 is given by [27]

$$\Delta m_s^2 = \left(7.50^{+0.19}_{-0.20}\right) \times 10^{-5}\mathrm{eV}^2 \tag{2.8}$$

From this it follows that the neutrino spectrum contains two masses (m_1 and m_2)

separated by the splitting Δm_s^2 (Δm_{12}^2) , and a third mass m_3 separated from the first two by a larger splitting Δm_a^2 (Δm_{23}^2), as also shown in Eq. 2.5 [4].

2.2 Neutrinoless Double Beta Decay

The experimental observation of neutrino oscillations, which requires that neutrinos have mass, indicates that the standard model description of neutrinos must be extended. The introduction of Majorana-type particle fermions provides a theoretically compelling solution to the need to incorporate massive neutrinos into the standard model. The most general mass term can be written in the Lagrangian as [2, 28]:

$$-2\mathscr{L} = m_D \overline{\nu_L} \nu_R + m_D \overline{(\nu_R)^c} (\nu_L)^c + m_R \overline{(\nu_R)^c} \nu_R + \text{h.c.} \tag{2.9}$$

where $(\nu_R)^c$ is the charge-symmetry conjugate of the right-handed neutrino chiral projection and (ν_L) is left-handed chiral projection. m_R and m_D are two mass terms. The last equation can be written in matrix form as:

$$-2\mathscr{L} = \left(\overline{\nu_L}, \overline{(\nu_R)^c} \right) \begin{pmatrix} 0 & m_D \\ m_D & m_R \end{pmatrix} \begin{pmatrix} (\nu_L)^c \\ \nu_R \end{pmatrix} + \text{h.c.} \tag{2.10}$$

The physical masses are the eigenvalues of the 2×2 mass matrix of the previous equation, as given by:

$$m_\pm = \frac{1}{2} \left(m_R \pm \sqrt{m_R^2 + 4m_D^2} \right) \tag{2.11}$$

Further making the assumption that $m_R >> m_D$, $m_\pm$ result in the following values:

$$|m_-| = \frac{m_D^2}{m_R} \tag{2.12}$$

$$|m_+| = m_R \left(1 + \frac{m_D^2}{m_R^2} \right) \sim m_R \tag{2.13}$$

This would explain both the absence of observational evidence for a heavy, right-handed neutrino and the suppression of the m_- mass. If we choose the mass

scale for m_R to be $10^{14} - 10^{16}$ GeV, and m_D to be 100 GeV, we obtain a value for m_- residing roughly in the observed neutrino mass splitting range of $\sim 1 - 100$ meV [29, 30]. This effect of a very massive, right-handed neutrino state driving down the mass of the left-handed neutrino state is colloquially referred to as type-I see-saw mechanism and it is generally considered the most economical possibility [31]. According to this mechanism, small neutrino masses are explained by new interac-

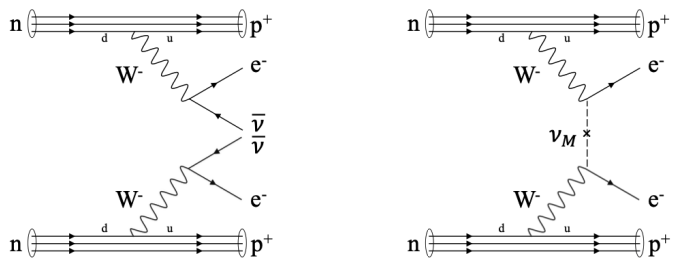

Figure 2.1: Feynman diagrams representing two-neutrino double beta ($2\nu\beta\beta$) decay (left) and neutrinoless double beta ($0\nu\beta\beta$) decay (right), as shown in Ref. [2]. The ($2\nu\beta\beta$) decay process conserves both baryon and lepton number separately. The ($0\nu\beta\beta$) decay process instead is explicitly a leptogenic process, creating two outgoing leptons. It is only possible if neutrinos are Majorana-type particles.

tions beyond the standard model of particle physics which violates the total lepton number and, consequently, the lepton number violating neutrinoless double-beta decay process ($0\nu\beta\beta$) of even–even nuclei is allowed[1] [34]

$$ {}^{A}_{Z}\mathrm{X} \Longrightarrow {}_{Z+2}^{A}\mathrm{Y} + 2e^- \tag{2.14} $$

where A and Z are the numbers of nucleons and protons in the parent nucleus X of mass M_X. Here Y is instead the daughter nucleus with mass M_Y and number of nucleons and protons equal to A and $Z+2$, respectively.

[1]The Type-I see-saw mechanism for neutrino mass generation is only one of the many possibilities that could produce a $0\nu\beta\beta$ decay. Other theoretical prescriptions include Type-II (scalar (Higgs) triplet) and Type-III (fermionic triplet) see-saw mechanisms [32]. An additional set of contributions to $0\nu\beta\beta$ could also arise by relaxing the assumption that the scale where lepton number is violated is well above the electroweak scale [33].

Figure 2.1 shows not only the Feynman diagram representing the lepton violating process ($0\nu\beta\beta$), but also the Feynman diagram for the lepton conserving two-neutrino double beta decay process ($2\nu\beta\beta$), represented by

$$ {}^{A}_{Z}\mathrm{X} \Longrightarrow {}_{Z+2}^{A}\mathrm{Y} + 2e^{-} + 2\bar{\nu} \tag{2.15} $$

As clear from Eq. 2.14, the measurement of a $0\nu\beta\beta$ decay would immediately demonstrate the existence of lepton number violation. In addition, its observation would confirm the existence of Majorana neutrinos, regardless of the decay mechanism [35]. Such a discovery would be a fundamental departure from the picture provided by the standard model of particle physics, as all experimental measurements to date have shown lepton number to be a conserved quantity.

2.2.1 Connections with Cosmology

Antimatter is rare in the universe. The Big Bang should have created equal amounts of matter and antimatter in the early universe [36, 37]. But today, everything we see is made almost entirely of matter. There are three basic ingredients necessary to allow for the evolution of a matter dominated universe from an initially symmetric state [38]:

- Baryon Number Violation: There must be a violation of the Baryon number (B).

- C and CP violation: Even in the presence of B-non conserving interactions, a baryon asymmetry will not develop unless both C (charge conjugation) and CP (charge conjugation combined with parity) are violated. In the absence of a preference for matter or antimatter, B-non conserving reactions will produce baryon and antibaryon excesses at the same rate, thereby maintaining zero net baryon number.

- Non-Equilibrium Conditions: In chemical equilibrium the entropy is maximal when the chemical potentials associated with all non-conserved quantum number vanish. Further, particles and antiparticles masses are guaranteed to be equal by the CPT invariance (charge, parity, and time reversal symmetry).

The conditions were proposed by Andrei Sakharov [39]. Modern physics research has shown that all three conditions can be present in the frameworks of the standard model [2].

For example, early experimental work studying Parity (P) symmetry violation in weak decays in 1957 implied the presence of a C-symmetry violation through a theorem from Lee and Yang. Later in 1964 studies of the neutral K-mesons showed the existence of CP-symmetry violation. Together these existing observations demonstrated, for example, as the second of Sakharov's three conditions is also present in nature. However, experimental research on K-mesons showed as the magnitude of the CP-violation present in K-meson systems was not sufficient to explain the matter-antimatter asymmetry of the universe [40].

Thus the search continues for a process to fulfill the requisite magnitude of CP-violation, potentially in some other area of the SM, such as the lepton sector, where neutrinos remain less than fully understood. In fact, the last two decades of developments in neutrino physics research have revealed a number of intriguing results. The simple, mass-less neutrinos of the SM have actually been found to be massive particles and potentially contain CP violation hidden within the complete formal description of flavor-oscillating massive neutrinos.

Additionally, neutrinos will also provide clues to the matter-antimatter asymmetry in the universe.

While, in fact, different possibilities exist to create such an asymmetry, the most popular scenario is baryogenesis via leptogenesis, as it allows to additionally address open questions of neutrino physics like the mechanism of neutrino mass generation and mixing [36]. The two common approaches are via: (i) leptogenesis from out-of-equilibrium decays, (ii) leptogenesis from oscillations.

In the first approach, in order to feature small enough neutrino masses and at the same time a large enough baryon asymmetry, the right handed neutrino mass is bounded from below [41].

In this type of leptogenesis an asymmetry is created by violating out-of-equilibrium decays of new heavy degrees of freedom that provide a new source of CP violation. As long as these decays generate a net asymmetry above the electroweak scale baryogenesis via leptogenesis becomes possible. The CP violation relevant for baryogenesis is usually parameterized by the CP asymmetry ε per de-

cay of heavy particles. In some leptogenesis models ε is proportional to the masses of both, the light neutrinos and the heavy ones. Given the tiny value of light neutrino masses (compared to the electroweak scale), the leptogenesis scale set by the mass of the heavy neutrinos has to be very high in order to generate a large enough lepton asymmetry [36].

In the second approach, instead, while the total lepton number is approximately conserved, flavor oscillations create an asymmetry in between the different flavor sectors [42]. The singlets that are in thermal equilibrium are able to transfer their asymmetry to the active neutrino sector and thus create a baryon asymmetry [36].

A number of experiments will explore the lepton flavor sector with more accuracy in the future. Particularly important are: (i) Neutrino oscillation experiments; (ii) Neutrinoless double beta decay searches [36]. The first kind of experiments will search for leptonic CP violation in light neutrino mixing. The oscillation probabilities are sensitive to the light neutrino mixing angles, mass differences and the CP phase: δ, of the PMNS matrix (Eq. 2.2). Although existing accelerator neutrino experiments such as T2K and NOνA are sensitive to δ, their sensitivity is rather limited and will be improved significantly in the future with the experiment DUNE [43].

Double beta decay experiments instead will perform measurements sensitive to low-scale seesaw scenarios as the heavy neutrinos can give a significant contribution to the amplitude for masses below 1 GeV.

2.2.2 Decay rate and half life of the $0\nu\beta\beta$ decay

The experimentally observable measurement for the $0\nu\beta\beta$ search is its decay rate, which is proportional to the inverse of its half-life time. Assuming that this process is induced by Majorana neutrino masses and mixing the $0\nu\beta\beta$ decay rate is given by [3]

$$\Gamma^{0\nu} \equiv \left(\frac{1}{T_{1/2}^{0\nu}}\right) = G^{0\nu}(Q,\mathrm{Z})|M^{0\nu}|^2 \frac{|m_{\beta\beta}|^2}{m_e^2} \tag{2.16}$$

where $G^{0\nu}(Q,\mathrm{Z})$ is the known integral over the phase space that depends on Z (the number of protons in the parent nucleus) and on the reaction Q-value. This last

quantity is defined as the total energy released in the nuclear decay process and it is equal to $Q \equiv (M_X - M_Y - 2m_e)$ with m_e the electron mass. $|M^{0\nu}|$ is the nuclear matrix element. The numerical values of $G^{0\nu}(Q,\mathrm{Z})$, Q and the natural abundance of

$\beta\beta$-decay	$G^{0\nu}$ [10^{-14} y^{-1}]	Q [keV]	Nat. abund. [%]	Experiments
$^{48}\mathrm{Ca} \to {}^{48}\mathrm{Ti}$	6.3	4273.7	0.187	CANDLES
$^{76}\mathrm{Ge} \to {}^{76}\mathrm{Se}$	0.63	2039.1	7.8	GERDA, Majorana
$^{82}\mathrm{Se} \to {}^{82}\mathrm{Kr}$	2.7	2995.5	9.2	SuperNEMO, Lucifer
$^{100}\mathrm{Mo} \to {}^{100}\mathrm{Ru}$	4.4	3035.0	9.6	MOON, AMoRe
$^{116}\mathrm{Cd} \to {}^{116}\mathrm{Sn}$	4.6	2809	7.6	Cobra
$^{130}\mathrm{Te} \to {}^{130}\mathrm{Xe}$	4.1	2530.3	34.5	CUORE SNO+
$^{136}\mathrm{Xe} \to {}^{136}\mathrm{Ba}$	4.3	2461.9	8.9	EXO, KamLAND-Zen, NEXT, XMASS
$^{150}\mathrm{Nd} \to {}^{150}\mathrm{Sm}$	19.2	3367.3	5.6	DCBA/MTD

Figure 2.2: Values of $G^{0\nu}(Q,\mathrm{Z})$, Q and natural abundance of the initial isotope for several $0\nu\beta\beta$ decay processes [3].

nuclei for which the $0\nu\beta\beta$ decay is theoretically allowed are presented in Fig. 2.2. The quantity $m_{\beta\beta}$ is instead the effective Majorana mass defined as

$$m_{\beta\beta} \equiv \sum_i U_{ei}^2 m_i \tag{2.17}$$

This last quantity, in addition to the nuclear matrix element $|M^{0\nu}|$, is a crucial parameter, since the measurement of the half-life of the $(0\nu\beta\beta)$-decay, according to Eq. 2.16, gives the product of the effective Majorana mass with the nuclear matrix element $|M^{0\nu}|$ and not only the effective Majorana mass [3].

Fig. 2.3 shows the value of the nuclear matrix element computed with several numerical models. It is evident that there is a large discrepancy between values of $|M^{0\nu}|$ computed with different models. The nuclear matrix element computation is therefore still an open field of research. The strongest limits on the half-life of the $0\nu\beta\beta$ decay rate are from the KamLAND-Zen and GERDA experiments, giving at 90% CL for two different isotopes [5]

$$T_{1/2}\left({}^{136}\mathrm{Xe}\right) > 10.7 \times 10^{25}\ \mathrm{yr} \tag{2.18}$$

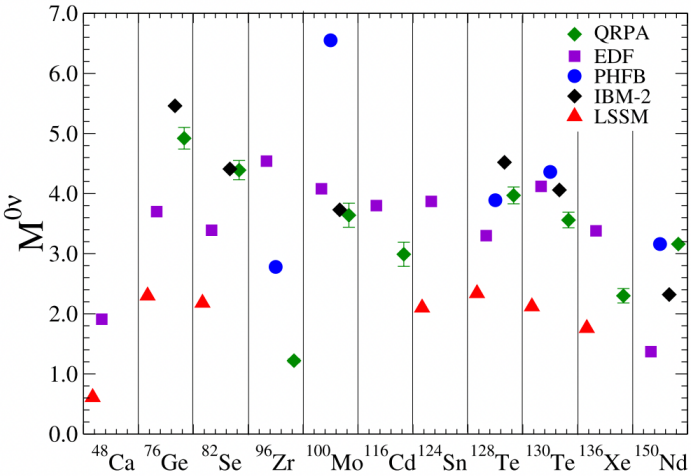

Figure 2.3: Values of the nuclear matrix element calculated with different numerical models. QRPA represents the Quasi-particle Random Phase Approximation. EDF is the Energy Density Functional method. PHFB is the Projected Hartree–Fock–Bogoliubov approach. IBM-2 is the Interacting Boson Model-2 and LSSM is the Large-Scale Shell Model. For more details see Ref. [3].

and [44]

$$T_{1/2}\left(^{76}\mathrm{Ge}\right) > 5.3 \times 10^{25}\ \mathrm{yr} \tag{2.19}$$

respectively.

Generally, the effective Majorana mass is examined as a function of the lowest neutrino mass, as shown in Fig. 2.4, for the two different neutrino mass hierarchies (normal or inverted) introduced in Sec. 2.1. Uncertainty in the parameters of Eq. 2.17 produces in Fig. 2.4 allowed bands (green and red) under the assumption that neutrinos are Majorana particles.

The current generation of $0\nu\beta\beta$ decay experiments are probing $|m_{\beta\beta}|$ down to 100 meV. Figure 2.4 also shows the target sensitivity level for the next generation $0\nu\beta\beta$ decay experiments, which is roughly $|m_{\beta\beta}| \sim$15 meV [2].

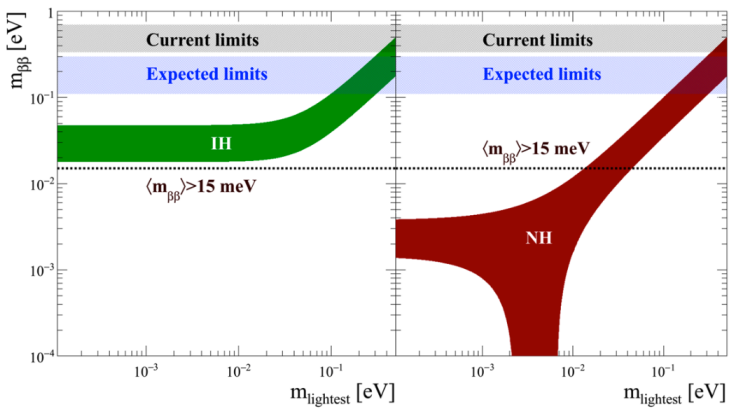

Figure 2.4: Effective neutrino mass as a function of the mass of the lightest neutrino. Current limits and expected limits from past and ongoing experiments are shown as grey and blue horizontal bands. The green (for inverted hierarchy) and red (for normal hierarchy) bands show the expected ranges under the assumption that neutrinos are Majorana particles. Next-generation tonne-scale experiments aim to probe the effective Majorana neutrino mass down to 15 meV, shown as a horizontal dashed line [2].

2.2.3 Energy signature of $0\nu\beta\beta$ decay

In addition to its half-life, the most important experimental signature for a $0\nu\beta\beta$ decay is a mono-energetic peak in the measured electron energy spectrum at the Q-value of the decay, produced when the two electrons emitted in the process are both absorbed in the detector active volume, as shown in Fig. 2.5. The electron energy is therefore the main observable for the discovery of the $0\nu\beta\beta$ decay [5]. This feature allows us to separate $0\nu\beta\beta$ from $2\nu\beta\beta$ events, even if the corresponding decay rate for the $0\nu\beta\beta$ mode is much smaller than the one for the $2\nu\beta\beta$ mode.

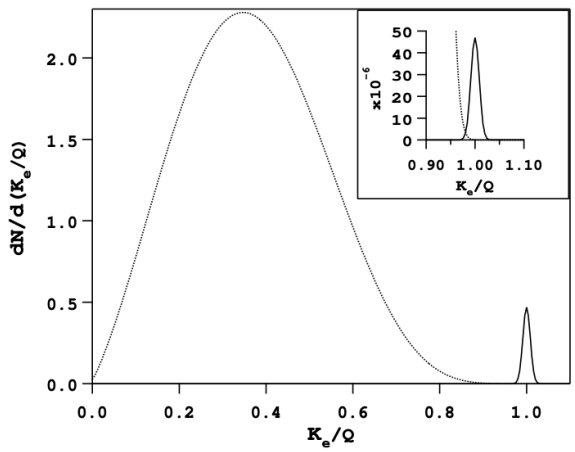

Figure 2.5: Electron energy spectrum for the $0\nu\beta\beta$ decay mode and for the $2\nu\beta\beta$ decay mode. The figure also includes the effect of a 2% energy resolution smearing [4].

2.2.4 Discovery potential for next generation $0\nu\beta\beta$ decay experiments

The number of detectable $0\nu\beta\beta$ decays ($N_{0\nu\beta\beta}$) occurring in a mass m of an element containing a candidate $0\nu\beta\beta$ isotope of half-life $T_{1/2}$ follows as [5]

$$N_{0\nu\beta\beta} = \frac{\ln 2 \cdot N_A \cdot \varepsilon}{M_{\beta\beta} T_{1/2}^{0\nu\beta\beta}} \tag{2.20}$$

where N_A is Avogadro's number, $M_{\beta\beta}$ is the molar mass of the target isotope, and $T_{1/2}$ is the half-life of the decay. ε is often called sensitive exposure and it is given by

$$\varepsilon \equiv \{a \cdot m \cdot \varepsilon_{\text{live}} \cdot \varepsilon_{\text{det}} \cdot t\} \tag{2.21}$$

where a is the isotopic abundance (the enrichment), ε_{det} is the detector detection efficiency in the energy Region of Interest (ROI) (Fig. 2.5) to observe $0\nu\beta\beta$ decay events, and t is the elapsed observation time with a detector live-time fraction of

$\varepsilon_{\text{live}}$ [2][2]. The number of background events in the ROI can be written as [5]

$$N_{bkg} = B \cdot \varepsilon \tag{2.22}$$

where B is often called sensitive background and represents the number of background events in the ROI region divided by ε, defined in Eq. 2.21. Sensitive exposure and sensitive background can then be used to estimate, using a likelihood method [5, 45], the discovery sensitivity of old and next generation $0\nu\beta\beta$ experiments, as reported in Figs. 2.6 and 2.7. More precisely, Fig. 2.7 plots the projected

Experiment	Isotope	Exposure (kg·yr)	$T_{1/2}^{0\nu\beta\beta}$ sensitivity (yrs)	$T_{1/2}^{0\nu\beta\beta}$ limit (yrs)	$\langle m_{\beta\beta} \rangle$ limit (eV)
EXO-200	^{136}Xe	177.6	3.7×10^{25}	$> 1.8 \times 10^{25}$	$< 0.15 - 0.40$
KamLAND-Zen	^{136}Xe	504	5.6×10^{25}	$> 10.7 \times 10^{25}$	$< 0.06 - 0.17$
GERDA	^{76}Ge	46.7	5.8×10^{25}	$> 8.0 \times 10^{25}$	$< 0.12 - 0.26$
MAJORANA DEMONSTRATOR	^{76}Ge	9.95	2.1×10^{25}	$> 1.9 \times 10^{25}$	$< 0.24 - 0.52$
CUORE	^{130}Te	86.3	0.7×10^{25}	$> 1.3 \times 10^{25}$	$< 0.11 - 0.52^{b}$

Figure 2.6: Experimental parameters for the older generation $0\nu\beta\beta$ experiments, with details on their sensitive exposure ε, half life sensitivity, half life limit (represented as $T_{1/2}^{0\nu\beta\beta}$) and effective mass limit $m_{\beta\beta}$ [2] .

discovery sensitivity for a number of selected experiments as a function of ε and B. The discovery sensitivity was defined in Ref. [5] to be the value of $T_{1/2}^{0\nu\beta\beta}$ or $m_{\beta\beta}$ for which an experiment has a 50% chance to measure a signal above background with a significance of at least 3σ. The computation was performed for $T_{1/2}^{0\nu\beta\beta}$ and the result converted to a range of $m_{\beta\beta}$ values by using Eq. 2.16. The experiments in Fig. 2.7 are divided accordingly to the candidate isotopes used for the $0\nu\beta\beta$ search. Uncertainty in the nuclear matrix element is represented as bands. Past or current experiments with published background level and energy resolution (red marks) are shown according to the average performance in their latest data taking

[2]Note as m and $M_{\beta\beta}$ are significantly different. m, in fact, represents the total mass of the element (Xe, for example), measured in kg, while $M_{\beta\beta}$ is the molar mass of the enriched isotope (^{136}Xe, for example), measured in kg/mol. Xenon, for example, can be enriched to significantly high level, up to 90% ($a = 0.9$) and it is one of the best candidates for $0\nu\beta\beta$ searches, see Fig. 2.2.

phase. Among several experiments, the next-generation Enriched Xenon Observa-

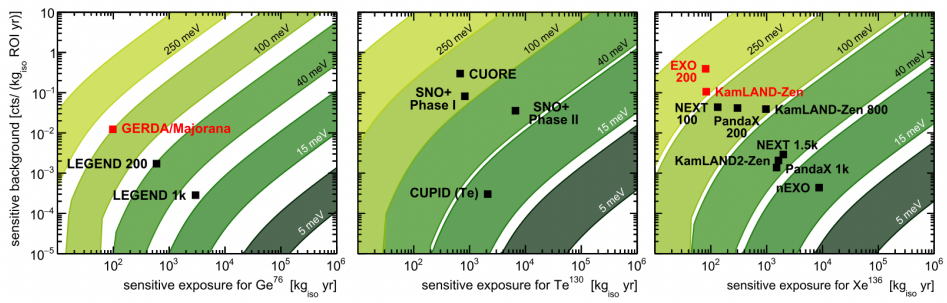

Figure 2.7: Projected discovery sensitivity as a function of the sensitive exposure ε and sensitive background B for three candidate isotopes for $0\nu\beta\beta$ search [5]. Uncertainties in the nuclear matrix elements are represented as bands. Past or current experiments with published background level and energy resolution (red marks) are shown according to the average performance in their latest data taking phase.

tory experiment (nEXO) is the only Xe-based next generation experiment able to probe the effective Majorana mass down to $\sim$ 15 meV.

2.3 Liquid xenon for $0\nu\beta\beta$ search

LXe (boiling point: 165.03 K, melting point: 161.36 K) is a particularly attractive candidate for $0\nu\beta\beta$ search for several reasons [28].

- It serves as the source of the decay and as the detector.
- It can be isotopically enriched to very high levels.
- Its high atomic mass and density make it efficient at stopping gamma backgrounds (this property is often called self-shielding).
- Being a liquid, it allows to build monolithic detectors.
- It can be reliably purified to facilitate long electron lifetimes.
- There are no long-lived radioactive isotopes of Xe produced via activation from cosmogenic sources.

- Scintillation and ionization are anti-correlated in LXe, and this can be used to achieve good energy resolution.

The response of LXe to ionizing radiation has been studied extensively in the literature, both experimentally [13] and numerically [7].

Energy loss in xenon produces both light (scintillation) and electron-ion pair (ionization) and it is important to measure both signals to achieve sufficient energy resolution and thus background rejection. The ionization point can be precisely measured by incorporating the LXe in a TPC [46].

More generally, when particles deposit their energy in LXe, they produce a number of electron-ion pairs and excited xenon atoms often called "excitons". In

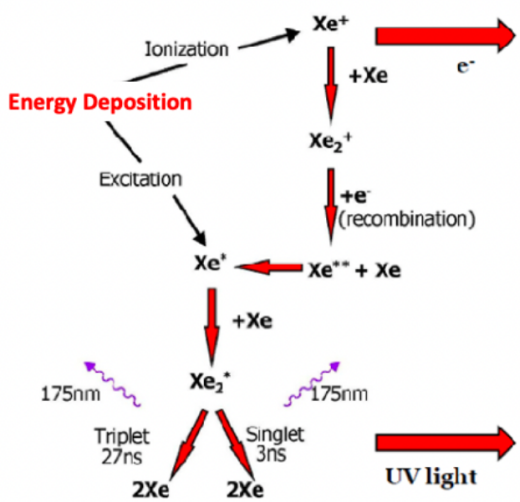

Figure 2.8: Ionization and scintillation processes in liquid xenon [2].

the scintillation process, two routes are then possible: either direct excitation of the Xe atoms or electron-ion recombination.

The resulting Xe^+ ions and Xe^* atoms recombine with other Xe atoms to form excited molecules (Xe_2^*) that decay emitting 175 nm Vacuum UltraViolet (VUV) photons (174.8 ± 10.2 nm [47]). Due to this fast decay time, the majority of the

scintillation signal is collected by the TPC photon-light sensors within 100 ns from the original energy deposition.

The final ratio of light over charge is strongly dependent on the type of particle that interacts with the liquid xenon, allowing particle identification. Alphas generate much more light than betas/gammas due to their higher density of ionization, resulting in larger amounts of recombination. As an example, a 2.5 MeV beta/gamma event generates about 104 k photons and 125 k electrons, while a 5 MeV alpha event generates about 350 k photons and 10 k electrons in an electric field of 400 V/cm [8]. The relative number of electrons and photons produced by an energy deposition not only depends on the type of particle, but also on the electric field applied to the TPC. This property was first measured in Ref. [48]. As the electric field increases in the TPC, more ionized electrons can be drifted away from the interaction site, reducing the number of photons produced through recombination. This anticorrelation between the light and charge channel can be used as a pow-

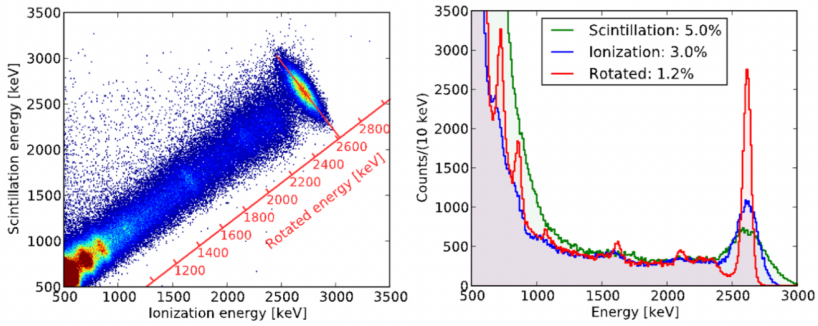

Figure 2.9: Energy of events as measured by the ionization and scintillation channels while using a ^{228}Th calibration source in the EXO-200 detector, the precursor of the nEXO detector. The energy resolution is considerably improved by forming a linear combination of both measurements [2, 49].

erful tool to dramatically improve the energy resolution, since it allows to linearly combine the information provided by the light and charge channels reducing therefore the fluctuations of the two channels while considered individually, as shown in Fig. 2.9 [48, 49].

In addition to this property, LXe is also ideal for the implementation of background rejection strategies. Shielding the inner detector from the energy deposition of other particles that constitute its natural background is crucial for an effective $0\nu\beta\beta$ search. Discrimination of $0\nu\beta\beta$ events from gammas coming from the ^{222}Rn decay chain is the key for the success of most of the $0\nu\beta\beta$ experiments. External gammas are in fact the dominant background source and they can deposit an energy near the Q-value of the $0\nu\beta\beta$ [50]. Gammas tend to Compton scatter, so they can produce more multiple energy deposition (multi-site) events than single energy deposition (single-site) events. Moreover, even for single-site events, there are differences between the ionization electron cloud topology produced by gammas and beta particles (used instead for $0\nu\beta\beta$ identification). An additional way to discriminate gamma particles in LXe is to reconstruct their original position of energy-deposition. Gamma rays with an energy comparable to the Q-value of the $0\nu\beta\beta$ decay in fact have an attenuation length in LXe smaller than 8.7 cm [28]. This means that a large enough LXe detector would have an inner volume isolated from external gamma rays. Therefore, all gammas interactions that happen close to the detector edges can be suppressed with fiducial-volume cuts.

This last property, usually called self-shielding, is due to the high atomic mass, density and homogeneity of LXe and it is crucial for $0\nu\beta\beta$ searches with LXe TPCs. It will be used, in addition to the measurement of the cloud charge size, as a powerful background rejection strategy in several next generation xenon based experiments. Additionally, it has already been successfully implemented in the EXO-200 experiment, the nEXO precursor.

2.4 Double Beta Decay search with the nEXO Detector

The nEXO detector is based on a Time Projection Chamber (TPC) filled with 5 tonnes of liquid xenon (5109 kg) enriched 90% at ^{136}Xe [51]. As shown in Fig. 2.7, it will be the only $0\nu\beta\beta$ next generation Xe-based detector able to probe the effective Majorana mass down to 15 meV. Additionally, the 5109 kg of LXe are chosen to achieve a competitive sensitivity. This last aspect can be easily understood using a simple estimation based on Eq. 2.20. Requiring a minimum $0\nu\beta\beta$ event rate of 1 event/year and assuming a half life limit of $T_{1/2}^{0\nu\beta\beta} \geq 9.7 \times 10^{27}$ years, the total

mass of xenon that is necessary to have to achieve the required event rate is about 5000 kg. This simple estimation, based on the law of radioactive decay shows that only large mass detectors can achieve a sufficient number of events in the ROI to perform a successful $0\nu\beta\beta$ search.

According to the nEXO baseline design, the nEXO TPC will be a monolithic single-phase detector with a completely free volume filled with LXe. This is a significantly different approach if compared with the design of its precursor: the EXO-200 detector, which instead had an optical transparent cathode in the centre of the TPC used to create the electric field [12], as shown in Fig. 2.10.

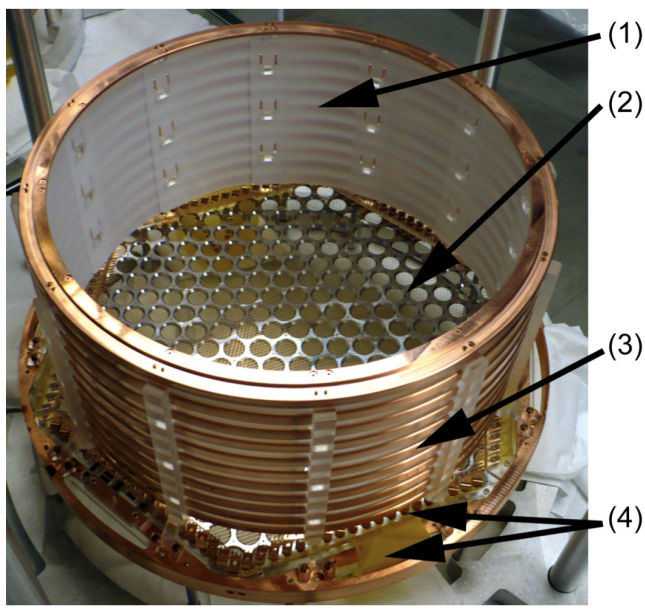

Figure 2.10: EXO-200 detector. PTFE (Polytetrafluoroethylene) tiles (1) installed inside the field-shaping rings serve as reflectors for the scintillation light. The aluminum-coated side of the large-area avalanche photodiodes platter (2) is visible, as well as the field cage (3), ionization wires and flexible cables (4) [12].

As shown in Sec. 2.2.2 the current most stringent limit on the ($0\nu\beta\beta$) decay in ^{136}Xe is 10.7×10^{25} yr from the KamLAND-Zen experiment, with a corresponding sensitivity exposure of 504 kg $\times$ yr [14]. The diagnostic power of a

LXe TPC allowed the EXO-200 experiment to reach a competitive sensitivity of 3.7×10^{25} yr with a substantially smaller exposure (178 kg $\times$ yr) and xenon mass (200 Kg) if compared with the KamLAND-Zen experiment [15]. A careful selection of the TPC material, with also the intrinsic capability to simultaneously detect signal and background, will be the primary strength of the nEXO detector following the same path of its precursor. The nEXO design is in fact conservative and very few assumptions of material radio-purity were made beyond what was already experimentally demonstrated and measured with the EXO-200 detector [52].

Fig. 2.11 shows a sketch of the nEXO LXe TPC located inside a vacuum insulated cryostat. A thicker shield will be also obtained with a large water tank,

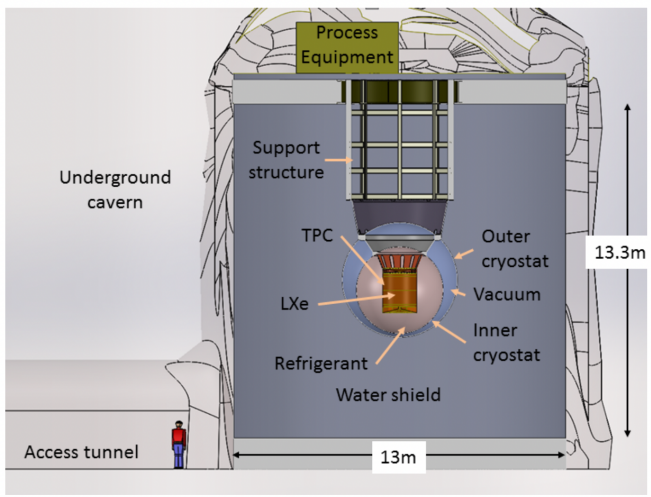

Figure 2.11: Sketch of the nEXO TPC located in the Cryopit at SNOLAB, the Canadian underground science laboratory [2].

which acts as an active cosmic-ray veto detector. The location of the nEXO detector is not yet finalized and, according to the nEXO baseline design, it will be located in the Cryopit at SNOLAB, the Canadian underground science laboratory. As a monolithic detector, surface αs and βs can be rejected by a fiducial volume cut after position reconstruction, as introduced in Sec. 2.3.

Decays producing αs inside the LXe bulk can also be easily rejected by a light-to-charge ratio cut, since α events create much denser charge clouds than electrons, and therefore a larger amount of scintillation light is produced from re-

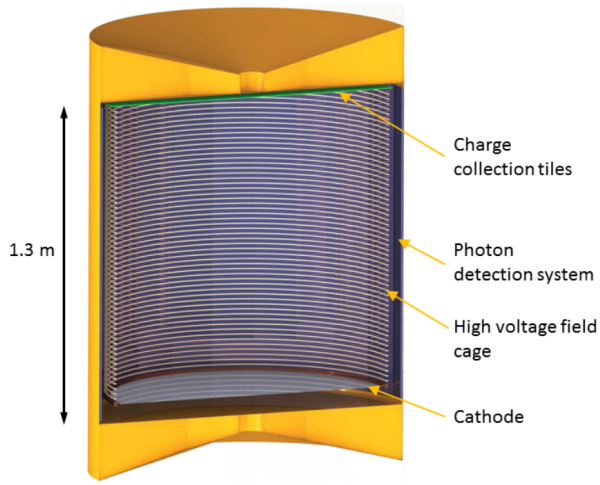

Figure 2.12: Sketch of the nEXO TPC [2].

combination. Moreover, the self-shielding capabilities of a large detector whose linear dimensions exceed 1 m are ideal to identify and suppress γ ray background in the energy region of interest (Sec. 2.3).

The energy resolution around the Q-value of the $0\nu\beta\beta$ decay is the crucial parameter in the $0\nu\beta\beta$ search, since it is the only instrument to effectively separate $2\nu\beta\beta$ decays from $0\nu\beta\beta$ decays (Sec. 2.2.4). nEXO is designed to optimize this characteristic, providing the best possible energy resolution for a LXe TPC with a final design goal of 1% energy resolution (σ/Q) for the $0\nu\beta\beta$ decay of ^{136}Xe (Q-value at 2458.07 ± 0.31 keV [9]).

In order to achieve this objective, the nEXO TPC is designed to read out with high efficiency both the charge clouds and the light produced by the LXe ionization and scintillation, respectively. This will allow it to take advantage of the anticorrelation between the two channels and improve therefore the final energy resolution, as discussed in Sec. 2.3. Fig. 2.12 shows a sketch of the nEXO TPC with the location of the channels used for the charge and photon detection. The electric field in the TPC is created thanks to 58 Field Shaping Rings (FSRs) held together by 24 1.2 meters long sapphire single-crystal rods and spaced by 1.6 cm long cylindrical spacers [2]. The sapphire rods are held in tension by springs above

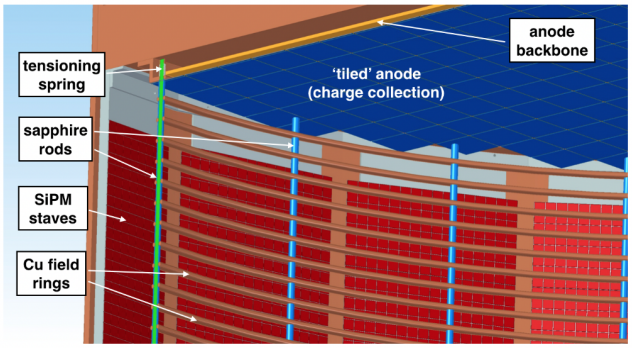

Figure 2.13: A close-up view of the TPC anode region showing the charge-collecting anode, the tensioned rods, and the SiPM staves behind the field cage [6].

the anode region. The field is graded from anode to cathode by a set of custom-made, low-mass, low-radioactivity resistors, connected to the FSRs.

Charge collection is achieved at the top of the TPC with silica tiles patterned with crossed metallic strips [6], as shown in Fig. 2.13. Scintillation light is instead collected with a large-area array (~ 5 m^2) of VUV-sensitive Silicon Photo-Multipliers (SiPMs). This is a significant difference if compared with the EXO-200 light detection system that was constituted by large-area avalanche photodiodes [53]. Vacuum Photo-multipliers are in fact too radioactive to be used in nEXO. The array of VUV sensitive SiPMs is expected to be located behind the field-shaping rings [54]. In this way it will be possible to achieve a higher light collection efficiency, compared with the EXO-200 detector, in which the large-area avalanche photodiodes were located behind the anode crossed-wire planes.

2.4.1 The nEXO Charge Collection and Readout Subsystem

In nEXO we plan to use a segmented anode composed of an array of tiles for the readout of the charge produced by the ionization of LXe [6, 55]. Each tile consists of a dielectric substrate covered with an array of 60 orthogonal metal charge-collecting strips for the charge collection. Each strip consists of 30 square pads that are 3 mm across the diagonal and daisy-chained at their corners. Indi-

vidual strips can be read out as an independent channel. A schematic drawing of a 10 cm by 10 cm prototype tile with a strip pitch of 3 mm is shown in Fig. 2.14. This

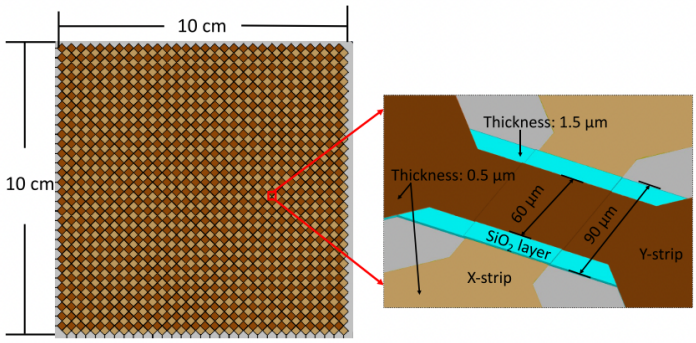

Figure 2.14: Schematic drawing of a prototype charge collection tile with 10 cm edge and 3 mm pitch electrodes [6].

prototype tile was already tested in a LXe TPC test chamber, where good agreement was achieved between the measured ionization spectrum of a ^{207}Bi source recorded with the tile and the one predicted by simulations [6, 55].

The characteristics of the nEXO charge readout subsystem are driven by the objective to achieve a 1% energy resolution at the decay Q-value. The main contribution of the charge subsystem to the overall nEXO energy resolution is, however, not coming from the electron collection and extraction efficiency in LXe (which generally approaches 100%), but instead it mainly depends on the readout electronic noise of the charge channels. Fig. 2.15 shows, for example, the energy resolution at 400 V/cm for different readout configurations, as a function of the overall photon collection efficiency of the nEXO light detection subsystem. As it can be seen the overall energy resolution can be significantly degraded by the electronic noise in the charge channel (here represented as a function of the readout board location and therefore temperature), while keeping unaltered the charge collection and extraction efficiency in LXe.

2.4.2 The nEXO Light Collection and Readout Subsystem

The readout of scintillation light is crucial to provide a prompt signal at the interaction time that can be used not only to obtain the best possible energy resolu-

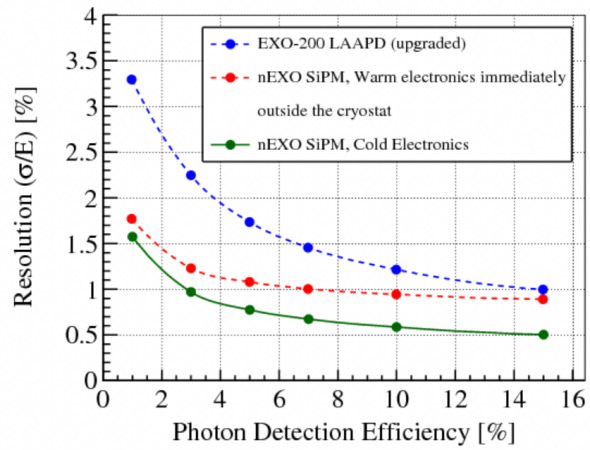

Figure 2.15: Energy resolution as a function of the overall light detection efficiency of the nEXO TPC for a field of 400 V/cm and front-end electronic appropriate for internal (cryogenic) and external (room temperature and immediately outside of the cryostat) usage. The curve for the upgraded (Phase-II) EXO-200 detector is also shown for reference [2].

tion, but also as trigger for the charge readout channel [51]. This thesis will focus on studying the performances of the candidates photo-detectors that will be used in the photon-sensor portion of the nEXO experiment. In order to achieve a 1% energy resolution at the Q-value of the $0\nu\beta\beta$ decay of ^{136}Xe, these photo-detectors, and their readout electronics, need to fulfill strict requirements to not degrade the overall energy resolution. This last quantity tends in fact to be dominated by fluctuations in the scintillation light channel because its detection efficiency is significantly smaller compared with the one achievable with the charge channel, which generally approaches 100% (Sec. 2.4.1).

According to the discussion of Sec. 2.3, when a particle deposits energy in LXe, it produces singlet and triplet molecules that decay quickly ($\sim$30 ns) emitting 175 nm VUV photons (174.8 ± 10.2 nm [47]). Simulations show that, when including the photon transport time, 99.9% of scintillation photons arrive at the photo-detectors within 100-150 ns of the interaction time [2].

In nEXO we plan to have a maximum photon-charge integration time after the trigger of 1 µs. This will allow not only to collect all the light produced by the

original interaction, but also to fully reconstruct the photo-detector signal, as will be shown in the next section.

2.4.2.1 VUV sensitive SiPMs for light detection in LXe

nEXO plans to use VUV sensitive Silicon Photo-Multipliers (SiPMs) as photon-sensors for the detection of the 175 nm scintillation light of LXe [56]. In contrast to the widely used Photomultiplier Tubes (PMTs), SiPMs are low-voltage powered, optimal for operation at cryogenic temperatures, and have low radioactivity levels with high gain stability ($\sim 10^6$) over the time in operational conditions [16, 57]. For these reasons not only nEXO, but other large-scale low-background cryogenic experiments such as Darkside-20k, are migrating to a SiPM-based light detection system [17, 18]. SiPMs consist of an array of tightly packed Single Photon Avalanche Diode (SPAD) acting as an avalanche photodiode that can behave in the Geiger mode regime when the device is reverse biased above a threshold voltage (breakdown voltage). In the conventional SiPM design each SPAD is connected to a series resistor (called the quenching resistor) that limits the current flowing during the breakdown and thus ensures that the avalanche current is eventually quenched [58]. The total charge realised from the SPAD defines the device gain and it depends on the SPAD capacitance C_{SPAD} and applied bias voltage such that $Q = C_{\mathrm{SPAD}}\mathrm{OV}$. The quantity OV is defined as the over voltage and it is equal to $(V - V_{\mathrm{BD}})$ where V is the applied bias voltage and V_{BD} is the breakdown voltage, defined as the minimum bias voltage for which an avalanche can be self sustained, i.e. when a pulse is actually produced [59]. When the avalanche current flows in the quenching resistor it induces a voltage drop on the SPAD itself that brings the voltage across the diode back to the breakdown voltage. After the avalanche is quenched the SPAD starts its recharging phase where it slowly returns to the original bias voltage. For a detail electrical characterization of SiPMs we refer the reader to Ref. [60]. An example of a SiPM pulse, that corresponds to the discharge of one SiPM SPAD is reported in Fig. 2.16. The most important SiPMs characteristic is their capability to detect light i.e. their Photon Detection Efficiency (PDE), which represents the combined probability that a photon is absorbed in the active volume of the device with a subsequently triggered avalanche, i.e. the pro-

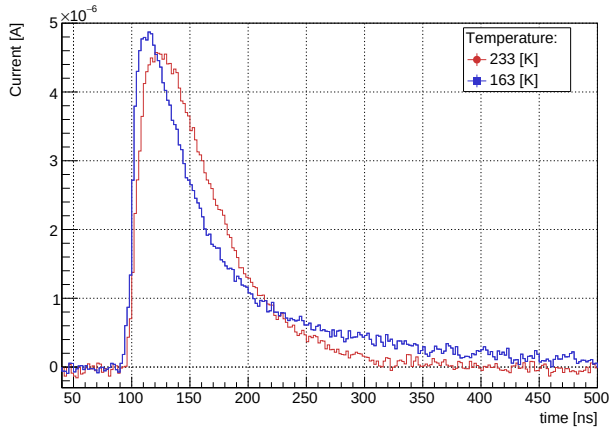

Figure 2.16: Pulse shape produced by the discharge of one SiPM SPAD for two different temperatures (233 K and 173 K) for one SiPM tested for nEXO (Hamamatsu VUV4 MPPC). The complete characterization of this device is reported in Chapter 3. The SiPM pulse shape depends on the SiPM temperature, since the quenching resistor used to quench the avalanche can have a strong temperature dependence [61].

duction of a pulse, as shown in Fig. 2.16. Only recently different companies and research institutions developed SiPMs with sensitivity extending to the 175 nm region. Fondazione Bruno Kessler (FBK), for example, produced several batches of VUV SiPMs for the nEXO experiment. Hamamatsu Photonics Inc. also developed four generations of SiPMs for applications in LXe.

In order to guide the discussion about the photo-detector specifications for nEXO, it is necessary to first introduce the SiPM characteristics that define the contribution of the light detection subsystem to the total nEXO energy resolution.

Fig. 2.17 shows the nEXO energy resolution as a function of the overall photon collection efficiency. A requirement of 1% in the energy resolution automatically sets a requirement on the overall light detection efficiency of the TPC that needs to be bigger than or equal to 3%. It is useful to define the overall light detection efficiency of the TPC (called ε_p) as the product of two quantities, the nEXO detector photon Collection Efficiency (CE), and the SiPM Photon Detection

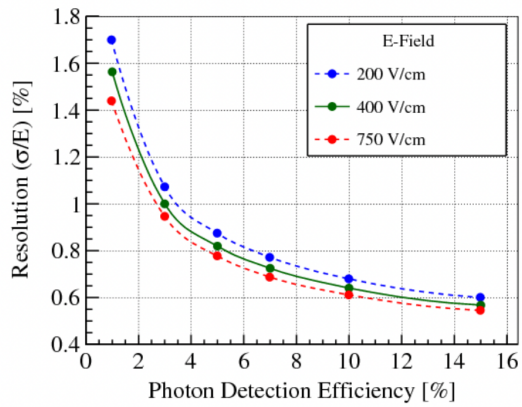

Figure 2.17: Energy resolution as a function of the overall light detection efficiency of the nEXO TPC for several electric fields [2].

Efficiency (PDE).

$$\varepsilon_p \equiv \mathrm{CE} \times \mathrm{PDE} \tag{2.23}$$

The CE is defined as the probability a photon produced randomly in the nEXO detector arrives to the SiPM surface; while the PDE represents instead the probability that a photon that is hitting the SiPM surface is subsequently absorbed by the SiPM and triggers an avalanche.

Fig. 2.18 shows a simulation of the photon CE (called photon transport efficiency in the figure) as a function of the overall reflectivity of Field Shaping Rings (FSR)s and cathode. If we consider a 15% SiPM PDE at the scintillation wavelengths of LXe, it is necessary to achieve, accordingly to Eq. 2.23, a photon CE of 20%. From Fig. 2.18 this means a $\sim$ 50% reflectivity of the cathode, anode and field shaping rings. The value of 15% for the SiPM PDE is considered as the baseline for the nEXO design. It is a conservative value, but, as it will be shown in Chapters 3 and 4, it represents the average PDE achievable by the current generation of VUV SiPMs.

In addition to their light detection capabilities, SiPMs suffer from several sources of intrinsic noise. Dark and correlated avalanche noise are in fact crucial SiPM parameters that can eventually reduce the overall nEXO energy resolution

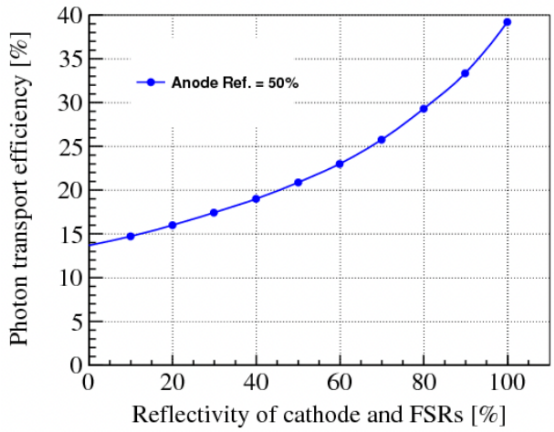

Figure 2.18: Simulation of the photon Collection Efficiency (CE) of the nEXO TPC as a function of the Field Shaping Rings (FSR)s and cathode reflectivity. In the simulation the anode reflectivity was set to 50% [2].

since they can artificially increase the fluctuations in the number of photons detected by the SiPMs.

Dark Noise (DN) pulses are charge signals generated by the formation of electron-hole pairs due to thermionic or field enhanced processes [62]. The most stringent constraint on the SiPM dark noise rate for the nEXO energy resolution comes from the requirement to trigger on scintillation pulses with energy as low as 500 keV, useful for background rejection strategies, for which a dark noise rate $\leq$ 50 Hz/mm^2 is required.

Correlated Avalanche (CA) noise is due instead to at least two processes: the production of secondary photons during the avalanche in the gain amplification stage detected in nearby cells; and the trapping and subsequent release of charge carriers produced in avalanches. The latter process is usually referred to as afterpulsing, while the former is usually called crosstalk. Afterpulse events can trigger the same cell in which the original avalanche happened multiple times. If we define as one Photo-electron Equivalent (PE) the charge realized by the discharge of one SiPM SPAD, the charge realized by one afterpulse event is, on average, smaller if compared with the original one PE discharge, since afterpulse events trigger the

cell during its recharging time. The mechanism of detrapping, that is at the basis of the afterpulse [63], is, however, a function of the temperature and it is not unlikely at 163 K to have afterpulses that trigger the original cell several ms after the original discharge. In this case, the charge realised from an afterpulse event is equal to 1 PE, since the original SPAD had enough time to be completely recharged.

CrossTalk (CT)s photons produce instead nearly simultaneous avalanches to the primary one (Direct CrossTalk (DiCT)) or delayed by several ns (Delayed CrossTalk (DeCT)), as shown in Fig. 2.19. Since Crosstalk photons trigger SPADs that are completely charged, the additional charge realized by a DiCT or DeCT event is a multiple of one PE, depending on the number of cells discharged [64]. In general, the subset of the CAs constituted by afterpulses and delayed crosstalk

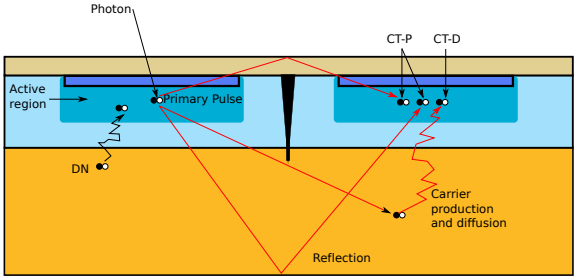

Figure 2.19: Representation of the noise sources in SiPMs: Dark Noise (DN) and Correlated Avalanche (CA) noise. DN are charge signals generated by the formation of electron-hole pairs due to thermionic or field enhanced processes. CA noise is instead mainly due to the production of secondary photons (called Cross Talk (CT) photons) during an avalanche in the gain amplification stage of one cell detected in nearby cells. Generally CT events are categorized accordingly to the time difference with respect to the primary discharged cell that originated them. If prompt ($\sim$ ps) they are called: Prompt CT (CT-P in the figure); if delayed ($\sim$ ns) they are called Delayed CT (CT-D in the figure).

events is named Correlated Delayed Avalanche (CDA)s. Unlike DN events, CAs (and therefore CDAs) are correlated with a primary signal and therefore they are present only if an avalanche happens i.e. a SiPM SPAD is discharged with the subsequent production of a pulse.

Independently of the mechanism responsible for their generation, all CAs pro-

Parameter	Requirement
Photon Detection Efficiency at 175 nm	$> 15\%$
Dark Noise Rate	< 50 Hz/mm^2
Relative Fluctuation of the mean number of CA in 1 μs	< 0.4
Equivalent noise charge	< 0.1 PE r.m.s

Table 2.1: Requirements for the nEXO light detection subsystem. See text for explanation.

duce an extra charge (measurable in PE) in the nEXO 1 μs acquisition window, therefore artificially increasing the total number of photons detected. Simulations show as the contribution of correlated avalanches to the resolution is subdominant when the relative fluctuation of the mean number of correlated avalanches per pulse is smaller than 0.4 [2]. This requirement sets a corresponding upper bound on the over voltage since the correlated avalanche rate increases with voltage, as will be shown in Chapters 3 and 4. Table 2.1 summarizes the SiPMs requirements for the just introduced nEXO light detection subsystem.

In addition to the SiPMs requirements, we include in Table 2.1 one more requirement to account for the electronic readout noise in the photon channel (Equivalent noise charge). In this case we require an electronic noise to be smaller than 0.1 PE r.m.s. to be able to detect and then trigger on single photoelectrons whose charge, by definition, is equal to 1 PE [65]. Figure 2.20 shows the predicted energy resolution including the contribution of the charge and light channel, as a function of the SiPM over voltage, for one of the SiPMs produced by FBK for the nEXO experiment and tested in Ref. [1]: the FBK VUV HD 1, with its Low Field (LF) and Standard (STD) version. The most dominant feature of the three curves in Fig. 2.20 is the existence of a minimum. Furthermore, the minimum does not coincide with the largest operational over voltage, which in general results in a worse energy resolution due to the increase of the SiPM correlated noise. Overall the FBK VUV HD 1 SiPM in its LF version satisfies, at an over voltage roughly between 2 and 3 V, the requirement on the nEXO energy resolution to be smaller or equal to 1% for the $0\nu\beta\beta$ decay of ^{136}Xe (Q-value at 2458.07 ± 0.31 keV [9])

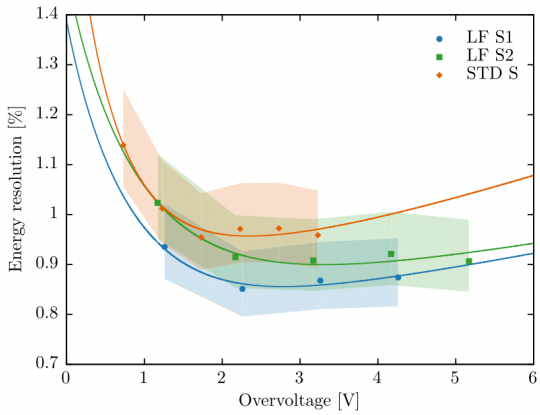

Figure 2.20: Estimated energy resolution for nEXO as a function of the over voltage for the FBK VUV HD 1 SiPM in its Low Field (LF) and Standard (STD) version [1].

2.4.3 A model for the nEXO Energy Resolution

In this section we introduce a model for the prediction of the expected energy resolution in nEXO. This model differs from the one used in Ref. [1] to construct Fig 2.20. The main difference is the estimation of the correlated avalanche noise contribution. In [1] CAs are in fact treated as Poisson processes. This approximation is justified at small over voltages, like the ones shown in Fig. 2.20, but tends to underestimate the contribution of the CAs to the overall energy resolution at high over voltages, as will be shown in Sec. 4.5 of Chapter 4.

The model derived in this section is based on the assumption that each recombining electron-ion pairs produces an exciton (excited xenon atom) which in turn produces a photon. The appropriateness of this approximation will be discussed in more details in Sec. 2.4.3.3. More generally, when particles deposit an energy E in LXe, they produce a number of electron-ion pairs and excitons. Some of the electrons produced in the initial energy deposition, however, can either recombine (depending on the density of the tracks realised by the initial particle), or they can be lost due to the inefficiency of the extraction electric field (Sec. 2.3). Regardless of the specific situation, when an electron-ion pair recombines, it produces an exciton, which in turn produces a photon. If we denote with r the fraction of recombin-

ing electrons, the maximum number of detectable electrons (n_q) and photons (n_p) for an initial population of n_i electron-ion pairs and n_{ex} excitons (produced by the initial energy deposition), can be written as

$$n_q = (1-r)n_i \tag{2.24}$$

and

$$n_p = (n_{\text{ex}} + rn_i) \tag{2.25}$$

respectively.
Under these assumptions, it is possible to define a recombination-independent value

$$W \equiv \frac{E}{n_q + n_p} \tag{2.26}$$

which corresponds to the energy required to create a single quantum of either type (light or charge). Equation 2.26 is independent from the recombination (and there-

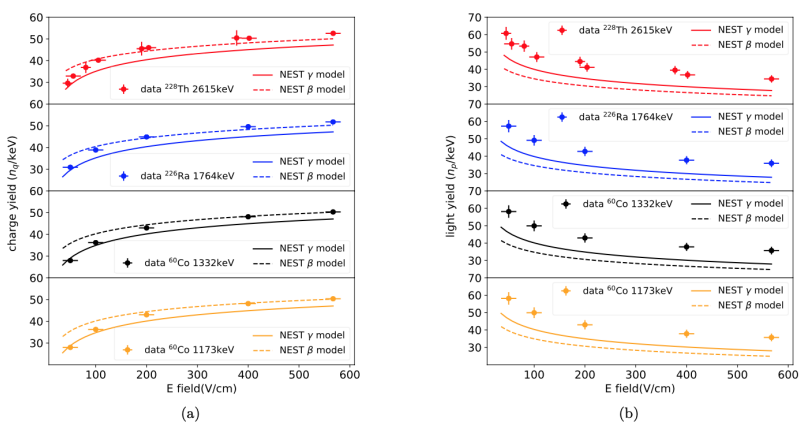

Figure 2.21: Comparison of the charge yields (a) and light yields (b) measured by the EXO-200 detector with the NEST simulator for γ and β particles [7, 8].

fore from the extraction electric field), since the quantity $n_q + n_p$ is independent of r, in fact

$$(n_q + n_p) = \{(1-r)n_i + n_{\text{ex}} + rn_i\} = \{n_{\text{ex}} + n_i\} \tag{2.27}$$

In addition to these definitions, it is also possible to define the energy required to produce a single electron-ion pair prior to recombination as

$$W_i \equiv \frac{E}{n_i} \tag{2.28}$$

Due to the anti-correlation between the light and charge channel in nEXO (in agreement with what was done in EXO-200) E can be decomposed using a rotated energy scale defined as [8]

$$E \propto \{\cos(\theta)\langle E_q\rangle + \sin(\theta)\langle E_p\rangle\} \tag{2.29}$$

where $\langle E_q\rangle$ and $\langle E_p\rangle$ are the mean energy deposited in the charge and light channel, respectively. Here θ represents the rotation angle and it indicates the optimal weighting of the charge and light signals in order to minimize the overall energy resolution.
The mean number of quanta (of both types) produced by a single energy deposition of energy E can then be written as

$$\langle n\rangle = \frac{\langle E\rangle}{W} \propto \langle n_q\rangle + \langle n_p\rangle \tag{2.30}$$

where $n_p = \frac{\langle E_p\rangle}{W}$ and $n_q = \frac{\langle E_q\rangle}{W}$. In what follows we will assume that $\langle E\rangle$ is equal to the Q-value of the $0\nu\beta\beta$ decay in ^{136}Xe (2458.07 ± 0.31 keV [9]) and W equal to 11.5 ± 0.5 (syst). ± 0.1 (stat.) eV [8]. From this it follows that

$$\langle n\rangle = \frac{\langle E\rangle}{W} = 2.14 \times 10^5 \tag{2.31}$$

The values of n_p and n_q can be derived knowing the decay Q-value and the light and charge yields (Fig. 2.21). Using for these two quantities the values measured in EXO-200 ($0.037\frac{\gamma}{\mathrm{eV}}$ and $0.050\frac{e}{eV}$[8]), n_p and n_q follow as

$$n_p = 90946 \tag{2.32}$$

$$n_q = 122900 \tag{2.33}$$

In term of quanta, the relative standard deviation of Eq. 2.30 (also called the energy resolution for the $0\nu\beta\beta$ decay or optimum estimator) can then be computed as

$$\frac{\sigma_n}{\langle n \rangle} = \frac{\sqrt{\sigma_q^2 + \sigma_p^2 + 2\mathrm{Cov}_{q,p} + \sigma_{\mathrm{Xe}}^2}}{\langle n \rangle} \tag{2.34}$$

where σ_q^2 and σ_p^2 are the variances of n_q and n_p, respectively. The first three terms in Eq. 2.34 follow directly using the theory of error propagation for correlated quantities. The last term, instead, represents an additional variance that was added to Eq. 2.34 to include the intrinsic fluctuations in the number of quanta not due to recombination (i.e. some loss due to heat). It can be written as

$$\sigma_{\mathrm{Xe}}^2 = f_{\mathrm{Xe}} \langle n \rangle \tag{2.35}$$

where f_{Xe} is defined as the LXe Fano Factor measured to be 0.059 [13] which represents a deviation from the Poisson statistic assumed by Eq. 2.35. More details of the LXe Fano Factors can be found in Ref. [66]. Compared to other mechanisms (readout charge noise and photon noise) this additional fluctuation can be neglected.

2.4.3.1 Light subsystem

In nEXO we plan to use VUV sensitive SiPMs in a photon counting mode. The number of avalanches measured by the SiPMs can be written as

$$n_{av} = (n_p \varepsilon_p + n_{\mathrm{DC}})(1 + \langle \Lambda \rangle) \tag{2.36}$$

where $\langle \Lambda \rangle$ represents the mean number of extra avalanches and n_{DC} represents the number of Dark Counts (DC) in the acquisition window. n_p, as introduced in the previous section, is the number of photons produced by the initial energy deposition and it is equal to the maximum number of photon detectable. Note as formally in Eq. 2.36 photon induced avalanches and dark induced avalanches are treated in the same way, i.e. as random continuous variables. Additionally, ε_p represents the total light detection efficiency defined in Eq. 2.23. This quantity will be assumed constant in what follows.

The number of photons detected can then be defined as

$$n_d \equiv n_p \varepsilon_p \tag{2.37}$$

Using this last equation, Eq. 2.36 can be written as

$$n_{av} = (n_d + n_{DC})(1 + \langle \Lambda \rangle) \tag{2.38}$$

and inverted to derive n_p as

$$n_p = \frac{n_{av} - n_{DC}(1 + \langle \Lambda \rangle)}{\varepsilon_p (1 + \langle \Lambda \rangle)} = \left[\frac{n_{av}}{\varepsilon_p (1 + \langle \Lambda \rangle)} - \frac{n_{DC}}{\varepsilon_p} \right] \tag{2.39}$$

Its variance follows as

$$\sigma_p^2 = \frac{\sigma_{av}^2}{(\varepsilon_p (1 + \langle \Lambda \rangle))^2} + \frac{\sigma_{DC}^2}{\varepsilon_p^2} + \sigma_r^2 \tag{2.40}$$

where: σ_{av}^2 is the variance of n_{av}; σ_{DC}^2 is the variance of n_{DC} and σ_r^2 is an additional term that accounts for the fluctuation in units of quanta, resulting from recombination. As will be shown in Chapters 3 and 4, the number of dark count events in the acquisition window, as well as its fluctuation, is completely negligible at cryogenic temperatures, therefore Eq. 2.40 can be simplified as

$$\sigma_p^2 \sim \frac{\sigma_{av}^2}{(\varepsilon_p (1 + \langle \Lambda \rangle))^2} + \sigma_r^2 \tag{2.41}$$

Error propagation of Eq. 2.38 gives

$$\sigma_{av}^2 = \left(\frac{\partial n_{av}}{\partial n_d} \right)^2 \sigma_d^2 + \left(\frac{\partial n_{av}}{\partial \langle \Lambda \rangle} \right)^2 \sigma_{\langle \Lambda \rangle}^2 + \left(\frac{\partial n_{av}}{\partial n_{DC}} \right)^2 \sigma_{DC}^2 \tag{2.42}$$

with

$$\sigma_{\langle \Lambda \rangle}^2 = \frac{\sigma_\Lambda^2}{\langle n_{DC} \rangle + \langle n_d \rangle} \tag{2.43}$$

with σ_Λ^2 and $\langle \Lambda \rangle$ the variance and mean of the number of additional avalanches in the acquisition window and $\langle n_{DC} \rangle + \langle n_d \rangle$ the total number of avalanches detected.

σ_Λ^2 and $\langle\Lambda\rangle$ can be measured from the SiPM dark noise data by constructing a histogram of the charge of all the pulses within the nEXO acquisition window (that extends up to 1 μs from the trigger pulse), and scaling it such that the single Photo-electron Equivalent (PE) avalanche charge is equal to one.
Assuming: (i) a binomial distribution for the number of photons detected with probability to be detected equal to ε_p ($\sigma_d^2 = \varepsilon_p(1-\varepsilon_p)n_p$, $\langle n_d\rangle = n_p\varepsilon_p$) and (ii) a Poisson distribution for the number of Dark Counts events in the acquisition window ($\sigma_{DC}^2 = \langle n_{DC}\rangle$, $\langle n_{DC}\rangle = n_{DC}$), we get

$$\sigma_{av}^2 = (1+\langle\Lambda\rangle)^2\varepsilon_p(1-\varepsilon_p)n_p + (\langle n_{DC}\rangle + \langle n_d\rangle)^2\sigma_{\langle\Lambda\rangle}^2 + (1+\langle\Lambda\rangle)^2\langle n_{DC}\rangle + \eta_{noise}^2 \tag{2.44}$$

The last term in Eq. 2.44, η_{noise}^2, accounts for an additional noise contribution due to avalanches misreconstructed by the photon-readout noise channel. This quantity cannot be calibrated until the photon-readout for nEXO is finalised, and therefore it will be neglected in what follows.
Eq. 2.41 then becomes

$$\sigma_p^2 = \frac{(1+\langle\Lambda\rangle)^2\varepsilon_p(1-\varepsilon_p)n_p + (\langle n_{DC}\rangle + \langle n_d\rangle)^2\sigma_{\langle\Lambda\rangle}^2 + (1+\langle\Lambda\rangle)^2\langle n_{DC}\rangle}{(\varepsilon_p(1+\langle\Lambda\rangle))^2} + \sigma_r^2 \tag{2.45}$$

Simplification gives

$$\sigma_p^2 = \frac{(1-\varepsilon_p)n_p}{\varepsilon_p} + \frac{(\langle n_{DC}\rangle + \langle n_d\rangle)^2\sigma_{\langle\Lambda\rangle}^2}{(\varepsilon_p(1+\langle\Lambda\rangle))^2} + \frac{\langle n_{DC}\rangle}{\varepsilon_p^2} + \sigma_r^2 \tag{2.46}$$

Using Eq. 2.43, Eq. 2.46 then becomes

$$\sigma_p^2 = \frac{(1-\varepsilon_p)n_p}{\varepsilon_p} + \frac{(\langle n_{DC}\rangle + \langle n_d\rangle)\sigma_\Lambda^2}{(\varepsilon_p(1+\langle\Lambda\rangle))^2} + \frac{\langle n_{DC}\rangle}{\varepsilon_p^2} + \sigma_r^2 \tag{2.47}$$

The mean number of dark noise events in the acquisition window $\langle n_{DC}\rangle$ can be estimated from the dark noise data by measuring the dark noise rate at 163 K and integrating it for a time length equal to the nEXO acquisition window (1 μs). It is, however, a sub-dominant contribution, due to the extremely low dark noise rate of SiPMs at 163 K. Therefore, using the same approximation done with Eq. 2.41,

Eq. 2.47 becomes

$$\sigma_p^2 \sim \frac{(1-\varepsilon_p)n_p}{\varepsilon_p} + \frac{\langle n_d \rangle \sigma_\Lambda^2}{(\varepsilon_p(1+\langle \Lambda \rangle))^2} + \sigma_r^2 \tag{2.48}$$

The quantity $\langle n_d \rangle = n_p \varepsilon_p$ is complicated to measure, since it depends on the total detector light collection efficiency (ε_p) which can only be estimated with a combination of light propagation simulations in the TPC (for the light Collection Efficiency (CE)) and SiPM Photon Detection Efficiency (PDE) measurements at 175 nm.

2.4.3.2 Charge subsystem

The contribution of the charge subsystem to the overall nEXO energy resolution can be derived with the same approach introduced in the previous section. In particular, the number of charges detected n_{dq} can be written as

$$n_{dq} = \varepsilon_q n_q \tag{2.49}$$

where ε_q is the charge collection efficiency. From this follows that

$$n_q = \frac{n_{dq}}{\varepsilon_q} \tag{2.50}$$

Assuming binomial statistics for the number of detected charges with probability to be detected equal to ε_q, we get

$$\sigma_q^2 = \frac{(1-\varepsilon_q)n_q}{\varepsilon_q} + \frac{\sigma_{q,noise}^2}{\varepsilon_q^2} + \sigma_r^2 \tag{2.51}$$

where $\sigma_{q,noise}^2$ accounts for the noise contribution in the charge channel and σ_r^2 is the variation in units of quanta in the charge channel due to recombination fluctuations. The charge collection efficiency is assumed to be function of the drift time t such that $\varepsilon_q = e^{-\frac{t}{\tau}}$ with $t = l/v$ ($l = 0.65$ m and $v = 2$ mm/μs [2]). The electron lifetime τ depends on the xenon purity and it is set in this model to be 10 ms, accordingly to the nEXO baseline design [2]. Overall these parameters bring to

a charge collection efficiency of $\varepsilon_q = 0.97$ %. Finally, the noise contribution in the charge channel, which depends on the design of the pixel pitch, is predicted to be ~ 1100 e$^-$[2].

2.4.3.3 Expected nEXO energy resolution

In Sec. 2.4.3 we assumed perfect anticorrelation between the light and charge channels, such that every recombined electron generates a VUV photon. With this assumption we derived Eq. 2.51 and Eq 2.48 introducing in both equations a term σ_r^2 that represents the recombination fluctuation for the two channels. With the same assumption it follows that the covariance between the two channels in Eq. 2.34 is simply $\mathrm{Cov}_{q,p} = -\sigma_r^2$.
This assumption was tested by the EXO-200 collaboration in Ref. [8] and it was found to be true with a recombination efficiency equal to 97%. In other words, a recombined electron generates a VUV photon in 97% of the cases. Due to the excellent agreement of the EXO-200 data with this assumption, in the nEXO estimation of the energy resolution we will assume that this condition holds true at all times. If we substitute the contribution of the light channel (Eq. 2.48) and charge channel (Eq. 2.51) in Eq. 2.34, we can derive an estimation of the energy resolution as follows

$$\frac{\sigma_n}{\langle n \rangle} = \frac{\sqrt{\left(\frac{(1-\varepsilon_p)n_p}{\varepsilon_p} + \frac{\langle n_d \rangle \sigma_\Lambda^2}{(\varepsilon_p(1+\langle \Lambda \rangle))^2} + \sigma_r^2\right) + \left(\frac{(1-\varepsilon_q)n_q}{\varepsilon_q} + \frac{\sigma_{q,noise}^2}{\varepsilon_q^2} + \sigma_r^2\right) - 2\sigma_r^2}}{\langle n \rangle} \tag{2.52}$$

Simplification gives

$$\frac{\sigma_n}{\langle n \rangle} = \frac{\sqrt{\left(\frac{(1-\varepsilon_p)n_p}{\varepsilon_p} + \frac{\langle n_d \rangle \sigma_\Lambda^2}{(\varepsilon_p(1+\langle \Lambda \rangle))^2}\right) + \left(\frac{(1-\varepsilon_q)n_q}{\varepsilon_q} + \frac{\sigma_{q,noise}^2}{\varepsilon_q^2}\right)}}{\langle n \rangle} \tag{2.53}$$

This last equation will be used in Chapter 4 for the estimation of the expected nEXO energy resolution using all the measurements done in Chapters 3 and 4 of this work for two SiPMs candidates for nEXO: the Hamamatsu VUV4 MPPC and the FBK VUV HD 3 SiPM.

2.5 Conclusions

In this chapter we introduced the main motivation behind the need for a $0\nu\beta\beta$ search. We also introduced liquid xenon (LXe) as an attractive candidate for this type of physics, since it not only serves as the source of the decay, but also as its detector. Moreover its anticorrelation and self shielding properties allow us to implement extremely precise particle identification and background suppression techniques that are crucial for a low background cryogenic experiment. In the second part of the chapter we introduced the nEXO experiment that will be one of the most promising candidates to perform a successful $0\nu\beta\beta$ search, allowing us to probe the effective Majorana mass down to 15 meV. We also introduced the requirement of the nEXO charge and light subsystem. The next two chapters of this thesis will focus on the nEXO light detection subsystem. In particular they will show the characterization of several SiPM photocandidates for the nEXO experiment, comparing their performance against the nEXO requirements, summarised in Table 2.1. Custom setups were built at TRIUMF specifically to test these devices. A significant part of the next two chapters will therefore be devoted to explain their construction. Finally, at the end of Chapter 4, we will use all the measurements of Chapters 3 and 4 to estimate the contribution of the tested SiPMs to the overall nEXO energy resolution, using the model introduced in Sec. 2.4.3 of this chapter.

Chapter 3

Characterization of the Hamamatsu VUV4 MPPCs for nEXO

3.1 Introduction

Silicon Photo-Multipliers (SiPMs)[1] have emerged as a compelling photo-sensor solution over the course of the last decade [57]. nEXO aims to probe the boundaries of the standard model of particle physics by searching for neutrino-less double beta decay ($0\nu\beta\beta$) of ^{136}Xe [10].

The requirements of the photo-sensor portion of the nEXO experiment are summarised in Table 2.1. More precisely, the VUV SiPMs that will be used in nEXO and their readout electronic must meet the following requirements [2]: (i) Photon Detection Efficiency (PDE) greater than 15% for light at 174.8 ± 10.2 nm (scintillation light in liquid xenon [47]), (ii) relative fluctuation of the mean number of correlated avalanches per pulse (within a time window of 1 μs after the trigger pulse[2]) below 0.4, (iii) dark-noise rate lower than 50 Hz/mm^2, (iv) electronic noise (equivalent noise charge) smaller than 0.1 Photo-electron Equivalent (PE) r.m.s.

[1] This chapter was published in [54] and [67]. Its content was adapted to fit the thesis structure.

[2] In nEXO, the maximum charge integration time after the trigger will be 1 μs, as introduced in Chapter 2.

According to the discussion introduced in Chapter 2, the first three requirements are in fact sufficient to achieve an energy resolution of 1% for the ($0\nu\beta\beta$) decay of ^{136}Xe. In Fig. 2.20, it was shown that these requirements could be met with FBK VUV HD 1 SiPMs developed by Fondazione Bruno Kessler (FBK, Trento, Italy) for nEXO. The aim of this chapter is to assess the performance of Hamamatsu VUV4 Multi-Pixel Photon Counter (MPPC) (S/N: S13370-6152) developed for application in liquid xenon as a possible alternative solution to FBK SiPMs. The devices tested have a micro-cell pitch of 50 μm and an effective photosensitive area of 6×6 mm^2. Similar characterizations for the same generation of Hamamatsu VUV4 devices, but with different series, can be found in [16, 68].

3.2 Experimental Details

3.2.1 Hardware Setup

A setup was developed at TRIUMF to characterize the response of SiPMs at VUV wavelengths, as illustrated in Fig. 3.1. The measurement setup is installed in a dark box, kept under constant nitrogen gas purge and mounted on an optical platform. Humidity was monitored constantly with a HH314A Omega controller [69]. Light from a Hamamatsu L11035 xenon flash lamp [70] shines through: (i) a 1 mm diameter collimator, (ii) a VUV diffuser (Knight optical DGF1500 [71]) and (iii) a CaF2 lens (eSource optic CF1220LCX [72]). The diffuser is placed at the focal point of the lens in order to uniformly illuminate the lens and to produce a parallel beam. The whole assembly is housed in a Radio-Frequency (RF) copper box (RF Shield #1 in Fig. 3.1) to shield against electromagnetic emissions from the lamp. Additionally, the VUV light passes through a set of bandpass filters, used to select the desired portion of the lamp emission spectrum and a second 1 mm diameter collimator, close to the SiPM surface (Sec. 3.2.2). Prior to filters and collimator, the light beam passes through a beam splitter, allowing to simultaneously illuminate the VUV4 MPPC and a Newport 918D-UV-OD3 Photo-Diode (PD) [73], used to monitor the xenon flash lamp light stability. The SiPM is mounted inside a second RF shielding copper box (RF Shield #2 in Fig. 3.1) placed on a movable optical arm which allows for remote positioning of the SiPM in the x-y plane. A liquid ni-

trogen controlled cold finger adjusts the temperature of the SiPM down to 163 K[3]. An additional UV-sensitive R9875P Hamamatsu PMT [70] is also mounted on the x-y stage and used during PDE measurements to calibrate the absolute light flux at the location of the SiPM. The SiPM and PMT can be interchanged remotely. A CAEN DT5730B Digitizer [74] and a Maximum Integrated Data Acquisition System (MIDAS)-based control system [75], are used for signal digitalization and constitute the Data AcQuisition System (DAQ) of the current setup. The SiPM signal is amplified by two MAR6-SM+ amplifiers in series [76]. The acquisition trigger module, the PD controller, the filters controller, the x-y stage controller, the PMT and the SiPM power supply are all placed outside the dark box.

3.2.2 Light Filtering Scheme

A set of 4 narrow bandpass filters with transmission nominally centered at 180 nm selects the desired portion of the lamp emission spectrum and attenuates the xenon flash lamp light intensity. Two of the filters are 25180FNB from eSource OPTICS [72] and two are 180-NB-1D from Pelham Research Optical LLC [77]. The typical peak transmission of these filters at 180 nm is on the order of 20%. In order to establish the transmitted wavelength distribution, each filter was characterized using a VUV spectrometer (Resonance TR-SES-200 [78]). The filtered spectrum is shown in Fig. 3.2. It has a mean wavelength of 189 nm and a Full Width Half Maximum (FWHM) of 13 nm.

3.2.3 Beam Position Mapping

The VUV4 MPPC and the PMT, used for absolute light calibration, have different Photosensitive Area (PA)s of 6×6 mm^2 and 50.24 mm^2, respectively. For the PDE calculations it is usually necessary to normalize SiPM and PMT measurements by their photosensitive areas. This correction can be neglected if the cross section of the impinging beam is smaller than the SiPM and PMT photosensitive areas. To verify this condition, the collimated light beam was mapped with respect to the surface of both photon-sensors. Particular attention was devoted to the SiPM Beam map, since the SiPM represents the smaller of the two sensors. The beam

[3] The temperature stability was found to be ± 1 K.

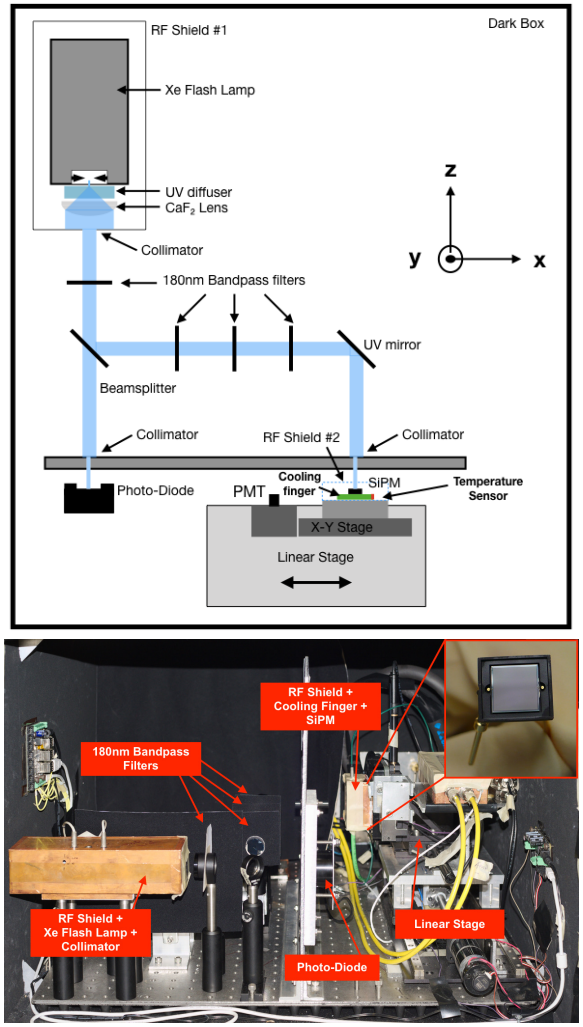

Figure 3.1: Hardware setup used for the characterization of the Hamamatsu VUV4 MPPC.

map of the SiPM is shown in this section while the beam map of the PMT is introduced in Sec. 3.3.5. In both cases the beam map was achieved by moving the SiPM (or the PMT) in the x-y plane (Fig. 3.1) in increments of 0.5 mm, and by measuring (noise subtracted) the counting rates detected by the device at each position. A typical beam-map for the SiPM is shown in Fig. 3.3. To size the diameter of the beam: d_{BEAM}, at the SiPM and PMT location, the x and y projections of the

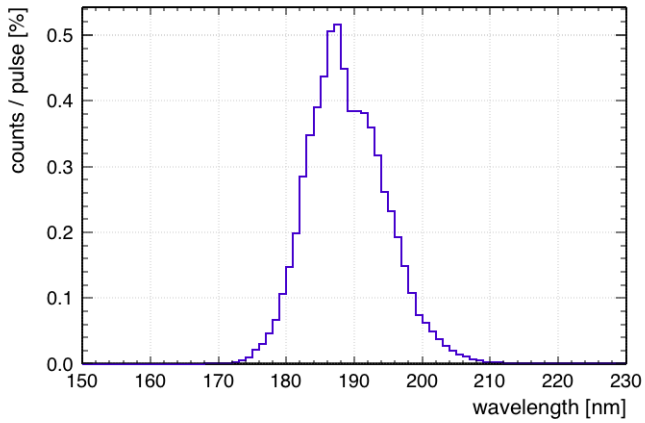

Figure 3.2: Filtered xenon flash lamp spectrum measured after application of the 4 VUV filters. The shoulder effect around 190 nm is due to the combination of the original xenon flash lamp spectrum and the different filters transmissions.

beam map are compared with a Monte-Carlo model (MC). Based on the collimator size and shape described in Sec. 3.2.1 and Fig. 3.1, the beam map should be the convolution between a circular beam and a square SiPM whose response in the MC model is assumed uniform across its surface. Different x and y profiles were created by letting d_{BEAM} float, and a likelihood method was used to determine the combination that best fits the data, shown in Fig. 3.4. The best fit beam diameter at the SiPM (or PMT) location is 1.2 $\pm$ 0.2 mm. This result confirms that: (i) the beam cross-section is smaller than the SiPM and PMT photon-sensitive areas and therefore an area correction can be neglected during efficiency measurements, (ii) the SiPM response is uniform across its surface.

3.2.4 Collected Data and Trigger Configurations

The VUV4 MPPC characteristics, as a function of the temperature, were investigated in the range 163 K $\leq$ T $\leq$ 233 K. The collected data can be divided into two types: dark data, where the SiPM was shielded from any light source, and xenon flash lamp data. For dark measurements (Sec. 3.3.2, Sec. 3.3.3 and Sec. 3.3.4) the SiPM copper box (RF shield # 2 in Fig. 3.1) was closed, enabling

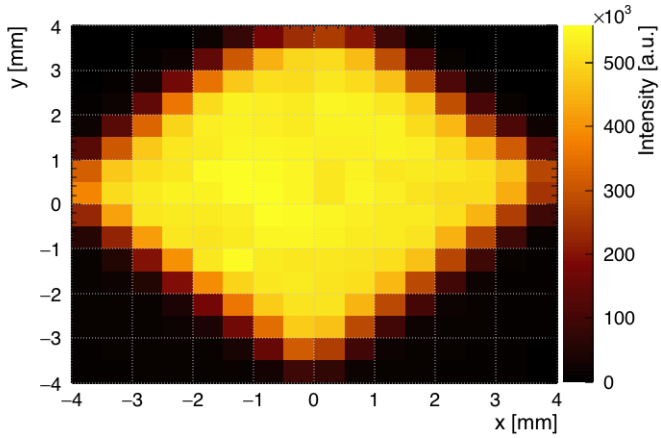

Figure 3.3: Position mapping of the VUV beam at the SiPM location. The SiPM was moved in the x and y coordinates of Fig. 3.1 at increments of 0.5 mm in each direction.

data-collection at temperatures below 233 K. The DAQ system was set to trigger on individual SiPM pulses with a DAQ threshold above the noise. For each trigger, the DAQ saves the event with a total sample window of 20 µs, split into 4 µs of pre-trigger and 16 µs of post-trigger samples. The long post-trigger window is necessary in order to measure delayed correlated pulses, while the long pre-trigger window ensures that no tail from previous pulses persists. Dark data were collected at different temperatures and over voltages. For xenon flash lamp data (PDE measurements in Sec. 3.3.5), the DAQ was externally triggered by pulses from a waveform generator which also fired the xenon flash lamp. Furthermore, the SiPM RF shielding box was opened, allowing light to reach the SiPM. PDE measurements were performed at 233 K to prevent residual water vapour condensation. The external trigger had a frequency of 500 Hz.

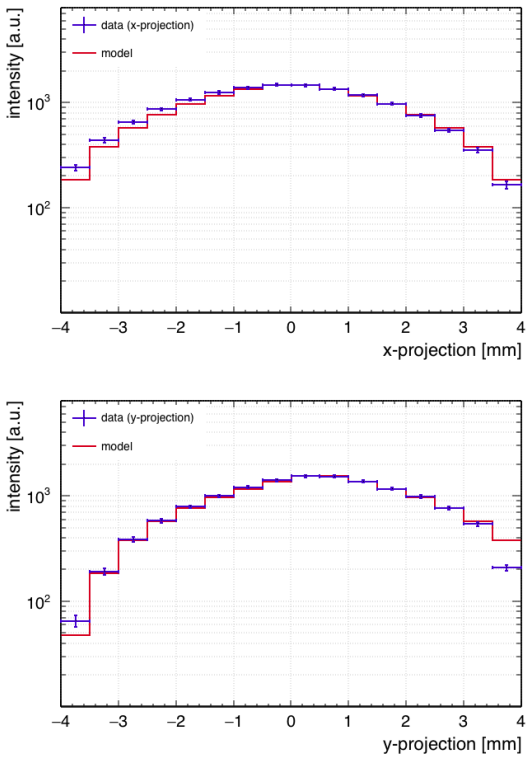

Figure 3.4: Comparison between the measured beam map x-y projections (Blue) and the Monte Carlo model (Red) for the x-projection (Top) and y-projection (Bottom) of the beam map of Fig. 3.3. The beam diameter was estimated to be 1.2±0.2 mm at the SiPM and PMT location, indicating that the beam cross-section is smaller than the SiPM and PMT photon-sensitive surface area. The χ^2 test for the two projections gives respectively a χ^2/NDF of 1.48 for the x projection and a χ^2/NDF of 1.24 for the y projection where NDF is the Number of Degree of Freedom. The biggest deviation between the model and the measurements is evident for points at the edge of the SiPM, where the relative error of the measurement increases due to a worsening of the signal to noise ratio.

3.3 Experimental Results

3.3.1 Signal Pulse Fitting Procedure

The collected dark data were analyzed at the pulse level in order to resolve individual PE pulses. A ROOT-based [79] waveform analysis toolkit was developed, similar to the one reported in [80]. See Fig. 3.5.

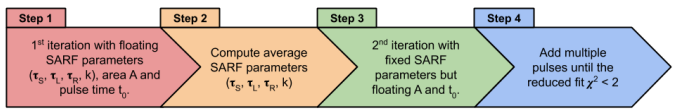

Figure 3.5: Schematic representation of the waveform analysis toolkit developed for this study. See text for a detailed explanation.

The implemented algorithm relies on a χ^2 minimization to identify and fit SiPM pulses. The Single Avalanche Response Function (SARF) was parametrized using the following equation, which accounts for the presence of two time constants in the SiPM pulse shape [60]:

$$V(t) = \mathrm{A} \times \left[\frac{1-k}{\tau_S} \left(e^{-\frac{t-t_0}{\tau_S+\tau_R}} - e^{-\frac{t-t_0}{\tau_R}} \right) + \right. \\ \left. + \frac{k}{\tau_L} \left(e^{-\frac{t-t_0}{\tau_L+\tau_R}} - e^{-\frac{t-t_0}{\tau_R}} \right) \right] \tag{3.1}$$

where: τ_R is the pulse rise time, A is the pulse area (proportional to the pulse charge, see Sec. 3.3.2), t_0 is the pulse time, τ_S and τ_L are the short and long pulse fall time constants, respectively. k is the relative contribution of the two fall time components in the SiPM pulse shape: $0 \leq k \leq 1$. For each over voltage and temperature the collected dark pulses were fitted in a multistage algorithm. First, a pulse-finding algorithm identifies and fits single avalanche pulses to extrapolate the average SARF parameters (τ_R,τ_S,τ_L and k), according to Eq. 3.1. The SiPM pulse shape is then set by fixing these parameters to their estimated average values. Finally, a second fit iteration is performed with fixed pulse shape to improve the estimation of pulse time and area. For fits exceeding a certain threshold of reduced χ^2, test pulses are added iteratively to the fit. The new pulse combination is kept

permanently if the reduced χ^2 of the new fit improves significantly. Else, the test pulses are discarded. The last step of the algorithm improves the capability to identify overlapping pulses (more details in [81]). As an example, we report in Fig. 3.6 the charge distribution of first pulses following single PE primary pulses (also called trigger or prompt pulses) as a function of the time difference with respect to their primary pulse recorded at T=163 K and for an over voltage of 5.1 ± 0.2 V.

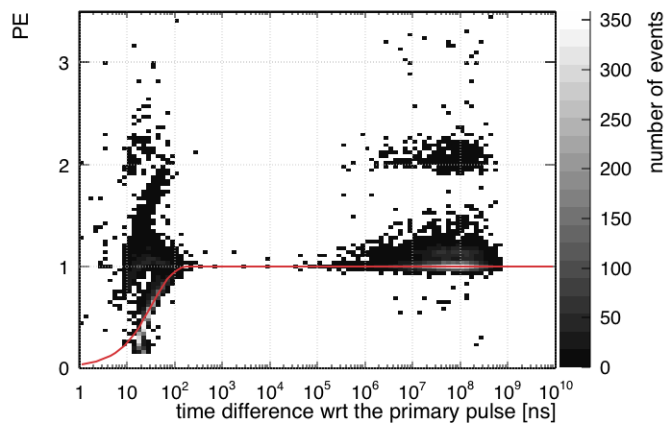

Figure 3.6: Charge distribution (normalized to the average charge of 1 PE pulses) of first pulses following single PE trigger pulses as a function of the time difference with respect to (wrt) their primary pulse for T=163 K and for an over voltage of 5.1 ± 0.2 V. The grey scale represents the number of events in each bin on a logarithmic scale. The solid red line shows a fit of the afterpulsing events and is used to measure the recovery time of one cell, equal to 35 ± 4 ns.

3.3.2 Single PE Gain and Breakdown Voltage Extrapolation

Single PE dark pulses were used to measure the single PE SiPM gain as a function of the SiPM temperature. The single PE (amplified) pulse charge Q can be defined as:

$$Q \equiv \left(\frac{\mathrm{IDR}}{2^{14}}\right) \times \left(\frac{\overline{\mathrm{A}}_{1\,\mathrm{PE}} \times 10^{-9}}{\mathrm{R}}\right) \tag{3.2}$$

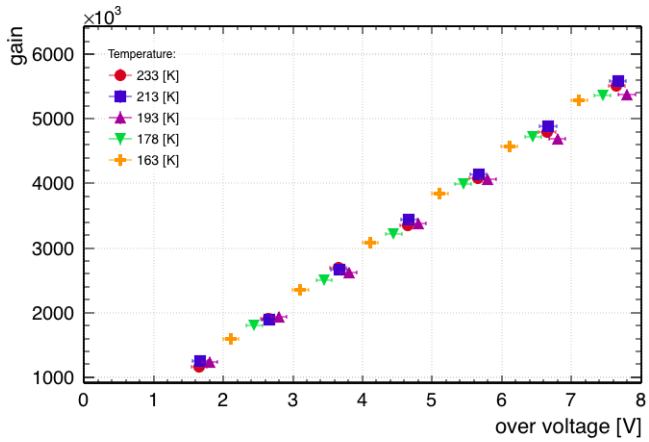

Figure 3.7: Measured single PE gain (Eq. 4.3) as a function of the over voltage for different SiPM temperatures.

where: IDR is the Input Dynamic Range of the digitizer (0.5 V), $\overline{\mathrm{A}}_{1\ \mathrm{PE}}$ is the average area (Eq. 3.1) of the fitted digitizer signals for 1 PE pulses (measured in LSB $\times$ ns [74]), and R is the amplifier load resistance (R=50 Ω). Therefore, the single PE (un-amplified) gain $\mathrm{G}_{1\ \mathrm{PE}}$ can be extracted from Q using the following equation:

$$\mathrm{G}_{1\ \mathrm{PE}} = \frac{Q}{g_{\mathrm{AMP}} \times q_E} \tag{3.3}$$

where g_{AMP} is the gain of the amplifier (measured to be 142 ± 2)[4] and q_E is the electron charge. In agreement with [82], the gain was found to increase linearly with the bias voltage V with a measured gradient of $(72.4 \pm 3.7) \times 10^4 \frac{1}{\mathrm{V}}$. From the single PE gain it is possible to extrapolate the single PE (un-amplified) charge defined as $Q_{1\ \mathrm{PE}} \equiv q_E \times \mathrm{G}_{1\ \mathrm{PE}}$. The single PE (un-amplified) charge, as a function of the bias voltage, was then linearly fitted as $Q_{1\ \mathrm{PE}} = C_D \times (V - V_{BD})$, in order to extract: (i) the single SiPM cell capacitance C_D and (ii) the Breakdown Voltage V_{BD} defined as the bias voltage at which the SiPM single PE gain (or charge) is zero.

[4]The amplifier gain was computed by applying a step voltage to a precision capacitor in order to inject a known charge into the SiPM amplifier input (*i.e.* Q_{IN}). The output charge was then computed from the digitized amplifier output waveform (*i.e.* Q_{OUT}). The amplifier gain follows as the ratio between the final integrated charge and the input known charge as $g_{\mathrm{AMP}} = \frac{Q_{\mathrm{OUT}}}{Q_{\mathrm{IN}}}$.

The breakdown voltage is found to linearly depend on the SiPM temperature with a measured gradient of $50 \pm 2\ \frac{\mathrm{mV}}{\mathrm{K}}$. At 163 K it is measured to be $V_{BD} = 44.9 \pm 0.1$ V. The average cell capacitance, extrapolated from the fit, is $C_D = 116 \pm 6$ fF with no observed temperature dependence in the analyzed temperature range. Moreover, the total SiPM capacitance was measured using a capacitance meter (Wayne Kerr 6440B [83]), with an extracted single cell capacitance of $C_D = 104 \pm 10$ fF. The gain measurements are shown in Fig. 3.7 as a function of the over voltage for different SiPM temperatures.

3.3.3 Prompt Pulse Charge Distribution

The pulse-charge distribution was studied using dark data and prompt pulses[5] with the SiPM set at different over voltages and temperatures. The single (and multi) PE charge response of prompt pulses follows the shape of a Gaussian distribution, where the width of the distribution corresponds to the charge resolution combination of the electronic noise and SiPM gain fluctuations. However, we have observed that all the charge peaks show a shoulder-like component to the right of the expected Gaussian charge distribution. This feature is observed to be highly dependent on over voltage, as shown in Fig. 3.8 for T = 233 K and 163 K. The shape of the shoulder and its dependence on over voltage were further investigated. We observed that the shape of the pulses which are contributing to the shoulder is consistent with that of single PE with a higher integrated charge. Based on these observations, this feature could arise from fast (<4 ns) correlated avalanches (afterpulse) which do not get resolved from their parent primary pulse by the DAQ system. This effect could also be explained by a discrepancy in gain between micro-cells in the device.

3.3.4 Noise Analysis

Dark Noise (DN) and Correlated Avalanche noise (CA) are among the crucial parameters that characterize SiPMs. We refer the reader to Chapter 2 for a detailed explanation of the different sources of noise in SiPMs. The DN rate of the Hamamatsu VUV4 MPPC as a function of the applied over voltage for different

[5] We define prompt pulse as the first SiPM pulse in each waveform recorded by the DAQ

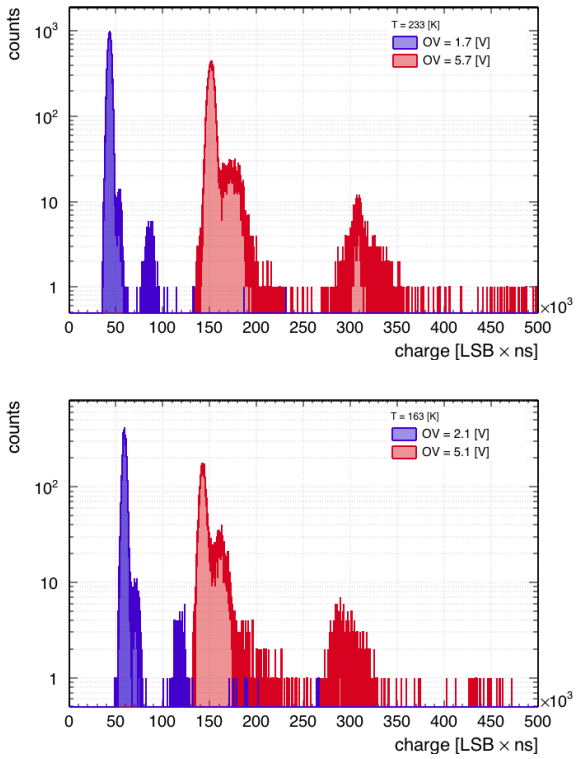

Figure 3.8: Charge distribution for prompt pulses obtained using dark data for different SiPM temperatures and over voltages (Top: T=233 K. Bottom: T=163 K). All the charge peaks show a shoulder-like component to the right of the expected Gaussian charge distribution. This feature appears to be highly dependent on the over voltage.

SiPM temperatures, is presented in Sec. 3.3.4.2. The subset of the CAs constituted by afterpulses and Delayed CrossTalk events (DeCT) is named Correlated Delayed Avalanches (CDAs). In nEXO the maximum charge integration time after the trigger pulse will be 1 µs. The number of CAs and CDAs per primary pulse in this time window as a function of the applied over voltage for different SiPM temperatures, is reported in Sec. 3.3.4.1 and Sec. 3.3.4.2, respectively. Direct CrossTalk (DiCT) is discussed in Sec. 3.3.4.3. It is worth recalling that the SiPM noise was studied using dark data, taken with the SiPM shielded from any light source (Sec. 3.2.4).

3.3.4.1 Number of Correlated Avalanches per Pulse

In order to reach the nEXO design performance, the relative fluctuation of the mean number of CAs per primary pulse must be below 0.4, within a time window of 1 μs after the primary pulse. A higher value would result in worsened energy resolution. The average number of CAs per pulse is measured by directly con-

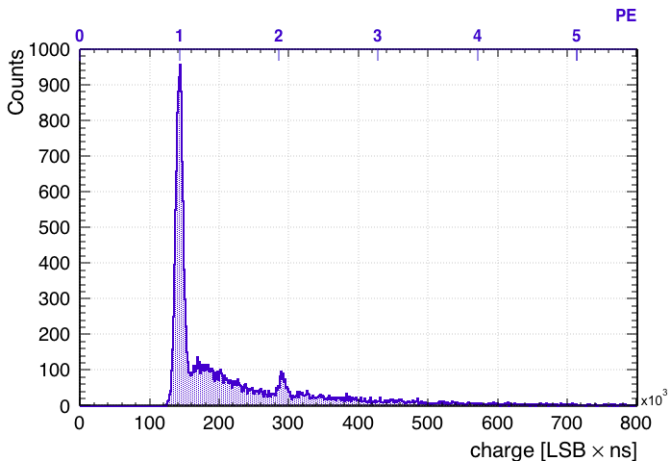

Figure 3.9: Histogram of the baseline subtracted integral of collected dark waveform for an over voltage setting of 5.1 ± 0.2 V and a temperature of 163 K. Each waveform recorded by the DAQ is integrated in the range [0-5]μs. The trigger pulse is at 4μs and no pulses are present in the pre-trigger region ([0-4]μs). The edge next to the 1 PE Gaussian peak is a combination of shoulder-like events (as reported in Fig. 3.8) and waveform with after-pulses.

structing a histogram of the baseline subtracted integral of collected dark waveform in the range $[0-5]$ μs and normalizing it to the average charge of 1 PE pulses, as discussed in [1] (An example is reported in Fig. 3.9). In the absence of correlated noise, the mean of this histogram should be exactly 1. However, each avalanche has a non-zero probability of being accompanied by correlated avalanches causing the mean of the waveform integral histogram to be larger than unity. The excess from unity can be then used to measure (in unit of PE) the average number of CAs per pulse in the 1 μs interval after the trigger pulse: $\langle\Lambda\rangle$. The $\langle\Lambda\rangle$ number is reported in Fig. 3.10, for different SiPM temperatures and over voltages. At low over voltages

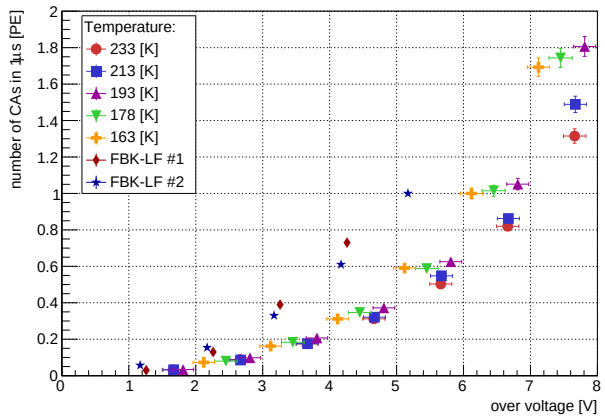

Figure 3.10: Number of Correlated Avalanches (CAs) per primary pulse within a time window of 1 μs after the trigger pulse as a function of the applied over voltage for different SiPM temperatures. FBK-LF #1 and #2 are instead the number of CAs per pulse, always in a time window of 1 μs after the trigger pulse for two FBK-LF SiPMs.

$\langle\Lambda\rangle$ doesn't show an evident temperature dependence; a minor deviation is, however, observed at higher over voltages. Similar trends are reported for other SiPMs by other investigations [84]. For comparison, in Fig. 3.10 we have also reported the average number of CAs for two FBK VUV HD 1 SiPM (called FBK-LF #1 and FBK-LF #2 in figure due to their fabrication technology, as shown in Chapter 2), characterized in [1]. The Hamamatsu VUV4 has a considerably lower $\langle\Lambda\rangle$ than FBK-LF. For reference, at T=163 K and at 3.1 ± 0.2 V of over voltage we measure $\langle\Lambda\rangle = 0.161 \pm 0.005$ for the Hamamatsu VUV4[6], while the FBK LF #1 and #2 at T = 163 K and 3.26 V and 3.17 V have a $\langle\Lambda\rangle$ equal to 0.39 and 0.33, respectively. Fig. 3.11 shows instead the Root Mean Square (RMS) (often called standard deviation) of the number of correlated avalanches per primary pulse within a time window of 1 μs after the trigger pulse (i.e. σ_Λ), as a function of the applied over voltage, for different SiPM temperatures. Differently from Fig. 3.10, in Fig. 3.11 we couldn't include the RMS error of the FBK LF data, since in [1] it was only

[6] 3.1 ± 0.2 V is the closest measured points for which the requirement on relative fluctuation of the number of CAs in 1 μs is satisfied. At this over voltage and temperature the electronics noise was measured to be 0.064 PE.

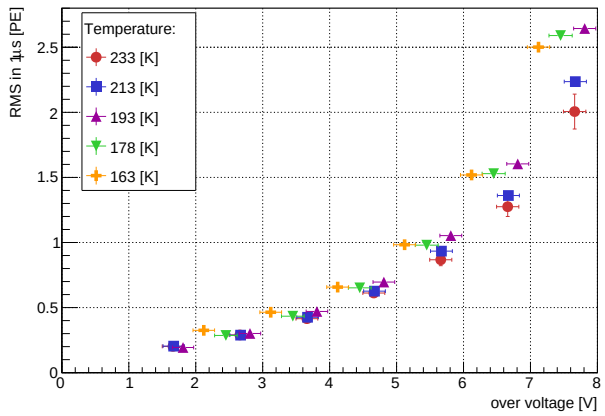

Figure 3.11: Root Mean Square Error (RMS) of the number of Correlated Avalanches (CAs) per primary pulse within a time window of 1 µs after the trigger pulse as a function of the applied over voltage for different SiPM temperatures.

reported the mean number of correlated avalanches in 1 µs, without any additional information of the data RMS error. The high values in Fig. 3.11 show as there is a significant amount of fluctuations in the number of correlated avalanches between different events. For instance at 163 K and at 3.1 ± 0.2 V of over voltage the mean number of correlated avalanche is $\langle \Lambda \rangle = 0.161 \pm 0.005$, while its RMS error is 0.46 ± 0.01. Fig. 3.12 reports the relative fluctuation of the number of CAs in 1 μs at 163 K, useful for nEXO operation, defined as

$$\text{Ratio} \equiv \frac{\sigma_\Lambda}{1 + \langle \Lambda \rangle} \tag{3.4}$$

In order to meet the nEXO requirements (Sec. 3.1), the Hamamatsu VUV4 can be operated at T=163 K up to about 3.2 V of over voltage keeping the relative fluctuation of the number of CAs in 1 μs smaller than 0.4. For reference at 3.1 ± 0.2 V of over voltage we measure a relative fluctuation of the mean number of CAs in 1 μs equal to 0.39 ± 0.01.

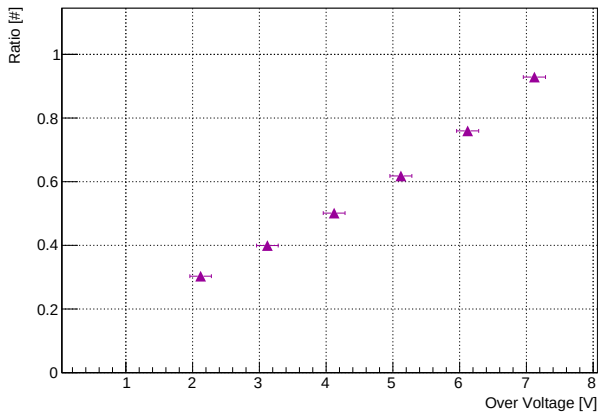

Figure 3.12: Relative fluctuation of the number of CAs in 1 μs measured at 163 K and derived with Eq. 3.4 from the data of Fig. 3.10 and Fig. 3.11.

3.3.4.2 Dark Noise Rate and Number of Correlated Delayed Avalanches per Pulse

DN and CDAs events can be distinguished by studying the time distribution of events relative to the primary pulse using a method, described in [85], that requires the charge of the primary pulse to be a single PE equivalent. The observed pulse rate $\mathrm{R}(t)$ is then computed as a function of the time difference t from the primary pulse ($t = 0$) as:

$$\mathrm{R}(t) = \mathrm{R}_{\mathrm{DN}}(t) + \mathrm{R}_{\mathrm{CDA}}(t) \tag{3.5}$$

where R_{DN} is the rate of dark noise pulses and $\mathrm{R}_{\mathrm{CDA}}$ is the rate of the CDAs per pulse. An example of the measured time distribution for a given over voltage and for two different temperatures is reported in Fig. 3.13. The DN rate can then be estimated from Fig. 3.13, performing a weighted mean of the asymptotic rate at long times[7]. The measured DN rates, for different SiPM temperatures, are shown in Fig. 3.14 as a function of the over voltage. For the same temperature and OV setting reported in Sec. 3.3.4.1 (163 K, 3.1 ± 0.2 V of OV), the DN rate is measured to be 0.137 ± 0.002 Hz/mm^2, which satisfies nEXO requirements (Sec. 3.1). By

[7]Each point in the mean was weighted with its error derived as reported in [85].

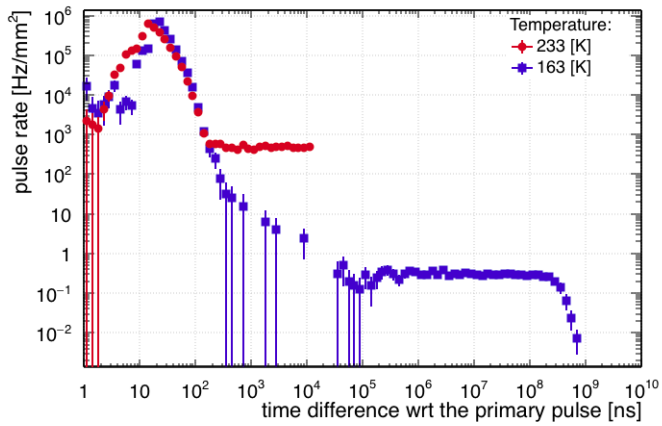

Figure 3.13: Observed pulse rate $R(t)$ normalized by the SiPM photon sensitive area as a function of the time difference with respect to (wrt) the primary pulse for a temperature of 163 K (5.1 ± 0.2 V of over voltage) (Blue) and 233 K (5.7 ± 0.2 V of over voltage) (Red). At 233 K, to avoid ADC dead time corrections due to the high self trigger DN rate, the time differences were computed only between pulses inside the same DAQ window (maximum time difference: 16µs)

applying Eq. 3.5 to the observed pulse rate (e.g. Fig. 3.13), it is possible to compute the expected number of CDAs per pulse in a fixed time window of length Δt after the trigger pulse as:

$$N_{CDA}(\Delta t) = \int_0^{\Delta t} \Big(R(t) - R_{DN}(t) \Big) \, dt \tag{3.6}$$

where R_{DN} is the measured DN rate as reported in Fig. 3.14. The measured average number of CDAs per pulse in the 1 µs window after the trigger pulse, for different SiPM temperatures and over voltages is reported in Fig. 3.15. For 163 K and 3.1 ± 0.2 V of OV, the average number of CDAs per pulse in 1 µs is 0.178 ± 0.003. Finally, it is worth noting that the number of CDAs, extrapolated in this section, cannot be compared directly with the number of CAs (Sec. 3.3.4.1). The number of CDAs is in fact derived, accordingly to [85], considering only the time differences of delayed events with respect to their primary pulse while the number of CAs accounts instead also for their different charge.

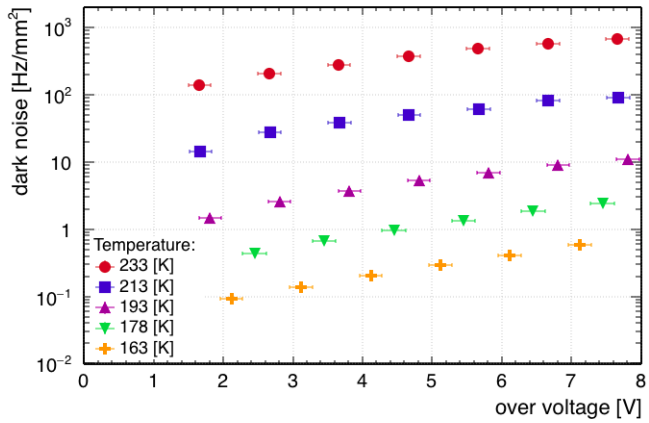

Figure 3.14: Dark Noise (DN) rate normalized by the SiPM photon sensitive area as a function of the applied over voltage for different SiPM temperatures.

3.3.4.3 Number of Additional Prompt Avalanches

Based on the measured dark noise rate reported in Sec. 3.3.4.2, and assuming Poisson statistics, the probability of having two dark noise pulses occurring within few nano-seconds is negligible. Therefore, the collected dark data can be used to investigate Direct CrossTalk (DiCT). DiCT occurs when photons generated during a triggered avalanche in one micro-cell promptly travel to the amplification region of neighboring micro-cells, where they induce a secondary avalanche. This mechanism happens over pico-seconds [64] and it mimics a multiple PE signal, thus biasing the photon counting ability of the device. The charge distribution of the prompt pulses obtained from the dark data (Sec. 3.3.3) can be used to determine the mean number of Additional Prompt Avalanche (APA)s, $\mathrm{N_{APA}}$, due to Direct CrossTalk :

$$\mathrm{N_{APA}} = \frac{1}{N}\sum_{i=1}^{N}\frac{\mathrm{A}_i}{\overline{\mathrm{A}}_{1\ \mathrm{PE}}} - 1 \tag{3.7}$$

where A_i is the charge of the prompt pulse i (Sec. 3.3.1), $\overline{\mathrm{A}}_{1\ \mathrm{PE}}$ is the average charge of 1 PE pulses and N is the number of prompt avalanches analyzed. The $\mathrm{N_{APA}}$ number, in unit of PE, as a function of the over voltage and for different SiPM

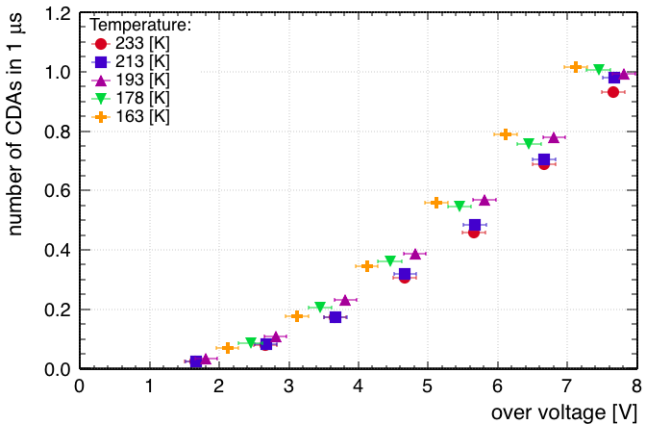

Figure 3.15: Number of Correlated Delayed Avalanches (CDAs) per primary pulse within a time window of 1 µs after the trigger pulse as a function of the applied over voltage for different SiPM temperatures.

temperatures, is reported in Fig. 3.16. For 163 K and for 3.1 $\pm$ 0.2 V of OV we measure a mean number of additional prompt avalanches, due to direct CrossTalk, equal to 0.032 ± 0.001. The small amount of N_{APA} can also be understood looking at Fig. 3.6 and Fig. 3.9 where 3 PE events are greatly suppressed.

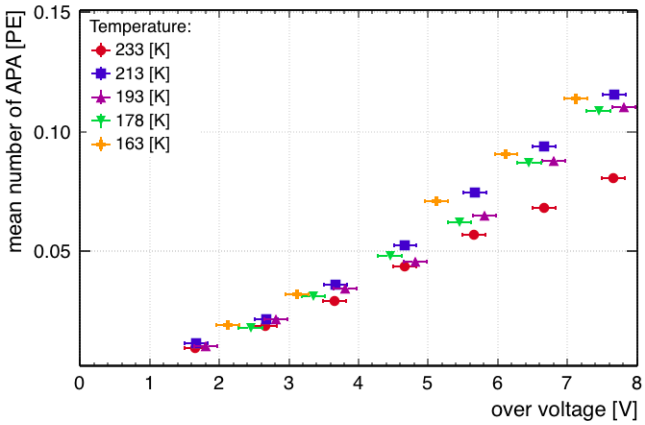

Figure 3.16: Number of Additional Prompt Avalanches (APAs) as a function of the over voltage for different SiPM temperatures.

3.3.5 Photon Detection Efficiency

To meet nEXO requirements, the SiPM PDE must be $\geq 15\%$ for liquid xenon scintillation wavelengths (174.8 ± 10.2 nm [47]). In this chapter, the PDE was measured using a filtered pulsed xenon flash lamp enabling measurements free from correlated avalanches [58]. As shown in Sec. 3.2.2, the mean wavelength after filtering is 189 ± 7 nm. The generated flash pulse has a width $\sim 1\mu$s, which prevents room temperature measurements, as the dark noise would overwhelm the light signal. For this reason, PDE data were taken with the SiPM temperature set at 233 K. The PDE was measured using an experimental technique similar to the one described in [58]. The light flux was assessed using a calibrated PMT (Sec. 3.2.1) with no corrections applied for the different photosensitive areas of the two devices (Sec. 3.2.3). The average number of photons detected by the SiPM ($\mu_\gamma^{\mathrm{SiPM}}$) was measured by counting the number of lamp flashes in which no pulses were detected (N_0). Using Poisson statistics $\mu_\gamma^{\mathrm{SiPM}}$ can be expressed as:

$$\mu_\gamma^{\mathrm{SiPM}} = -\ln\left(\frac{N_0}{N_{\mathrm{TOT}}}\right) - \mu_{\mathrm{DN}} \tag{3.8}$$

where N_{TOT} is the total number of lamp flashes. This method is independent of correlated avalanches and it requires only correcting for the average number of dark noise pulses in the trigger window (μ_{DN}). The same analysis was applied to the reference PMT (Hamamatsu R9875P, Sec. 3.2.1) in order to measure the average number of photons detected by the PMT ($\mu_\gamma^{\mathrm{PMT}}$) and then extrapolate, using the PMT Quantum Efficiency (QE) and Collection Efficiency (CE), the effective number of photons produced by the pulsed xenon flash lamp at the SiPM and PMT surface: N_γ. The PMT QE expresses the probability of photon-electron emission when a single photon strikes the PMT photocathode [86]. The QE reported by Hamamatsu for this phototube is 16.5 ± 2.1 %. The PMT CE expresses the probability that the generated photon-electron will land on the effective area of the first PMT dynode and start the amplification process [86]. The CE of this phototube was determined by Hamamatsu to be 71% without any estimate of the uncertainty. The PMT Beam map is reported in Fig. 3.17. Conservatively, in agreement with the discussion done in Sec. 3.2.3 and with [1], we assume a 10 % error for the CE of this PMT (i.e. 71 ± 10 %) to account for the non-uniformity of the photon

collection at the photo-cathode. The number of incident photons N_γ on the PMT

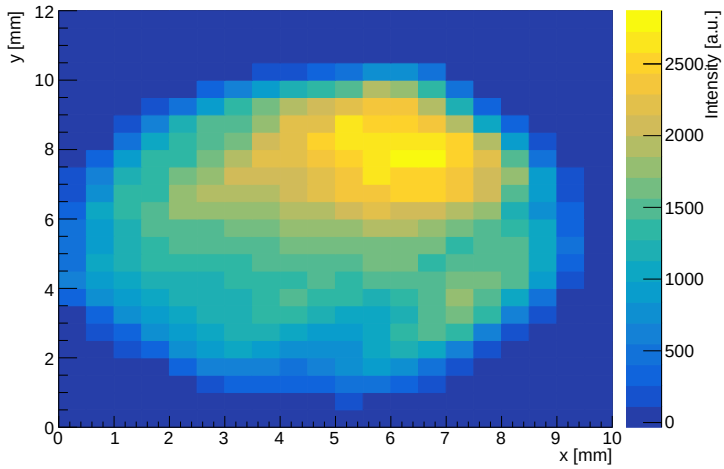

Figure 3.17: Position mapping of the VUV beam at the PMT location. The PMT was moved in the x and y coordinates of Fig. 3.1 at increments of 0.5 mm in each direction.

surface can then be obtained as:

$$N_\gamma = \left(\frac{\mu_\gamma^{\mathrm{PMT}}}{\mathrm{CE} \times \mathrm{QE}} \right) \tag{3.9}$$

The SiPM PDE is in turn obtained as:

$$\mathrm{PDE}_{\mathrm{SiPM}} = \left(\frac{\mu_\gamma^{\mathrm{SiPM}}}{N_\gamma} \right) \tag{3.10}$$

The measured PDE as a function of the over voltage is shown in Fig. 3.18 for two different VUV4 devices labelled VUV4 #1 and VUV4 #2. VUV4 #2 is the device for which DN, CAs, CDAs and APAs are reported in the previous sections of this chapter. The measured saturation PDE for VUV4 #2 and VUV4 #1 are $14.8 \pm 2.8\%$ and $12.2 \pm 2.3\%$, respectively. Both values are well below the 24 % saturation PDE advertised by Hamamatsu [87]. For comparison, we measured the PDE of one FBK LF (FBK LF # 3 in Fig. 3.18), for which the saturation PDE was

measured to be $22.8 \pm 4.3\%$, in agreement with [1] (FBK-LF #1 and #2 in Fig. 3.18, see Sec. 3.3.4.1). It is important to mention that different sources of systematic uncertainty were considered and investigated for this measurement. The PMT gain stability was found to be a negligible source of uncertainty. The stability of the light flux, monitored with a photo-diode (Sec. 3.2.1), was also found to have a negligible effect, with fluctuations within 1 %. The dominant source of systematic uncertainty is therefore the uncertainty on the PMT CE. We conclude this section by interpreting the results of the PDE measurement in the context of the nEXO experiment. There are three main differences between the experimental condition of this study and the nEXO environment: (i) wavelength, (ii) angle of incidence of the light, and (iii) temperature. Firstly, as shown in Sec. 3.2.2, the filtered wavelength distribution is about 10 nanometers higher than liquid xenon scintillation. In [87] Hamamatsu reports little wavelength dependence in this range. Secondly, as shown in Sec. 3.2.3, the angular distribution of photons at the SiPM location in the TRIUMF setup is normal to the SiPM surface. This is not the case for nEXO, for which preliminary GEANT4 optical simulations [88] show an average deviation from a normal distribution at the SiPM surface. The photon detection efficiency is likely to be lower at higher incidence angles due to increased reflectivity [58]. Finally, as explained in Sec. 3.2, the VUV4 PDE is measured at 233 K instead of liquid xenon temperature, which may affect the total PDE [89, 90]. Measurements of SiPM reflectivity to VUV light as a function of photon incident angle and wavelength are being planned with new setups properly customized to perform PDE measurements down to 163 K, as the one introduced in Chapter 4 of this thesis. These custom setups will allow us to measure the VUV4 PDE in conditions closer to those in nEXO. A lower systematic uncertainty on the VUV4 PDE will be also achieved substituting the calibrated Hamamatsu PMT with a calibrated NIST photodiode, as it will be shown in Chapter 4, due to the smaller systematic uncertainty on the provided responsivity [91] if compared with the PMT CE.

3.3.5.1 Analysis of the reflectivity of the Hamamatsu VUV4 MPPC and FBK LF SiPM

As shown in Fig. 3.18, the PDE of the Hamamatsu VUV4 MPPC is lower if compared with the one of the FBK LF SiPM. A possible explanation could

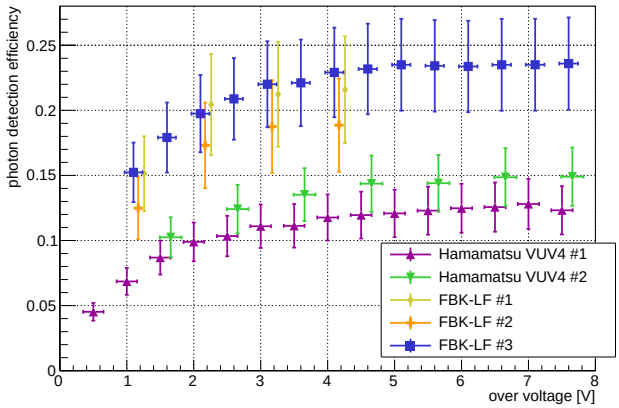

Figure 3.18: Photon Detection Efficiency (PDE) as a function of the over voltage for two Hamamatsu VUV4 MPPCs and three FBK-LF SiPMs. The Hamamatsu MPPC used throughout this chapter is the VUV4 #2. The FBK-LF #3 is a new FBK LF SiPM measured, for comparison, in the setup reported in this chapter. FBK-LF #1 and #2 are instead the FBK-LF PDE whose number of CAs is reported in Sec. 3.3.4.1 and Fig. 3.10. The error, on each point, for all the five devices accounts for the presence both to the statistical and the systematic uncertainty.

be searched in the different surface reflectivity of the two SiPMs. To investigate this aspect, the nEXO collaboration in Ref. [92] studied the reflectivity of the two SiPMs as a function of the incident wavelength and angle, as shown in Fig. 3.19 and Fig. 3.20. In particular in Ref. [92] five samples were investigated: a FBK-VUV-HD1-LF (FBK-LF) SiPM; a FBK-VUV-HD1-STD (FBK-STD) SiPM; a FBK silicon wafer and two Hamamatsu VUV4 MPPCs. The FBK SiPMs have the same dimension (10 mm $\times$ 10 mm), a pixel size of 30 μm and a fill factor of $\sim$ 73%. The FBK silicon wafer is a 6-in silicon wafer deposited by a layer of SiO_2 with a thickness of approximately 1.5 μm. This silicon wafer is identical to the one used during SiPM manufacturing and diced into 20 mm $\times$ 20 mm pieces. The two Hamamatsu VUV4 MPPCs have instead a dimensions of 6 mm $\times$ 6 mm and a pixel size of 50 μm and 75 μm, respectively. The 50 μm version is the one characterised in the previous sections of this chapter. As shown in Fig. 3.19 and Fig. 3.20, the lower efficiency of the Hamamatsu VUV4 MPPC cannot be attributed to its reflec-

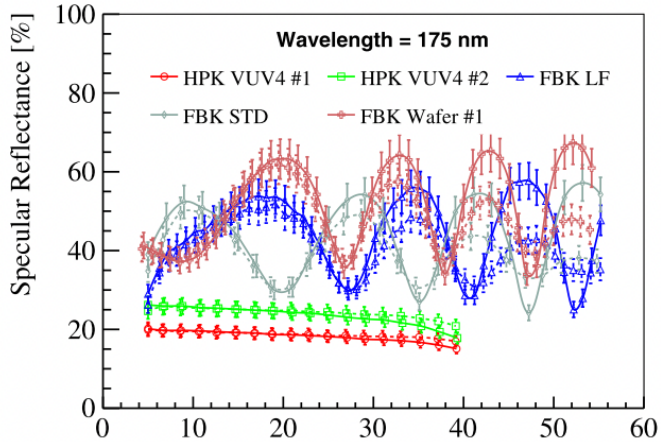

Figure 3.19: Specular reflectance as a function of the Angle of Incidence (AOI) for five samples measured at 175 nm. The wavelength is labeled on each plot, and samples are indicated by different colors. Solid lines represent light beams with s-polarization, while dashed lines indicate p-polarization. From Ref. [92].

tivity at 175 nm or 193 nm. If compared with the FBK LF SiPM, the Hamamatsu VUV4 has in fact a lower surface reflectivity and this results in a higher amount of light transmitted throw the SiO_2 coating layer at the top of the SiPM. Additionally, the FBK samples show oscillations in their specular reflectivity that are not observed for VUV4 MPPCs. This result is caused by the interference of the incident light in the thin SiO_2 layer deposited on the surface of the FBK samples. The thickness of the thin SiO_2 layer is approximately 1.5 μm, as measured by FBK. The FBK-Si-Wafer sample has a higher specular reflectance than that of the other two FBK SiPMs, due to the microstructures on the surface of SiPMs, such as traces and quenching resistors that can reduce the specular reflectance. The Hamamatsu VUV4 instead doesn't show oscillation most likely due to the thinner SiO_2 layer deposited at the top of it. Unfortunately, no information of the MPPC structure were provided by Hamamatsu.

Overall, as already noticed, the reflectivity of Hamamatsu VUV4 MPPC is lower if compared with the one of the FBK SiPM. The lower PDE of the Hamamatsu VUV4 MPPC is therefore probably due to absorption of the incident light in the not depleted region close to the surface between the SiO_2 layer and the

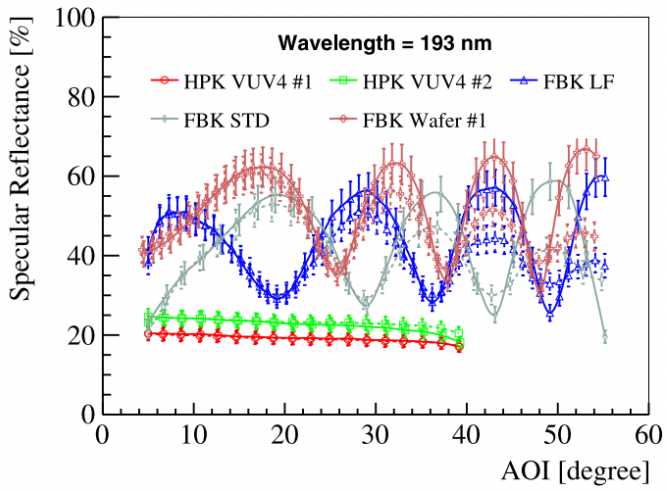

Figure 3.20: Specular reflectance as a function of the Angle of Incidence (AOI) for five samples measured at 193 nm. The wavelength is labeled on each plot, and samples are indicated by different colors. Solid lines represent light beams with s-polarization, while dashed lines indicate p-polarization. From Ref. [92].

avalanche region rather than due to light directly reflected from the silicon surface. The attenuation length of VUV photons in Silicon is in fact extremely sensitive to the location of the avalanche region that can produce noticeable differences in the final PDE, as shown for example in Chapter 5 and in Ref. [93].[8]

3.4 Conclusions

This chapter described measurements performed at TRIUMF to characterize the properties of VUV sensitive SiPMs at cryogenic temperatures. In particular, this chapter focused on the Hamamatsu VUV4 MPPC, identified as a possible option for the nEXO experiment. The results of the characterization are summarized in Table 3.1. For a device temperature of 163 K, the VUV4 dark noise

[8]The higher PDE measured by Hamamatsu could be also related to the different technique used by Hamamatsu to evaluate the VUV4 PDE. According to an internal meeting with Hamamatsu, the PDE reported in [87] was not assessed by pulse counting, but reading out instead the MPPC current under illumination. However, as shown in [94], the MPPC current is affected by CA noise and it is therefore easier to overestimate the PDE if the CA noise contribution is not accounted properly.

Quantity	Value	Unit
Dark noise rate	0.137 ± 0.002	Hz/mm^2
Number of CAs	0.161 ± 0.005	PE
Relative fluctuation of the mean number of CAs	0.39 ± 0.01	-
Number of APAs	0.032 ± 0.001	PE
Number of CDAs	0.178 ± 0.003	-
PDE VUV4 #2	13.4 ± 2.6 %	-
PDE VUV4 #1	11 ± 2 %	-

Table 3.1: Summary of the results derived for the characterization of the Hamamatsu VUV4 MPPC useful for nEXO operation. The first five measurements are reported for a temperature of 163 K and at 3.1 ± 0.2 V of Over Voltage (OV). The Photon Detection Efficiency (PDE) was measured for two Hamamatsu VUV4 devices (labelled as VUV4 #2 and VUV4 #1) at T = 233 K, for a mean wavelength of 189 ± 7 nm and at an over voltage of 3.6 ± 0.2 V and 3.5 ± 0.2 V, respectively.

rate is 0.137 ± 0.002 Hz/mm^2 at 3.1 ± 0.2 V of over voltage, a level comfortably lower than what required for nEXO (<50 Hz/mm^2). At the same over voltage setting and temperature, we measure: (i) a number of additional prompt avalanches equal to 0.032 ± 0.001; (ii) a number of correlated delayed avalanches per pulse in the 1µs following the trigger pulse of 0.178 ± 0.003, (iii) a number of correlated avalanches per pulse and a relative fluctuation of the mean number of CAs per pulse in the same time window equal to 0.161 ± 0.005 and 0.39 ± 0.01, respectively. The Dark characteristics of the Hamamatsu VUV4 MPPC are therefore consistent with the nEXO requirements up to ~ 3.2 V of over voltage. Finally, the PDE of the Hamamatsu VUV4 was measured for two different devices (labelled as VUV4 #2 and VUV4 #1) at T = 233 K. At 3.6 ± 0.2 V and 3.5 ± 0.2 V of over voltage we measure, for a mean wavelength of 189 ± 7 nm, a PDE of 13.4 ± 2.6 % and 11 ± 2 % for the two devices, corresponding to a saturation PDE of 14.8 ± 2.8 % and 12.2 ± 2.3 %, respectively. Both values are well below the 24 % saturation PDE advertised by Hamamatsu [87]. More generally, the VUV4 #1 at 3.5 V of over voltage is below the nEXO PDE requirement. The VUV4 #2 instead yields a PDE that is marginally close to meeting the nEXO specifications. This suggests

that, with modest improvements, the Hamamatsu VUV4 MPPCs could be considered as an alternative to the FBK-LF SiPMs for the design of the nEXO detector.

Chapter 4

Characterization of the FBK VUV HD 3 for nEXO

4.1 Introduction

In the previous chapter of this work we reported the characterization of the Hamamatsu VUV4 MPPC as possible candidate for the nEXO experiment. In this chapter we report the characterization of the newest generation of FBK devices: FBK VUV HD 3 Vacuum Ultra-Violet (VUV) sensitive SiPMs. Following the same procedure introduced in Chapter 3, various SiPM features such as: dark noise, gain, correlated avalanches and direct CrossTalk were measured at 163 K and compared not only with the Hamamatsu VUV4 MPPC characteristics, but also with the previous generation of FBK devices: FBK VUV HD 1, presented in [1]. Table 4.1 summarises the characteristics, useful for nEXO operation, of the two previously characterised devices. According to the nEXO SiPMs specification introduced in Chapter 2 (Sec. 2.4.2), the FBK VUV HD 1 meets the nEXO Photon Detection Efficiency (PDE) requirement at 174.8 ± 10.2 nm, while the Hamamatsu VUV4 MPPC only marginally meets the nEXO PDE requirements (Fig. 3.18). Both devices meet instead the nEXO Dark and Correlated Avalanche (CA) noise requirements at 163 K in however a different over voltage range. More precisely, the Hamamatsu VUV4 MPPC and FBK VUV HD 1 can be operated up to 3.5 V and 2.5 V of over voltage, respectively while keeping the relative fluctu-

Quantity	Value	Unit
Dark Noise Rate VUV4	0.137 ± 0.002	Hz/mm^2
Relative fluctuation of the mean number of CAs (VUV4)	0.39 ± 0.01	-
PDE VUV4	11.9 ± 1.6 %	-
Dark Noise Rate LF	0.19 ± 0.06	Hz/mm^2
Relative fluctuation of the mean number of CAs (LF)	0.44 ± 0.05	-
PDE LF	19.8 ± 2.6 %	-

Table 4.1: Summary of the results derived from Chapter 3 and [1] for the characterization of the Hamamatsu VUV4 MPPC and FBK VUV HD 1 Low Field (LF) SiPM. The Hamamatsu VUV4 dark noise rate and number of Correlated Avalanches (CAs) per pulse (in the 1µs following the trigger pulse) are reported for a temperature of 163 K and at 3.1 ± 0.2 V of over voltage. The FBK LF dark noise rate is reported for a temperature of 163 K and at 3.58 V of over voltage. The FBK LF relative fluctuation of the mean number of CAs (in the 1µs following the trigger pulse) is extrapolated, using Poisson statistics, from the mean number of CAs for a temperature of 163 K and at 3.2 V of over voltage. The Hamamatsu VUV4 PDE was measured at 233 K for an over voltage of 3.55 ± 0.1 V, while the FBK VUV HD 1 (LF) PDE was measured at 163 K for an over voltage of 3.2 ± 0.1 V.

ation of the mean number of CAs in the 1μs after the trigger pulse smaller than 0.4. The smaller operational over voltage and junction capacitance [59] of the FBK VUV HD 1, if compared with the ones of the Hamamatsu VUV4 MPPC, could be a potential issue for the nEXO light detection subsystem, due to the limited operational gain achievable with these SiPMs.

From an electronics point of view, a higher over voltage is in fact desirable, since this automatically means higher gain and better signal-to-noise ratio.

The aim of this chapter is to assess the performance of a new generation of FBK devices (FBK VUV HD 3) developed for application in liquid xenon. Additionally, we will also introduce a new technique (based on the time distribution between pulses [85]) to measure the SiPM PDE, that not only is free from correlated avalanche noise corrections, but also it allows to reduce significantly the systematic uncertainly on the measured PDE, especially in the VUV wavelength

range. At the end of this chapter we will also estimate the contribution of the Hamamatsu VUV4 MPPC and FBK VUV HD 3 SiPM to the overall nEXO energy resolution using the model introduced in Chapter 2 (Sec. 2.4.3). The cell geometry and size of the FBK VUV HD 3 are comparable with the ones of its previous generation (FBK VUV HD 1). An image of the FBK VUV HD 3 SiPM is reported in Fig. 4.1. The total number of pixel is 25500 with a pitch size of 34μm and a fill factor of 0.8 giving a sensitive area that is comparable with the one of the Hamamatsu VUV4 MPPC and equal to $\sim$ 36 mm^2. The novelty of the FBK VUV HD 3

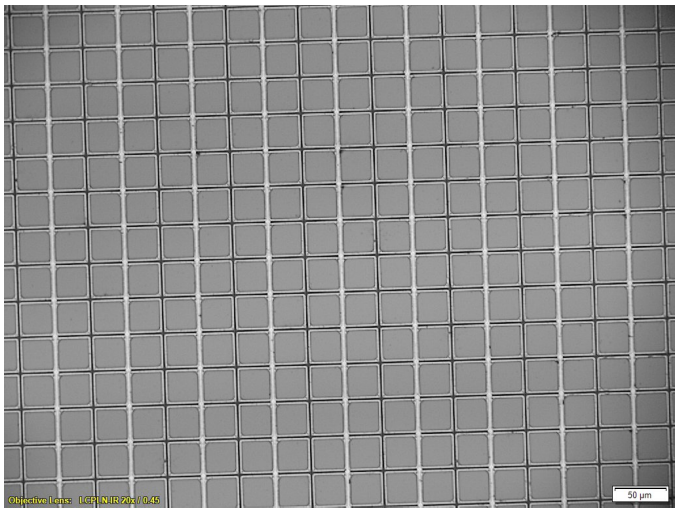

Figure 4.1: Image of a FBK VUV HD 3 SiPM.

SiPM, if compared with its previous generation, is a new triple-doping technology developed by FBK for the Darkside-20k experiment and used for the fabrication of the sensor [18]. As it will be shown in this chapter, this new technology significantly suppresses the after-pulsing probability allowing to increase the operational over voltage of these devices of 1 V, if compared with its previous generation while keeping the requirement on the relative fluctuation of the mean number of CAs to be smaller than 0.4. The absolute PDE of this device could not be finalized in this work due to an ongoing study of the light beam profile in the new commissioned setup. The confinement of the beam inside the photosensor area is in fact necessary to precisely measure the sensor efficiency. If the PDE of the FBK VUV HD 3 will be the same of its previous generation, it will allow to consider this device, with its

improved correlated avalanche noise contribution, as an excellent candidate for the nEXO light detection subsystem.

4.2 Experimental Details

4.2.1 Hardware Setup

A new setup called Vacuum Emission Reflectivity Absorption (VERA) was developed at TRIUMF to characterize the response of SiPMs at VUV wavelengths. A schematic representation of the setup is reported in Fig. 4.2. VERA consists

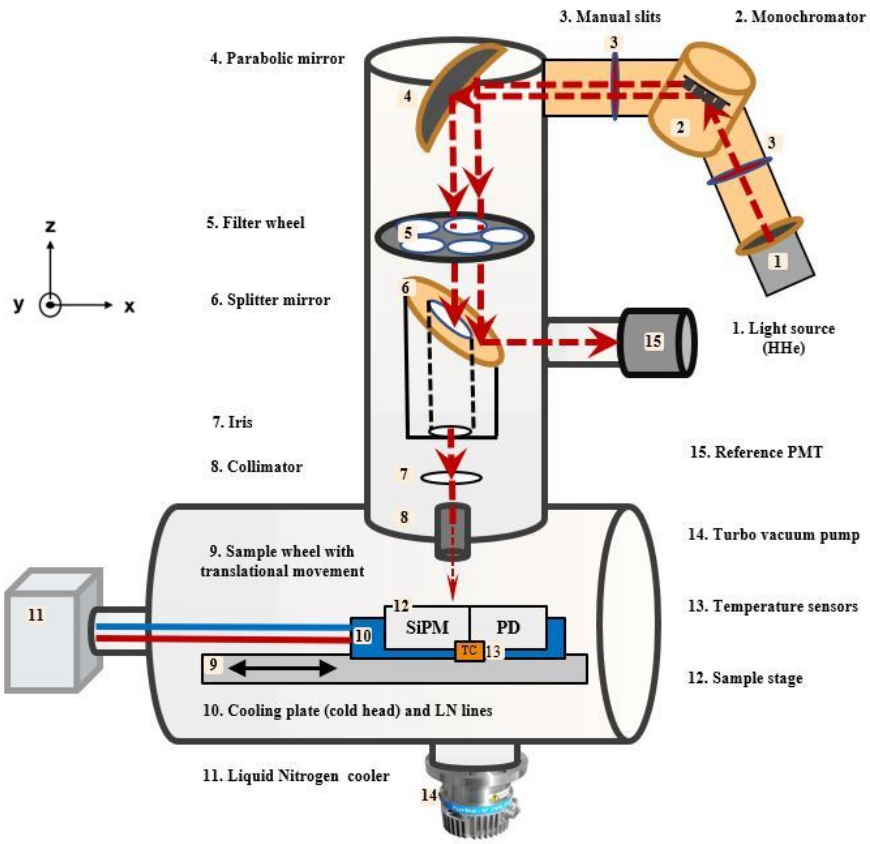

Figure 4.2: Hardware setup used for the characterization of the FBK VUV HD 3 SiPM.

of a vacuum chamber (Fig. 4.3 a)) coupled with a vacuum VM200 Resonance monochromator [78]. The entire chamber is coated with a MH2200 Alion Science vacuum compatible antireflective paint [95] whose reflectivity was certified to be $< 1\%$ in the range 250-2500 nm. Light from a Resonance Lyman-Alpha DC lamp [78] is separated by the monochromator and directed alternatively toward a Photo-Diode (AXUV100G [96]), used to calibrate the absolute light flux, or a SiPM under test (Fig. 4.4). Both devices are placed on a movable arm which allows for remote positioning of the devices under the light beam (Fig. 4.3 b)). Differently from the setup introduced in Chapter 3, the movable arm allows only to perform a beam mapping along the direction marked as x in Fig. 4.2. The AXUV100G

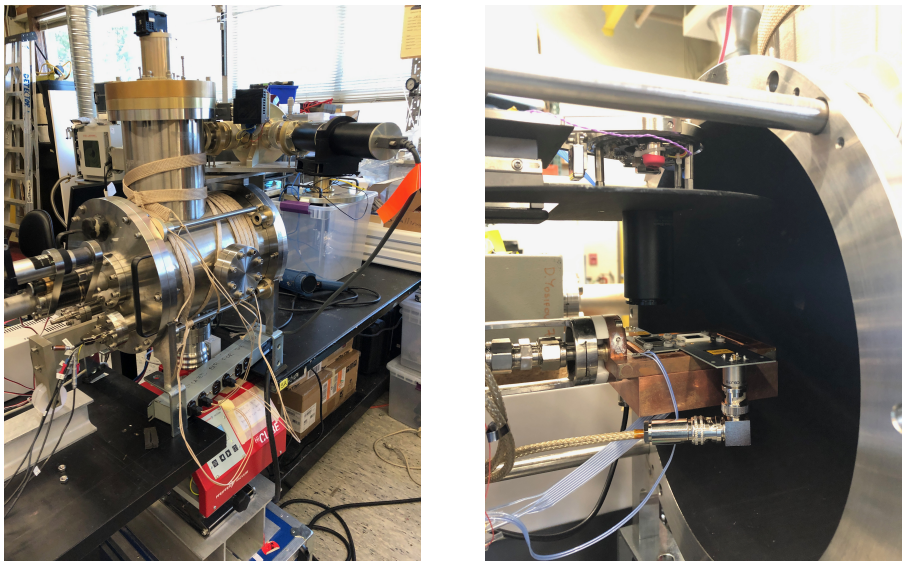

(a) Vacuum Chamber **(b)** Cold Finger

Figure 4.3: Vacuum Emission Reflectivity Absorption (VERA) setup at TRIUMF.

Photo-Diode was calibrated against a NIST calibrated Photo-Diode (XUV-100C) that was placed on the movable arm, in replacement of the SiPM under test, for a calibration measurement (Fig. 4.4). A liquid nitrogen controlled cold finger adjusts the device temperature down to 163 K.

For efficiency measurements the light from the Resonance Lyman-Alpha source

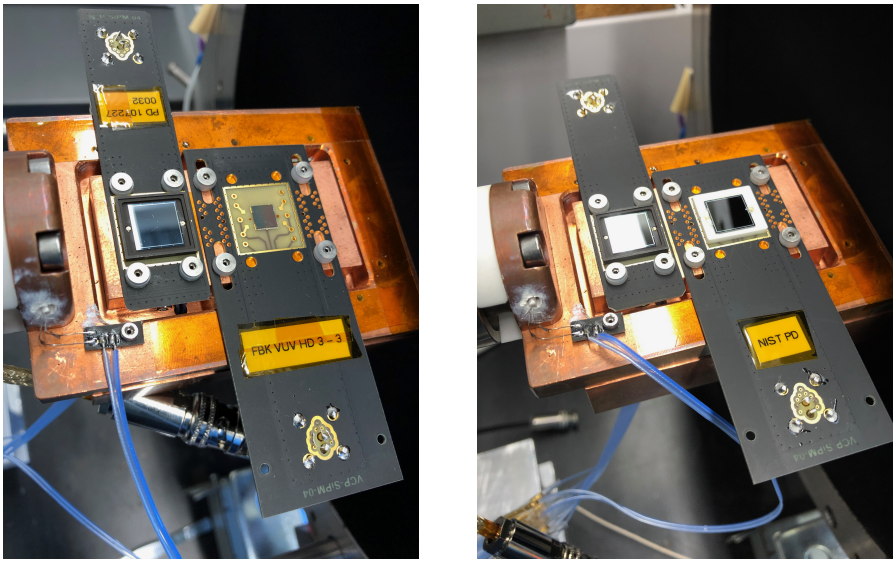

(a) FBK VUV HD 3 efficiency measurement

(b) Photo-Diode Calibration measurement

Figure 4.4: Configuration for efficiency and calibration measurements in the VERA Setup.

passes through a filter wheel, used to suppress multiple orders of the vacuum monochromator and a splitter Gold coated Parabolic Mirror. The mirror allows to simultaneously illuminate the SiPM (or the Photo-Diode) under test and a Reference UV sensitive Hamamatsu Photonics PMT (R8486), used to monitor the light stability. The gold coating was chosen due to its flat reflectivity in a broad wavelength range. Its reflectivity in the VUV wavelength range is however fairly poor and it is partially compensated by the high lamp flux. Before reaching the devices location, light passes also through a motorized IRIS (Uniblitz AI25 [97]) and a 2 mm diameter collimator coupled with a Acktar Hexa-Black collimation tube [98], as shown in Fig. 4.5, with a certified 99.9% absorbance in the wavelength range 200-5000 nm. Particular attention was devoted on the choice of the IRIS blades and on the collimator design to avoid fluorescence from materials located in the light path. The motorized IRIS is used to optimize the light flux for different wavelengths and to change the beam width accordingly to the device under

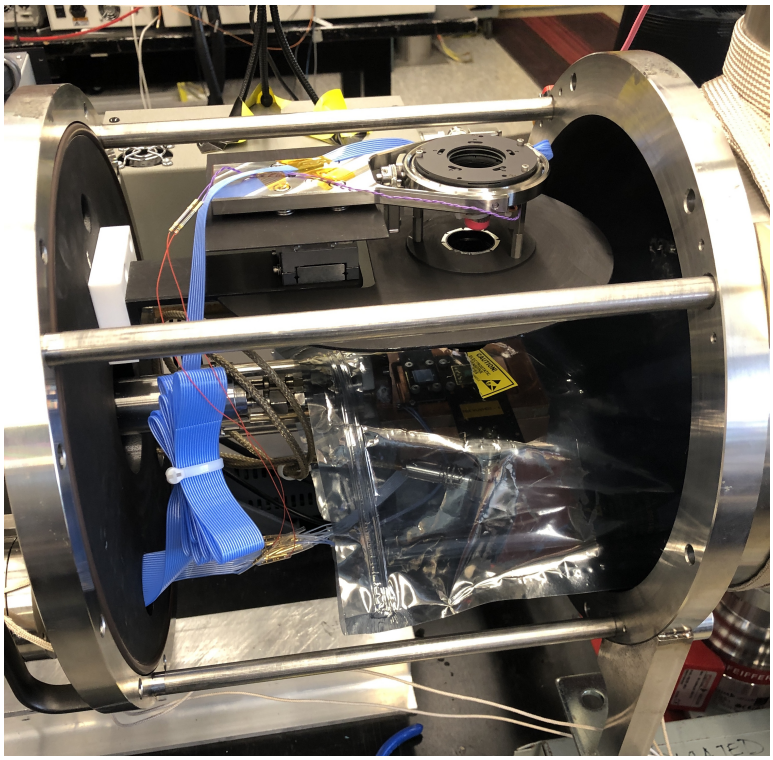

Figure 4.5: Particular of the motorized IRIS assembly inside the vacuum chamber. The IRIS also incorporates a shutter useful to shield the sensor from the lamp light (at the monochromator 0-order) and to record background (dark) measurements.

test. Moreover, it also incorporates a shutter useful to shield the sensor from the lamp light at the monochromator 0-order, and to record background (dark) measurements.

A CAEN DT5730B Digitizer Module [74] and a MIDAS-Labview based control system [75] are used for signal digitalization and for the management of the slow control hardware of the setup. Overall they constitute the VERA Data Acquisition System (DAQ). For pulse counting measurements the SiPM signal is amplified by a two stage amplifier (MAR6-SM+ [76] and OPA695 [99]) while for beam mapping and IV measurements the DC SiPM current is measured with a Keithley 6487 picoammeter [100]. The Photo-Diode current is instead measured

with a Keysight B2985 low noise picoammeter [101]. The reference PMT used to monitor the light stability is biased by a C13654-01 Hamamatsu socket assembly. The output voltage from the Hamamatsu socket is digitized by a Texas Instruments ADS1248 24 bit ADC [102], and it is read by a Nanopi.

4.3 Experimental Results

4.3.1 Lamp Spectrum

Differently from the light filtering scheme introduced in Chapter 3, preliminary studies of the FBK VUV HD 3 PDE, reported in Sec. 4.4, were done using a Resonance Lyman-Alpha light source coupled with a Resonance VM200 vacuum monochromator, as introduced in Sec. 4.2.1. The VM200 allows to precisely select the wavelength and its resolution with a Labview-based control software and a set of input and output slits. In Fig. 4.6 it is reported the lamp spectrum recorded by the Reference PMT as a function of the monochromator slits width. For reference, monochromator input and output slit had always the same width. The main lamp peak is at 160 nm [103, 104]. This peak is used as calibration point for the VM200 monochromator along with its second order at 320 nm. The wavelength resolution generally achievable with a monochromator depends from several characteristics of the monochromator itself: grating, focal length and slit width. Higher groove grating, longer focal length and narrow slit widths allow to achieve better resolution in wavelength. The drawback is the rather poor light intensity since light is more dispersed inside the monochromator. To calibrate the absolute light flux for efficiency measurements (Sec. 4.4) we used a re-calibrated Photo-Diode (AXUV100G). By design Photo-Diodes have no internal gain, therefore the Photo-Diode photon-current measured for rather low photon fluxes ($\sim$ MHz) is fairly small ($\sim$ fA). The VM200 monochromator has a short focal length (200 mm) and it is equipped with a grating with relatively low number of lines per mm: 1200 G/mm[1]. The final wavelength resolution is therefore lower if compared with the one of other commercially available monochromators, but its higher light throughput allows to

[1]Gratings are usually designated by their groove density, the number of grooves per unit length, usually expressed in grooves per millimeter: G/mm.

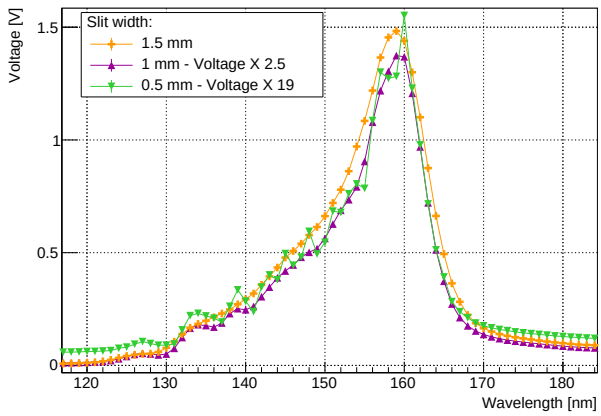

Figure 4.6: Lamp Spectrum of the Lyman-Alpha Resonance light source (Lamp temperature set point: 423 K) recorded by the reference PMT (Bias Voltage: 1050 V) as a function of the VM200 monochromator slit width. Input and output slit had the same width. Smaller slit width results in higher wavelength accuracy (the oscillations in the lamp spectrum can be resolved), but lower photon flux.

achieve a better S/N if used in conjunction with a Photo-Diode. Moreover the LXe scintillation spectrum is fairly broad 174.8 ± 10.2 nm [47], therefore a resolution of few nm is acceptable to characterize devices in this wavelength range.

4.3.2 Beam Mapping Strategy

As introduced in Sec. 4.2.1, the movable arm allows for remote positioning of the devices under the light beam. Differently from the beam mapping scheme reported in Chapter 3, the VERA setup doesn't allow to perform 2D beam mapping of the device under test. This can be a serious issue, since the Photo-Diode and the SiPM under test have different Photosensitive Areas (PA)s of 1×1 cm^2 and 36 mm^2, respectively. The light beam can therefore not be completely contained on the smaller of the two devices (SiPM) bringing to an underestimation of the total measured PDE. To address this issue a CCD camera (ARTCAM-2020UV-USB3) was purchased and it will temporarily substitute the cold finger to map, in the near future, the beam size as function of wavelength and IRIS aperture. This will allow

to correctly measure the light flux, and therefore the PDE, at 175 nm using the technique introduced in Sec. 4.4. For this reason, in Sec. 4.4 we will only present a relative measurement of the SiPM efficiency without proving a normalization for the photon flux at 175 nm.

4.3.3 Collected Data and Trigger Configurations

The SiPMs characteristics were investigated at 163 K. The collected data follow the same scheme presented in Chapter 3 and they can be divided into two types: dark data and DC light lamp data. For both data-sets the DAQ system was set to trigger on individual SiPM pulses with a DAQ threshold above the noise. For each trigger, the DAQ saves the event with a total sample window of 10 μs, split into 2 μs of pre-trigger and 8 μs of post-trigger samples. The data were analyzed at the pulse level with the same ROOT-based [79] waveform analysis toolkit introduced in Chapter 3 with the only difference of the Single Avalanche Response Function (SARF) used to parametrize the FBK VUV HD 3 pulse shape. For the FBK VUV HD 3 SiPM the SARF was represented as the superimposition of two exponentially modified Gaussian distributions with the same variance, but with two exponential time constants as follows [105]

$$\begin{aligned} V(t) = \mathrm{A} \times \Bigg[\frac{1-k}{2\tau_S} \left(\mathrm{Exp}\left[\frac{\sigma^2}{2{\tau_S}^2} - \frac{t-t_0}{\tau_S} \right] \times \mathrm{Erfc}\left[\frac{\sigma}{\sqrt{2}\tau_S} - \frac{t-t_0}{\sqrt{2}\sigma} \right] \right) + \\ + \frac{k}{2\tau_L} \left(\mathrm{Exp}\left[\frac{\sigma^2}{2{\tau_L}^2} - \frac{t-t_0}{\tau_L} \right] \times \mathrm{Erfc}\left[\frac{\sigma}{\sqrt{2}\tau_L} - \frac{t-t_0}{\sqrt{2}\sigma} \right] \right) \Bigg] \end{aligned} \tag{4.1}$$

where: t_0 is the pulse time, σ is the square root of the variance of the Gaussian component, τ_S and τ_L are the two exponential decay constants and $0 \leq k \leq 1$ is the relative contribution of the two fall time components in the SiPM pulse shape. A is the pulse area (proportional to the pulse charge).

4.3.4 Single PE Gain and Breakdown Voltage Extrapolation

Single Photo-electron Equivalent (PE) dark pulses at 163 K from two different FBK devices (FBK VUV HD 3 #1 and FBK VUV HD 3 #2) were used to measure the single PE charge as a function of the SiPM over voltage, as shown in Fig. 4.7.

In the same figure we also reported the single PE charge of the Hamamatsu VUV4 MPPC and FBK VUV HD 1 measured in Chapter 3 and [59], respectively. The single PE (amplified) pulse charge Q was defined as:

$$Q \equiv \left(\frac{\mathrm{IDR}}{2^{14}}\right) \times \left(\frac{\overline{\mathrm{A}}_{1\ \mathrm{PE}} \times 10^{-9}}{\mathrm{R}}\right) \tag{4.2}$$

where: IDR is the Input Dynamic Range of the digitizer (0.5 V), $\overline{\mathrm{A}}_{1\ \mathrm{PE}}$ is the average area (Eq. 4.1) of the fitted digitizer signals for 1 PE pulses (measured in LSB $\times$ ns [74]), and R is the amplifier load resistance (R=50 Ω). Therefore, the single PE (un-amplified) gain ($\mathrm{G}_{1\ \mathrm{PE}}$) can be extracted from Q using the following equation:

$$\mathrm{G}_{1\ \mathrm{PE}} = \frac{Q}{g_{\mathrm{AMP}} \times q_E} \tag{4.3}$$

where g_{AMP} is the gain of the amplifier (measured to be 141 ± 3) and q_E is the electron charge. The amplifier was calibrated using the same scheme already introduced in Chapter 3 (Sec. 3.3.2). The single PE (un-amplified) charge, as a function

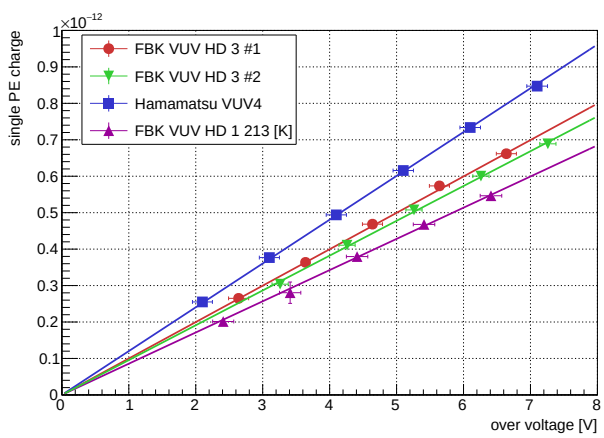

Figure 4.7: Measured single PE charge as a function of the over voltage for several devices tested for the nEXO experiment. The measurements of the FBK VUV HD 3 and Hamamatsu VUV4 were done at 163 K, while the one of the FBK VUV HD 1 was extrapolated from [59] and reported for a temperature of 213 K.

of the bias voltage, was then linearly fitted as $Q_{1\ \mathrm{PE}} = C_D \times (V - V_{BD})$, in order to extract: (i) the SiPM single cell capacitance C_D and (ii) the Breakdown Voltage V_{BD} defined as the bias voltage at which the SiPM single PE gain (or charge) is zero. Table 4.2 summarises the breakdown voltage at 163 K and the capacitance of the devices reported in Fig. 4.7. The capacitance of the FBK VUV HD 3 is compatible with one of the FBK VUV HD 1. The cell structure for the two generations of FBK devices is in fact almost identical (Sec. 4.1). The Hamamatsu VUV4 has a single cell pitch bigger if compared with the one of FBK devices (50μm vs 35μm, respectively) resulting in a larger SPAD capacitance.

Device	Capacitance [fF]	Breakdown [V]
Hamamatsu VUV4	116 ± 6	44.8 ± 0.11
FBK VUV HD 1 [213 K]	86 ± 5	30.6 ± 0.14
FBK VUV HD 3 #1	100 ± 5	27.4 ± 0.15
FBK VUV HD 3 #2	96 ± 5	27.7 ± 0.17

Table 4.2: Summary of the capacitance and breakdown voltage for several photon-sensors tested for nEXO. The FBK VUV HD 3 and Hamamatsu VUV4 measurements were done at 163 K, while the one of the FBK VUV HD 1 was derived from [59] and reported for a temperature of 213 K.

4.3.5 Noise Analysis

In this section we report the results of the dark characterization at 163 K for the two FBK VUV HD 3 devices (FBK VUV HD 3 #1 and FBK VUV HD 3 #2) already introduced in the previous section. In particular, the FBK VUV HD 3 characteristics were compared against: (i) the nEXO requirements, (ii) the Hamamatsu VUV4 MPCC and FBK VUV HD 1 SiPM, reported in Chapter 3 and in [1], respectively. More precisely, the FBK VUV HD 3 Dark Noise rate (DN), as a function of the over voltage, is presented in Sec. 4.3.5.2. The FBK VUV HD 3 number of Correlated Avalanches (CAs) and Correlated Delayed Avalanches (CDAs) per primary pulse in 1 µs after the trigger pulse is reported in Sec. 4.3.5.1 and

Sec. 4.3.5.2, respectively[2]. Direct CrossTalk (DiCT) is discussed in Sec. 4.3.5.3. It is worth recalling that the SiPM noise was studied using dark data, taken with the SiPM shielded from any light source (Sec. 4.3.3). All the measurements reported in the next sections were performed at 163 K.

4.3.5.1 Number of Correlated Avalanches per Pulse

In order to reach the nEXO design performance, the relative fluctuation of the mean number of CAs, within a time window of 1 μs after the primary pulse, needs to be < 0.4. The average number of CAs per primary pulse is measured by directly constructing a histogram of the baseline subtracted integral of collected dark waveform in the range $[0-3]$ μs (the trigger pulse is at 2 μs) and normalizing it to the average charge of 1 PE pulses, as discussed in Chapter 3. The number of correlated avalanches is then computed as

$$\langle \Lambda \rangle = \frac{1}{N} \sum_{i=1}^{N} \frac{\mathrm{A}_{\text{T-w}i}}{\overline{\mathrm{A}}_{1\ \mathrm{PE}}} - 1 \tag{4.4}$$

where $\mathrm{A}_{\text{T-w}i}$ is the Total charge of the waveform-i (baseline subtracted) integrated up to 1 μs after the trigger pulse, $\overline{\mathrm{A}}_{1\ \mathrm{PE}}$ is the average charge of 1 PE pulses and N is the number of waveform analyzed. The $\langle \Lambda \rangle$ number, in unit of PE, as a function of the over voltage, is reported in Fig. 4.8. For comparison, in the same figure we also reported the number of CAs for the other two SiPMs tested for nEXO. The FBK VUV HD 3 has a significantly smaller number of CAs if compared with its previous generation (FBK VUV HD 1). As it will be shown in Sec. 4.3.5.2 and Sec. 4.3.5.3, the significant improvement of the new generation of FBK devices is mainly due to the reduction of after pulse thanks to the new triple doping technology developed by FBK, rather than the reduction of the optical CrossTalk, that instead is essentially the same of the previous generation. Overall the correlated avalanche noise characteristics of the FBK VUV HD 3 are comparable with the one of the Hamamatsu VUV4 MPPC. Fig. 4.9 reports instead the Root Mean Square Error (RMS) of the number of CAs per primary pulse within a time window of

[2]We refer the reader to Chapter 2 for a detailed explanation of the different sources of noise in SiPMs.

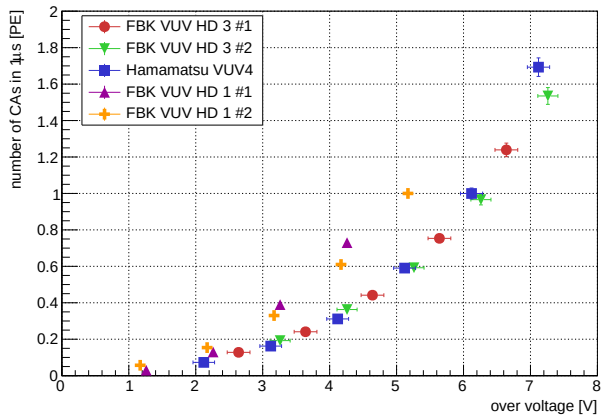

Figure 4.8: Number of Correlated Avalanches (CAs) per primary pulse measured at 163 K within a time window of 1 μs after the trigger pulse as a function of the applied over voltage for several photon-sensors tested for nEXO.

1 µs after the trigger pulse as a function of the applied over voltage (i.e. σ_Λ). Differently from Fig. 4.8, the FBK VUV HD 1 data could not be included in Fig. 4.9 since in [1], it was only reported the mean number of correlated avalanches in 1 µs, without any additional information of its RMS error. As shown in Fig. 4.9 and in Fig. 4.8, the RMS error and the mean number of correlated avalanches of the FBK VUV HD 3 and Hamamatsu VUV4 MPPC are compatible: the two SiPMs have therefore similar noise performances. Additionally both devices show a high RMS error that results in a significant fluctuation in the number of correlated avalanches between different events. Fig. 4.10 reports the relative fluctuation of the mean number of CAs in 1 μs at 163 K, useful for nEXO operation, for the three devices of Fig. 4.9. The relative fluctuation was defined as introduced in Eq. 3.4 and here reported for clarity

$$\text{Ratio} \equiv \frac{\sigma_\Lambda}{1+\langle\Lambda\rangle}$$

In order to meet the nEXO requirements (Sec. 2.4.2), the FBK VUV HD 3 can be operated at T=163 K up to about 3.2 V of over voltage while keeping the relative

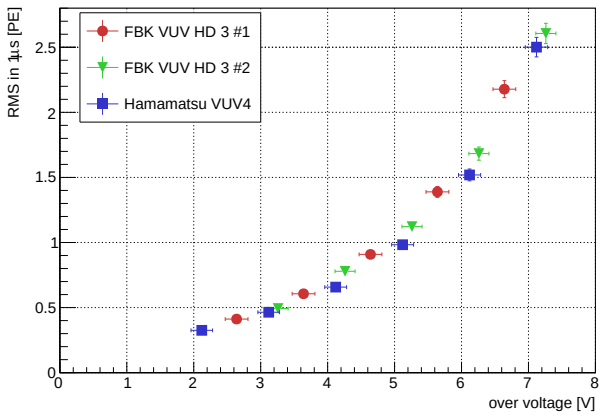

Figure 4.9: Root Mean Square Error (RMS) of the number of Correlated Avalanches (CAs) per primary pulse measured at 163 K within a time window of 1 µs after the trigger pulse as a function of the applied over voltage for several photon-sensors tested for nEXO.

fluctuation of the mean number of CAs in 1 μs smaller than 0.4. The triple doping technology allows therefore to increase of 1 V the operational over voltage of these devices. This automatically means, accordingly to Fig. 4.7, a higher single PE charge and gain with better S/N ratio.

4.3.5.2 Dark Noise Rate and Number of Correlated Delayed Avalanches per Pulse

Dark Noise (DN) and Correlated Delayed Avalanches (CDA)s events can be distinguished by studying the time distribution of events relative to the primary pulse using the method introduced in Sec. 3.3.4.2 of Chapter 3. An example of the FBK VUV HD 3 charge distribution (for the FBK VUV HD 3 #1) as a function of the time difference with respect to the primary pulse is reported in Fig. 4.11 for an over voltage of 5.64 ± 0.17 V, at 163 K. If compared with the charge distribution of the Hamamatsu VUV4 MPPC (Fig. 3.6) measured at the same temperature and roughly over voltage, the FBK VUV HD 3 has a significantly higher amount of multiple PE events due to direct CrossTalk between pixels. A study of the FBK VUV HD 3 Direct CrossTalk (DiCT) contribution is reported in Sec. 4.3.5.3.

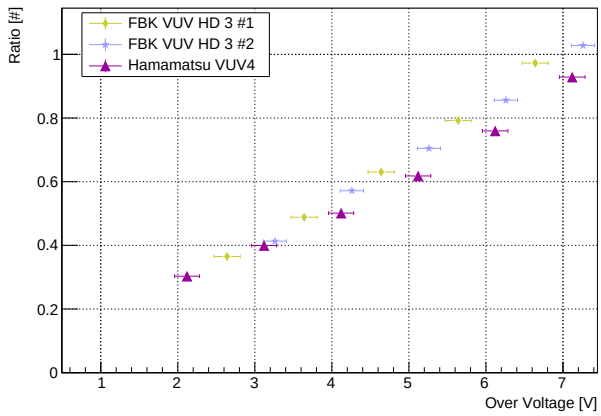

Figure 4.10: Relative fluctuation of the number of CAs in 1 μs measured at 163 K and derived with Eq. 3.4 from the data of Fig. 4.8 and Fig. 4.9.

Fig. 4.11 can then be used to extrapolate the pulse rate R(t) as a function of the time difference with respect to the primary pulse using Eq. 3.5, as reported in Sec. 3.3.4.2. The result is reported in Fig. 4.12. In the same figure we also reported the observed pulse rate for the highest over voltage dataset measured at 163 K for the Hamamatsu VUV4 MPPC. Fig. 4.12 clearly shows as the Hamamatsu device has a significantly higher amount of correlated avalanches if compared with the FBK VUV HD 3, especially at short times after the trigger pulse ($\leq$ 100 ns) where the time distribution is dominated by after pulse events. The high Hamamatsu VUV4 afterpulse rate was already reported in Sec. 3.3.3 while analysing its prompt pulse charge distribution. In that case we noticed shoulder-like events in the Hamamatsu VUV4 charge distribution that we attributed to fast correlated avalanches which do not get resolved from their parent primary pulse by the DAQ ($\leq$ 4 ns).

The afterpulse rate of the FBK and Hamamatsu devices can be better compared analysing the total Number of Correlated Delayed Avalanches (CDA) in 1 μs with respect to the trigger pulse, as a function of the over voltage, using Eq. 3.6 of Sec. 3.3.4.2, as shown in Fig. 4.13. The number of CDA of the FBK VUV HD 3 is greatly reduced not only if compared with its previous generation, but also if compared with the Hamamatsu VUV4 MPPC resulting therefore in a smaller num-

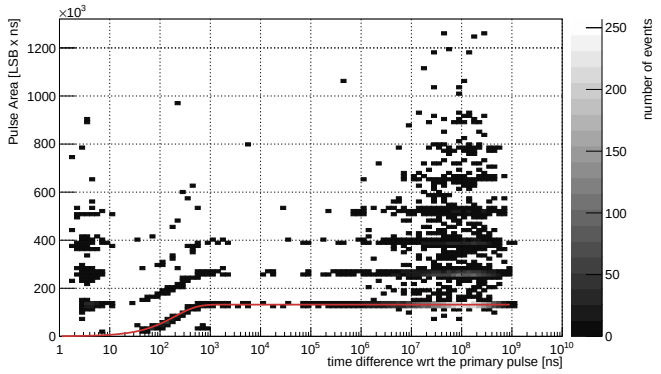

Figure 4.11: FBK VUV HD 3 #1 charge distribution of first pulses following single PE trigger pulses as a function of the time difference with respect to (wrt) their primary pulse for T=163 K and for an over voltage of 5.64 ± 0.17 V. The grey scale represents the number of events in each bin on a logarithmic scale. The solid red line shows a fit of the afterpulsing events and is used to measure the recovery time of one cell, equal to 195 ± 10 ns.

ber of after pulse events in the same acquisition window (1 μs after the trigger). As already introduced in Sec. 4.3.5.1, this is a consequence of the triple doping technology developed by FBK for the Darkside-20k experiment and used in this new generation of FBK devices. From Fig. 4.12 it is possible to extrapolate the Dark Noise Rate at 163 K, as a function of the over voltage, performing a weighted mean of the asymptotic rates at long times, as reported in Fig. 4.14. For a device temperature of 163 K all the SiPMs tested (including the FBK VUV HD 3) meet the nEXO requirement of $<$50 Hz/mm^2 (Sec. 2.4.2) with values comfortably lower than the required one.

4.3.5.3 Number of Additional Prompt Avalanches

Direct CrossTalk (DiCT) can be investigated with the same technique used in Sec. 3.3.4.3 by studying the charge distribution of prompt pulses obtained from dark data. More precisely, using Eq. 3.7 it is possible to measure the number of Additional Prompt Avalanches (APA) as a function of the over voltage at 163 K, as shown in Fig. 4.15. The number of APA of the FBK VUV HD 3 is significantly

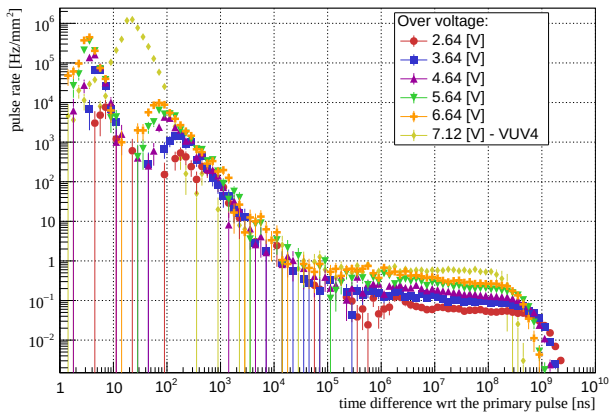

Figure 4.12: Observed dark pulse rate R(t) of the FBK VUV HD 3 #1 SiPM as a function of the time difference with respect to (wrt) the primary pulse for a temperature of 163 K and for different over voltages. For comparison, in the same figure we also reported the pulse rate for the highest over voltage point measured in Chapter 3 for the Hamamatsu VUV4 MPPC (7.12 ± 0.16 V).

higher if compared with the one of the Hamamatsu VUV4 MPPC, as already noticed in Sec. 4.3.5.2. Additionally, the new generation of FBK devices has almost identical performances of its previous generation (FBK VUV HD 1). From this we can conclude as the reduced number of correlated avalanches (Sec. 4.3.5.1) is mainly due to the reduced after pulse (Sec. 4.3.5.2) rather than the reduced Direct optical CrossTalk, as anticipated in Sec. 4.3.5.1.

4.4 A new DC technique to measure the SiPM Photon Detection Efficiency

To meet the nEXO requirements, the SiPM PDE must be $\geq 15\%$ for liquid xenon scintillation wavelengths (174.8 ± 10.2 nm [47]), as shown in Sec. 2.4.2. In Chapter 3 the Hamamatsu VUV4 PDE was measured using a filtered pulsed xenon flash lamp and a technique that was based on Poisson statistics. More precisely, the average number of photons detected by the SiPM was firstly measured by counting the number of lamp flashes in which no photons were detected (corrected for the

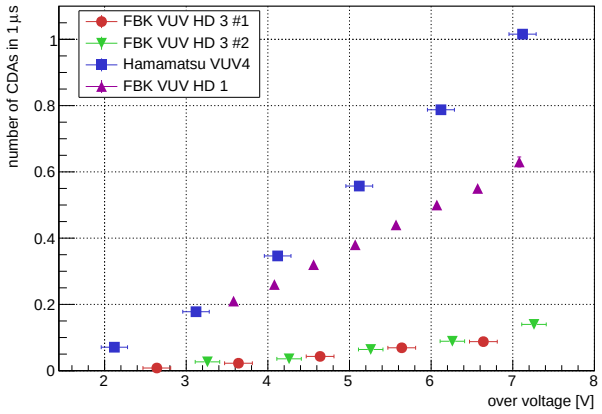

Figure 4.13: Number of Correlated Delayed Avalanches (CDAs) per primary pulse measured at 163 K within a time window of 1 μs after the trigger pulse as a function of the applied over voltage for several photon-sensor tested for nEXO.

SiPM dark noise rate), and then normalized for the average number of photons detected by a calibrated Hamamatsu PMT. This technique cannot be applied with DC lamps (like the Lyman-Alpha Resonance light source), since the probability to have no photons in the acquisition window is negligible if compared with the probability to have one or multi-photon events in the same acquisition window. Moreover, the high photon flux that is associated with DC light sources may produce delayed correlated avalanches that trigger the DAQ artificially increasing therefore the final SiPM PDE. Different techniques are available in literature to measure the SiPM PDE with DC lamps. These techniques relay on measuring the SiPM current and then correct it for the correlated avalanche noise contribution as shown, for example, in [94]. These corrections, however, are often model dependent, since it is complicated to resolve analytically higher orders of correlated avalanche noise (e.g. afterpulse of DiCT and/or afterpulse of DeCT). In this section we introduce a different technique that is free from correlated avalanche noise and that can be used to measure the SiPM efficiency with DC light sources. The main characteristic is to estimate the SiPM photon induced avalanche rate at the SiPM location using the time distribution between pulses, in analogy with what was done in Sec. 3.3.4.2

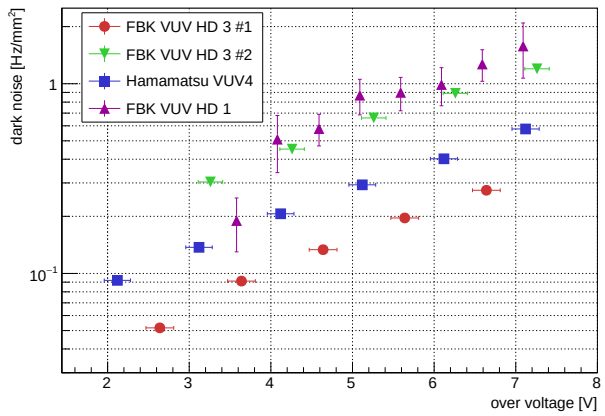

Figure 4.14: Dark Noise rate measured at 163 K and normalized by the SiPM photon sensitive area as a function of the applied over voltage for several photon-sensor tested for nEXO.

and Sec. 4.3.5.2 to measure the dark noise rate of the Hamamatsu VUV4 MPPC and FBK VUV HD 3 SiPM, respectively. More precisely, since photon induced avalanches are uncorrelated events (like dark noise events), it is possible to distinguish them from dark noise and correlated delayed avalanches by studying the time distribution of all the events relative to the primary pulse. The total observed pulse rate $R(t)$ can then be computed as a function of the time difference with respect to the primary pulse using Eq. 3.5 including an additional contribution due to photon induced avalanches as follows:

$$R(t) = R_{DN}(t) + R_0(t) + R_{CDA}(t) \tag{4.5}$$

where: $R_0(t)$ is the contribution due to the photon induced avalanches detected by the SiPM; $R_{DN}(t)$ is the SiPM dark noise measured in Sec. 4.3.5.2; and $R_{CDA}(t)$ is the correlated delayed avalanche rate. The FBK VUV HD 3 pulse rate $R(t)$, as a function of the time difference with respect to the primary pulse, for different over voltages under 175 nm illumination is reported in Fig. 4.16. It is clear comparing Fig. 4.16 with Fig. 4.12 as the pulse rate at 163 K is significantly higher under illumination due to the photon induced contribution to the total pulse rate. The

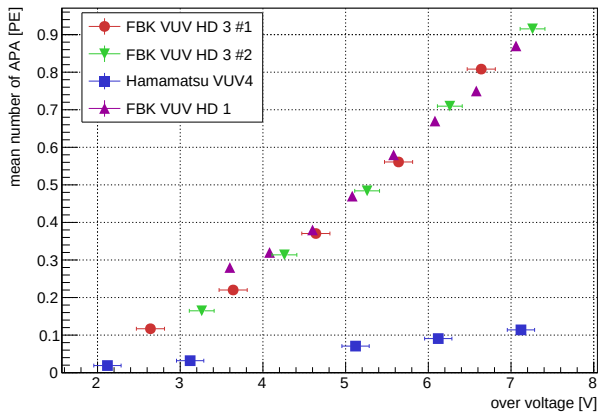

Figure 4.15: Number of Additional Prompt Avalanches (APA)s measured at 163 K as a function of the over voltage for several photon-sensor tested for nEXO.

uncorrelated pulse rate ($R_{DN}(t) + R_0(t)$) can then be measured, as a function of the over voltage, from Fig. 4.16 performing a weighted mean of the asymptotic rate at long times[3]. Subtracting from this last quantity the dark noise rate measured in Sec. 4.3.5.2 with the same technique (but without illumination), gives the photon induced avalanches rate ($R_0(t)$) detected by the SiPM, as shown in Fig. 4.17. The SiPM PDE can then be obtained dividing $R_0(t)$ by the photon flux Φ_0 measured with a calibrated detector at the SiPM location as:

$$\mathrm{PDE} = \frac{R_0}{\Phi_0} \tag{4.6}$$

Fig. 3.18 in Chapter 3 and Fig. 4.17 differ only for the missing normalization Φ_0 for the FBK VUV HD 3 data (Sec. 4.3.2) that is independent from the SiPM over voltage. The photon induced pulse rate of Fig. 4.17 and the SiPM PDE of Fig. 3.18 have the same trend as a function of the applied over voltage: both curves saturate at high over voltages due to the saturation of the electron avalanche triggering probability, as it will be discussed in more details in Chapter 5. We stress as the technique introduced in this section is free from correlated avalanche noise, since

[3]Each point in the mean was weighted with its error derived as reported in [85].

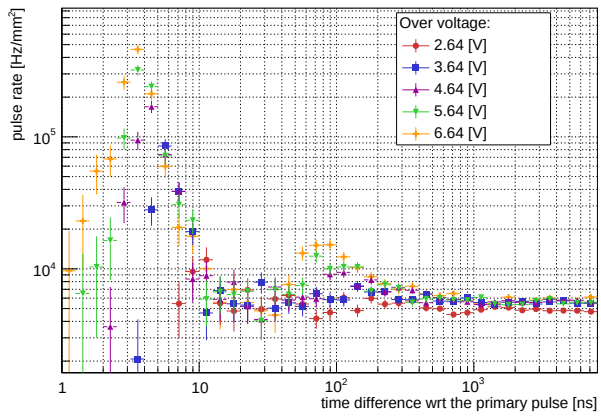

Figure 4.16: Observed pulse rate $\mathrm{R}(t)$ of the FBK VUV HD 3 #1 SiPM as a function of the time difference with respect to (wrt) the primary pulse for a temperature of 163 K under 175 nm light illumination.

their contribution to the total pulse rate can be discriminated while constructing the rate plot, as the one shown for example in Fig. 4.16.

4.4.1 Calibration of the photon flux with a NIST Photo-Diode as reference

As introduced in Sec. 4.3.2, the PDE of the FBK VUV HD 3 could not be finalized due to the ongoing study of the beam shape that will be mapped in a close future with a linear CCD. For this reason, in the previous section we didn't provide a normalization (Φ_0) for the data of Fig. 4.17. As introduced in Sec. 4.2.1, for the measurement of the FBK VUV HD 3 efficiency we plan to use a re-calibrated photo-diode in order to calibrate the absolute light flux Φ_0, as follows:

$$\Phi_0 = \frac{(I - I_{\mathrm{DN}})\lambda}{R\mathrm{hc}} \tag{4.7}$$

where: I and I_{DN} are the Photo-Diode currents with and without illumination, respectively; R is the Photo-Diode responsivity at the wavelength λ; h is the Planck constant and c is the speed of light. This is a radical difference if compared with what was done in Chapter 3 where we used a calibrated PMT to measure the abso-

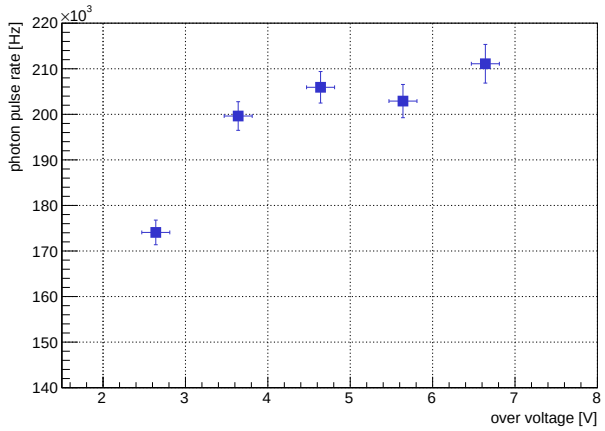

Figure 4.17: Observed photon induced pulse rate $R_0(t)$ extrapolated from Fig. 4.16 for the FBK VUV HD 3 #1 SiPM as a function of the over voltage, for a temperature of 163 K, under 175 nm light illumination.

lute light flux at the SiPM location. The choice to abandon PMTs is in fact driven by the low information available on their collection efficiency. Additionally, NIST Photo-Diodes come with a small uncertainty on their responsivity (Fig. 4.18) and this will allow to reduce significantly the systematic error on the final measured PDE. The drawback to use Photo-Diodes is the small current ($\sim$ fA) measured for rather low photon fluxes ($\sim$ MHz). Eq. 4.5, in fact, assumes the capability to keep the SiPM in pulse counting mode: it therefore assumes that the fitting procedure introduced in Sec. 4.3.3 can be successfully applied on the SiPM pulses recorded by the DAQ under illumination. In order to do so, it is necessary to adjust the light flux (done with the motorized IRIS introduced in Sec. 4.2.1) to have, at the same time, the SiPM in pulse-counting mode and the S/N of the Photo-Diode high enough to measure the 175 nm light of the DC lamp. For this reason, to minimize the noise induced on the Photo-Diode by other sources, not only we used shielded low noise triax cable (Keithley 7078-TRX-1), but also we measured the Photo-Diode current with a Keysight B2985 low noise picoammeter that is one of the commercially available instruments with the lowest RMS current noise (RMS noise with open input of $\sim$ 140 aA). Without implementing these noise suppression strategies, Photo-Diode measurements would be in fact dominated by the noise induced by:

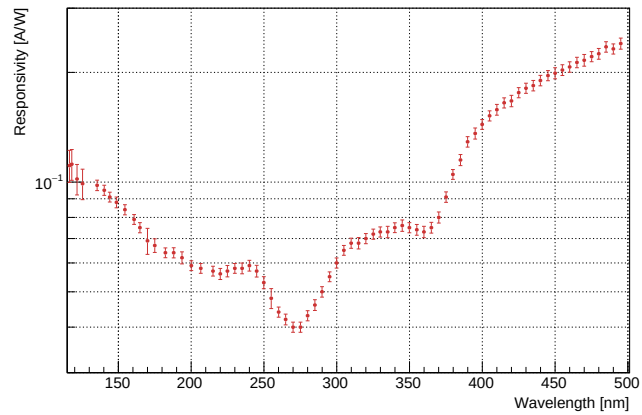

Figure 4.18: Responsivity of the NIST calibrated Photo-Diode as a function of the wavelength.

the picoammeter itself, the cabling and other instruments rather than the photon current measured by the Photo-Diode.

4.4.2 Temperature dependence of the Photo-Diode current

In Sec. 4.4.1 we provided a technique to obtain a measurement of the photon flux at the SiPM location using a calibrated NIST diode. In this section we will study the temperature dependence of the Photo-Diode current under identical photon fluxes. Fig. 4.19 and Table 4.3 show typical currents measured by the Photo-Diode for different wavelengths with and without illumination, as a function of the temperature. The Photo-Diode photon current, reported in Fig. 4.19, was computed as

$$\mathrm{I}^{0F}_{\mathrm{Diode-T}} = \mathrm{I}^{0}_{\mathrm{Diode-T}} \times \frac{\mathrm{V}^{0}_{\mathrm{PMT-T}}}{\mathrm{V}^{0}_{\mathrm{PMT\text{-}300}}} \tag{4.8}$$

where: $\mathrm{I}^{0}_{\mathrm{Diode-T}}$ and $\mathrm{I}^{0F}_{\mathrm{Diode-T}}$ refer to the Photo-Diode current, corrected for the dark current, measured at the temperature T before and after re-scaling. The quantity $\mathrm{I}^{0}_{\mathrm{Diode\text{-}T}}$, for example, was computed as

$$\mathrm{I}^{0}_{\mathrm{Diode\text{-}T}} = \mathrm{I}_{\mathrm{Diode\text{-}T}} - \mathrm{I}^{D}_{\mathrm{Diode\text{-}T}} \tag{4.9}$$

where: $I^{D}_{\text{Diode-T}}$ is the Photo-Diode dark current measured at the temperature T, reported in Table 4.3, and $I_{\text{Diode-T}}$ is the current measured by the Photo-Diode under illumination at the same temperature. $V^{0}_{\text{PMT}-\text{T}}$ and $V^{0}_{\text{PMT-300}}$ refer instead to the

Temperature [K]	Current [A]
300	$(36.5 \pm 7.2) \times 10^{-15}$
223	$(3.5 \pm 3.7) \times 10^{-15}$
163	$(3.0 \pm 3.3) \times 10^{-15}$

Table 4.3: Average dark current of the Photo-Diode as a function of the temperature.

voltage measured by the reference PMT when the Photo-Diode had a temperature of T and 300 K, respectively. $V^{0}_{\text{PMT}-\text{T}}$ is reported in Fig. 4.20. The rationale for the

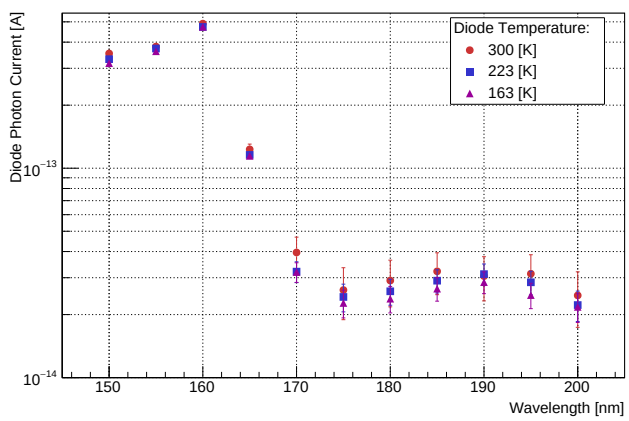

Figure 4.19: Photo-Diode photon current measured, as a function of the wavelength, for several Photo-Diode temperatures.

ratio in Eq. 4.8 is the correction of the Photo-Diode currents for light fluctuations independent from the Photo-Diode itself, but due instead to the DC lamp. The reference PMT was in fact used to monitor the light flux between different Photo-Diode measurements, as introduced in Sec. 4.2.1. The studies of the temperature dependence of the Photo-Diode current, reported in Fig. 4.19, are crucial to obtain a reliable PDE measurement at cryogenic temperatures. Vacuum systems can in

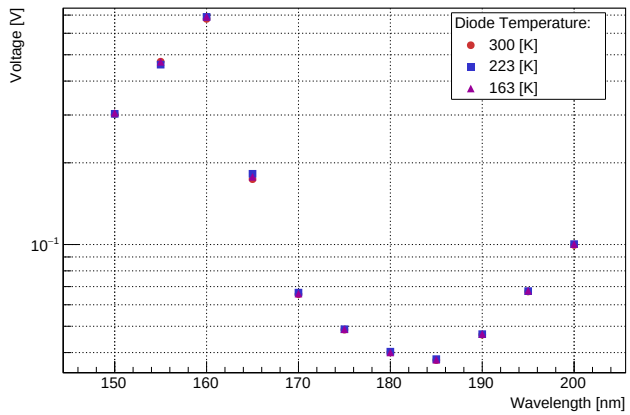

Figure 4.20: Voltage recorded with the reference PMT during the Photo-Diode measurements reported in Fig. 4.19.

fact suffer from residual moisture condensation. According to [106], the AXUV Photo-Diode series used for this measurement (AXUV100G) should have a weak temperature dependence quantifiable in a change of its responsivity of 0.03% per degree Kelvin[4]. The authors however acknowledge in their publication possible residual contamination on the diode surface due to some anomalous drops in the diode responsivity at cryogenic temperatures. More generally, any drop in the diode responsivity, in particular in the 150-170 nm range, suggests the possibility of moisture condensation since water strongly absorbs in this wavelength range, as shown in [107]. In order to prevent the possibility of moisture condensation during PDE measurements, a number of procedural techniques were implemented. First of all, in the VERA setup we only used ultra high vacuum materials. The chamber was evacuated by a turbomolecular pump and the baseline pressure before each measurement was typically around $\sim 1 \times 10^{-7}$mBar. Additionally, after any exposure to air the chamber was heated for 48 h at temperatures > 150 C. This was done thanks to heating strips wrapped around the vacuum chamber with the system under vacuum (Fig. 4.3 a)). This allowed to force the desorption of water

[4]Moisture condensation can only happen on the Photo-Diode or on the SiPM that are cooled at 163 K, not on the reference PMT that instead is located on a separate flange of the VERA setup and it is not cooled.

molecules from walls and other assemblies in the vacuum chamber and to therefore reduce the content of contaminants in the setup. Finally, a Residual Gas Analyzer (RGA) (SRS 100) was also installed on one of the flanges and the amount of water measured by the instrument after 48 h of baking was always below its sensitivity. All these precautions allowed to obtain the Photo-Diode currents measured in Fig. 4.19 that show a temperature dependence smaller of the ones reported in [106] with currents measured, at different temperatures, always compatible within the error at each wavelength.

4.5 Estimation of the nEXO energy resolution

The nEXO experiment is designed to optimize the characteristics of the light and charge channels to provide the best possible energy resolution for a LXe TPC with a final design goal of 1% energy resolution (σ/Q) for the $0\nu\beta\beta$ decay of ^{136}Xe (Q-value at 2458.07 ± 0.31 keV [9]). In Chapter 2 we shown as the first generation of FBK devices (FBK VUV HD 1) satisfies the requirement on the overall nEXO energy resolution, at an over voltage roughly between 2 and 3 V. In this section we will predict the nEXO energy resolution, as a function of the SiPM over voltage, using the characteristics of the two SiPMs fully characterised in this work: the Hamamatsu VUV4 MPPC and the FBK VUV HD 3 SiPM. The starting point is the model of the nEXO energy resolution with Eq. 2.53, derived in Sec. 2.4.3, and here reported for clarity

$$\frac{\sigma_n}{\langle n \rangle} = \frac{\sqrt{\left(\frac{(1-\varepsilon_p)n_p}{\varepsilon_p} + \frac{\varepsilon_p n_p \sigma_\Lambda^2}{(\varepsilon_p(1+\langle\Lambda\rangle))^2}\right) + \left(\frac{(1-\varepsilon_q)n_q}{\varepsilon_q} + \frac{\sigma_{q,noise}^2}{\varepsilon_q^2}\right)}}{\langle n \rangle}$$

Table 4.4 summarises the meaning and the values of the parameters used in this equation.

As already anticipated in Sec. 2.4.3, Eq. 2.53 differs from the one used in [1]. The main difference is the estimation of the correlated avalanche noise contribution to the overall energy resolution. In [1] CAs are in fact treated as Poisson processes.

The overall energy resolution therefore was proportional to

$$\frac{\sqrt{\langle\Lambda\rangle}}{1+\langle\Lambda\rangle} \tag{4.10}$$

This approximation is justified at low over voltages (when $\langle\Lambda\rangle < 1$), but tends to artificially improve the energy resolution at high over voltages. In the model derived in Sec. 2.4.3 the resolution is instead proportional to

$$\frac{\sigma_\Lambda}{1+\langle\Lambda\rangle} \tag{4.11}$$

therefore it worsens at high over voltages since σ_Λ increases faster than $\langle\Lambda\rangle$. Fig. 4.21 compares the two estimators, as a function of the over voltage, for the two SiPMs tested in this work. The two estimators are comparable at low over voltages: < 4 V.

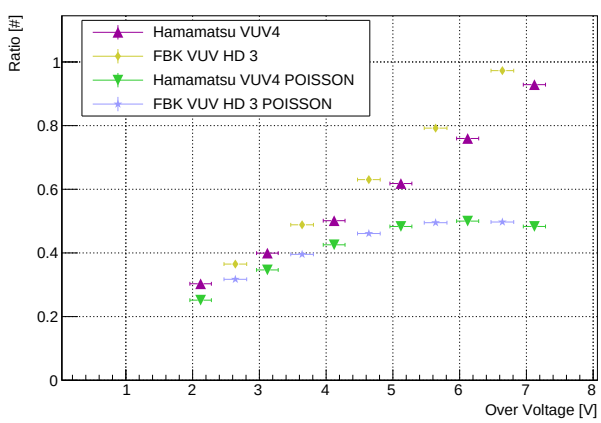

Figure 4.21: Comparison of two estimators used to account for the CA noise contribution in the derivation of the nEXO energy resolution for the two SiPMs tested in this work. The estimator labelled as POISSON was derived from [1] and was defined, assuming Poisson statistics as $\frac{\sqrt{\langle\Lambda\rangle}}{1+\langle\Lambda\rangle}$. The other one, introduced in this work, is defined as $\frac{\sigma_\Lambda}{1+\langle\Lambda\rangle}$.

At higher over voltages instead the new estimator accounts for the increased fluctuation in the number of correlated avalanches while the previous one was artificially decreasing. Fig 4.22 reports the predicted nEXO energy resolution, using the new

Symbol	Meaning	Value
n_p [γ]	Number of photons	90946
CE [#]	Photon Collection Eff.	$20-33\%$
PDE [#]	Photon Detection Eff.	Fig. 3.18
$\langle\Lambda\rangle$ [PE]	Mean number of CA	Fig. 4.8
σ_Λ [PE]	Fluctuation in number of CA	Fig. 4.9
n_q [e$^-$]	Number of electrons	122900
ε_q [#]	Charge Collection Eff.	97%
$\sigma_{q,noise}$ [e$^-$]	Noise in the charge ch.	1100
n [#]	Total number of quanta	2.14×10^5

Table 4.4: Summary of the parameters of Eq. 2.53. n_p and n_q represent the number of photons and electrons produced by the $0\nu\beta\beta$ decay of ^{136}Xe (Q-value at 2458.07 ± 0.31 keV). CE and PDE represent the detector photon Collection Efficiency (CE) and the SiPM Photon Detection Efficiency (PDE). Their product defines the overall light detection efficiency of the experiment i.e. $\varepsilon_p = \text{CE}\times\text{PDE}$. The SiPMs Photon Detection Efficiency, Correlated Avalanche (CA) noise ($\langle\Lambda\rangle$) and fluctuation in the number of CA (σ_Λ) are reported in Fig. 3.18, Fig. 4.8 and Fig. 4.9 for the two devices tested in this work: Hamamatsu VUV4 and FBK VUV HD 3. ε_q and $\sigma^2_{q,noise}$ represent the charge collection efficiency and the noise in the charge channel. n is the total number of quanta of either type (light and charge) produced by the original energy deposition. We refer the reader to Sec. 2.4.3 for a detailed explanation of the values reported in this table.

estimator for the SiPM CA noise, including the contribution of the light and charge channels using the data of Table 4.4 and a 20% light Collection Efficiency (CE) for the experiment. This last number is a conservative value and it was derived from light transport simulation of the nEXO detector using conservative parameters for the reflectivity of the detector components, as shown in Fig. 2.18 of Chapter 2. The three main parameters that drive the energy resolution of Fig. 4.22 in the light channel are: the SiPMs Photon Detection Efficiency (PDE), the SiPM mean number of Correlated Avalanche (CA) per pulse ($\langle\Lambda\rangle$) and its fluctuation (σ_Λ). The last two quantities, used for the construction of Fig 4.22, are reported in Fig. 4.8 and Fig. 4.9 for the two SiPMs tested. The efficiency of the Hamamatsu VUV4 MPPC

is reported in Fig. 3.18. The efficiency of the FBK VUV HD 3 SiPM could not be finalised in this work due to an ongoing study of the beam size in the VERA setup (Sec. 4.4). In Fig 4.22 we therefore assumed that the new generation of FBK devices had the same efficiency of its previous generation: FBK VUV HD 1, reported in Fig. 3.18 of Chapter 3. Conservatively we also assumed that the efficiency of the FBK VUV HD 3 was equal to the lower of the three measurements reported in Fig. 3.18. The error bars account for the systematic errors in the measurements of the SiPMs PDE, as shown in Fig. 3.18. The most dominant feature

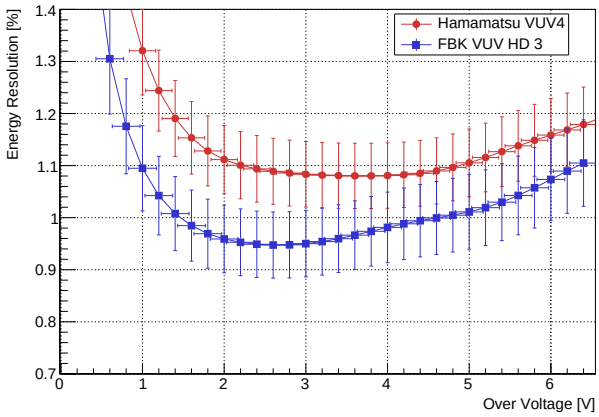

Figure 4.22: nEXO predicted energy resolution as a function of the SiPM over voltage for the two SiPMs tested in this work. Both curves include the contribution of the charge channel and use the values reported in Table 4.4. The overall detector collection efficiency was set to 20%.

of the two curves is the existence of a minimum, as already noticed in Sec. 2.4.2 while analysing the energy resolution of the FBK VUV HD 1 SiPM. Furthermore, the minimum does not coincide with the largest operational over voltage, which in general results in a worse energy resolution due to the increase of the SiPM correlated noise. Fig. 4.22 therefore shows that, if the PDE of the FBK VUV HD 3 will be the same of its previous generation, it will allow to consider this device as an excellent candidate to the FBK VUV HD 1 for the nEXO light detection subsystem, since it satisfies the requirement on the nEXO energy resolution to be smaller (or equal) to 1%. Additionally, the requirement on the energy resolution

is satisfied up to 4 V of over voltage, differently from the previous generation of FBK devices that was limited up to 3 V of over voltage. The Hamamatsu VUV4 is instead close to meet this requirement, but its lower efficiency doesn't allow to reach a value of 1% with a detector light collection efficiency of 20%. However, an increase of the overall detector light collection efficiency to 33% (value that currently is considered as the new baseline by the nEXO collaboration), would push both devices to a significant higher energy resolution giving a value close to 0.8% for the FBK VUV HD 3 and comfortably lower than 1% (0.9%) for the Hamamatsu VUV4 MPPC, as shown in Fig. 4.23. Overall Fig. 4.22 and Fig 4.23 show as both

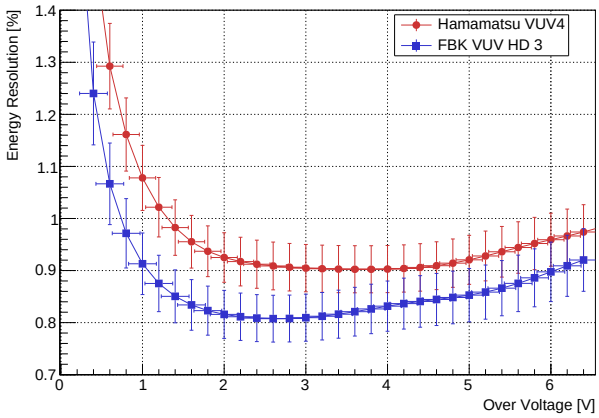

Figure 4.23: nEXO predicted energy resolution as a function of the SiPM over voltage for the two SiPMs tested in this work. Both curves include the contribution of the charge channel and use the values reported in Table 4.4. The overall detector collection efficiency was set to 33%.

SiPMs, depending on the final detector light collection efficiency, meet or are close to meet the 1 % nEXO energy resolution requirement. An additional study by the nEXO collaboration is ongoing to finalize light transport simulations of the TPC that will guide, in the next years, the final choice of the SiPM candidate for the nEXO experiment.

4.6 Conclusions

This chapter describes measurements performed at TRIUMF to characterize the properties of a new VUV sensitive SiPM at cryogenic temperatures for the nEXO experiment. In particular we characterized a new generation of FBK SiPM named FBK VUV HD 3 and compared it against the old generation of FBK devices: FBK VUV HD 1, and the Hamamatsu VUV4 MPPC. The results of this characterization are summarized in Table 4.5. For a device temperature of

Quantity	Value	Unit
Dark noise rate	0.278 ± 0.001	Hz/mm^2
Number of CAs	0.211 ± 0.004	PE
Relative fluctuation of the mean number of CAs	0.444 ± 0.009	-
Number of APAs	0.184 ± 0.003	PE
Number of CDAs	0.025 ± 0.001	-

Table 4.5: Summary of the results derived in this chapter for the characterization of the FBK VUV HD 3 SiPM. The measurements are reported for a temperature of 163 K and at 3.42 ± 0.11 V of Over Voltage. CA stands for Correlated Avalanche. APA stands for Additional Prompt Avalanches and CDA stands for Correlated Delayed Avalanches.

163 K, the FBK VUV HD 3 dark noise rate is 0.278 ± 0.001 Hz/mm^2 at 3.42 ± 0.11 V of over voltage, a level comfortably lower than what required for nEXO (< 50 Hz/mm^2). At the same over voltage setting and temperature, we measure: a number of additional prompt avalanches equal to 0.184 ± 0.003 PE, a number of correlated avalanches per pulse and a relative fluctuation of the mean number of CAs in the 1μs following the trigger pulse of 0.211 ± 0.004 PE and 0.444 ± 0.009, respectively. Additionally, we measure a number of correlated delayed avalanches per pulse in the same time window of 0.025 ± 0.001, also consistent with nEXO requirements. This last quantity is significantly lower of the ones extrapolated for the Hamamatsu VUV4 MPPC and FBK VUV HD 1 SiPM, reported in Table 3.1 and in [1], respectively. The novelty of the FBK VUV HD 3 SiPM is in fact a new triple-doping technology developed by FBK for the Darkside-20k experiment and used for the fabrication of the sensor. This new technology significantly suppresses the after-pulsing probability of this SiPM reducing therefore the number

of CDAs and CAs. This allows to increase the operational over voltage of these devices of almost 1 V if compared with its previous generation. Overall the dark characteristics of the FBK VUV HD 3 are consistent with the nEXO requirement. The efficiency of the FBK VUV HD 3 SiPM could not be finalized in this work due to an ongoing study of the light beam confinement. However, we presented a new technique, based on the time distribution between pulses, that not only is free from correlated avalanche noise corrections, but also it allows to reduce significantly the systematic uncertainly on the measured PDE, especially in the VUV wavelength range. It will be used in the near future to measure the efficiency of the FBK VUV HD 3 SiPM. Finally, at the end of this chapter, we used the data derived from the characterization of the FBK VUV HD 3 SiPM and Hamamatsu VUV4 MPPC to estimate the nEXO energy resolution, as a function of the SiPM over voltage including the contribution of the light and charge channel. More precisely assuming: (i) an efficiency for the FBK VUV HD 3 equal the one of its previous generation, (ii) a detector light collection efficiency of at least 20%, we obtained a predicted energy resolution for the FBK VUV HD 3 SiPMs compatible with the 1% requirement set by the nEXO experiment. We can therefore conclude that, if the PDE of this device will be the same of its previous generation, the FBK VUV HD 3 SiPM could be considered as an excellent alternative to the FBK VUV HD 1 SiPM for the nEXO light detection subsystem. The Hamamatsu VUV4 MPPC instead, due to its lower efficiency (Chapter 3), doesn't satisfy the nEXO energy resolution requirement. This suggests that with modest improvements in its PDE, or with an overall higher baseline value for the light collection efficiency of the nEXO detector, the Hamamatsu VUV4 MPPC could be considered as a possible alternative to FBK SiPMs for the nEXO experiment.

Chapter 5

A new detector for particle physics and beyond

5.1 Introduction

In the previous chapters of this work we characterized several SiPM photon-sensors for nEXO. In particular, we studied their contribution to the nEXO energy resolution focusing on the two main parameters that drive this quantity in the nEXO light detection subsystem: photon detection efficiency and correlated avalanche noise. Chapters 3 and 4, in particular, show as the current generation of SiPMs is limited for the following reasons: (i) high correlated avalanche noise, (ii) low photon detection efficiency for vacuum ultraviolet wavelengths. Additionally, as shown in Fig. 5.1 the current generation of SiPM is affected by low timing resolution ($>$ 100 ps) [109, 110]. While the first two quantities are strongly related to the photo-detector characteristics, the timing resolution of a large low background cryogenic experiment, such nEXO, is limited not only by the timing jitter of the photo-detectors, but also from the slow electronics that is necessary to use in order to obtain, over the entire detector, a manageable power consumption [65]. As shown in Chapter 2, for example, the current nEXO baseline design does not require a time resolution better than 100 ns. A detector with faster timing, at the ns level for example, would be however extremely beneficial for Xe-based cryogenic experiments, since it would allow not only to separate singlet

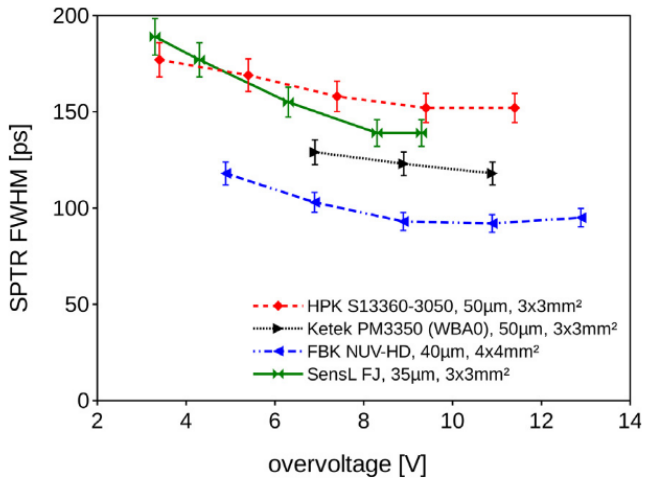

Figure 5.1: Measured Single Photon Timing Resolution (SPTR) with a 420 nm PiLas picosecond laser (42 ps FWHM intrinsic pulse width) for several SiPMs. The SPTR in nowadays devices is around 100 ps to 140 ps FWHM for a SiPM size around 3×3 mm^2. From Ref. [108].

and triplet lifetimes in xenon, useful for background discrimination (Sec. 2.3), but also to discriminate, from a timing prospective, the Cherenkov photons of the two electrons produced in the $0\nu\beta\beta$ decay that constitute a unique signature of this decay. The second part of this thesis wants to explore from a theoretical prospective Geiger mode properties of SiPMs. This study will be in fact crucial for the development, in the near future, of a new type of SiPM technology to dramatically improve energy and timing resolution of the next generation of noble liquid detectors. More precisely, we propose to develop a 3D integrated Back-side illuminated SiPM (3D B-SiPM) where every SPAD is individually connected to a Quenching Circuit and a Time-to-Digital Converter [111, 112]. This new technology would not only yield unprecedented light detection efficiency, but it would also be suitable to build detectors with 4π light coverage and ($\sim$ ps) timing resolution. Differently from the current generation of front-side illuminated SiPMs, where the incoming photons are converted into charge carriers in a shallow depletion region close to the surface [59], in B-SiPMs the back-side of the detector is what faces the incoming photons, with the depletion region extending for almost

the full thickness of the silicon substrate. Some advantages of this configuration are: 1) lower delayed correlated avalanches if compared with analog devices (after-pulsing reduction [81]); 2) early digitization by individual readout of each SPAD opens the door to in situ signal processing, limiting required data bandwidth and lowering power consumption; 3) damaged/noisy SPADs can be disabled, which can't be done with analog SiPM (otherwise compromising single photon counting ability) [113]; 4) shorter electronics transmission lines minimizing therefore the total timing jitter: a 10 ps single photon timing resolution is achievable. In addition, the back side photon-entrance window of the 3D B-SiPM is suitable to be treated with standard anti-reflective coatings technology (e.g. CCD, [114, 115]) that shows extremely low reflection in the expected scintillation spectrum of liquid xenon and argon (174.8 ± 10.2 nm [47] and 126.8 ± 7.8 nm [116], respectively). The expected low silicon surface reflectivity [92], among other characteristics, will be in fact the key component to achieve a high detector energy resolution thanks to the almost 100% photon detection efficiency that the 3D B-SiPM technology can offer.

In order to start this development, in this chapter and in the next one we report new theoretical models to better understand Geiger mode properties of SiPM. This study in fact will be crucial to optimize the electric field of the 3D B-SiPM that drives not only the device avalanche triggering probability, but also its noise performance. Disadvantage of the back-side configuration is in fact the potentially higher dark noise rate due to the extended depleted region [117–119]. The main theoretical study of Geiger mode devices properties goes back to 1972 with the work done by R. J. McIntyre [120] and by P. P. Webb [121] that is at the basis of modern semiconductor simulators. Up to now, there were not analytical models that could be used to link the micro-physics of the device, responsible for the avalanche formation, with the measured wavelength and voltage dependence of the SiPM photon detection efficiency. Moreover, it was missing a connection between the Shockley-Read-Hall thermal rate, considered to be the source of noise in Geiger mode device, and the measured voltage and temperature dependence of the SiPM dark noise rate. In the last two chapters of this work we will try to provide a physics explanation of these two mechanisms.

More precisely, in this chapter we will introduce a new model to explain the

wavelength and voltage dependence of the SiPM photon detection efficiency. We will also show how to infer from this model useful design parameters. Finally, in Chapter 6, we will provide an extension of the model presented in this chapter to predict the voltage and temperature dependence of several nuisance processes in SiPMs, named: dark noise rate, correlate delayed avalanche and direct CrossTalk. These models were tested against the measurements reported in the previous chapters of this work and against new set of data specifically collected for this study.

5.2 Characterization of SiPM Avalanche Triggering Probabilities

Thanks to the rapid evolution of signal processing and light source technologies, the field of light detection has significantly advanced over the last 10 years [122][1]. Sensors capable of detecting single photons are crucial not only in particle physics, but also in a wide range of scientific and commercial applications. SiPMs are an emerging and very promising technology that addresses the challenge of sensing, timing and quantifying low-light signals down to the single-photon level. A key parameter of SiPMs is their Photon Detection Efficiency (PDE), which is defined as the probability for a single photon of wavelength λ to produce a detectable current pulse when the SiPM is operated at a reverse bias voltage V. Experimentally, this quantity can be measured as the ratio between the number of photons producing detectable pulses and the total number of photons impinging onto the SiPM surface, usually measured with a reference detector [54]. In previous studies the PDE was parameterized as [123]

$$\mathrm{PDE} = \mathrm{FF} \cdot \mathrm{QE}(\lambda) \cdot \mathrm{T}_P(V, \lambda) \tag{5.1}$$

where FF is the Fill Factor, *i.e.* the ratio of the sensitive to total area of the device; $\mathrm{QE}(\lambda)$ is the quantum efficiency, *i.e.* the probability for an impinging photon to create a primary electron-hole pair in the active volume; $\mathrm{T}_P(V, \lambda)$ is the avalanche triggering probability, *i.e.* the probability for the generated electron-hole pair to initiate a Geiger-mode avalanche inside the depletion layer. The main drawback of

[1] This chapter was published as a standalone publication in [59]. Its content was adapted to fit the thesis structure.

Eq. 5.1 is the lack of formal separation between the different physical processes that define the total PDE. Absorption and avalanche triggering probabilities are in fact correlated, since the latter probability depends on where the photon is absorbed. Internal and optical quantum efficiency are also not formally separated in Eq. 5.1 and the lack of an analytical expression for $T_P(V, \lambda)$ brings to the need to introduce for each SiPM a different data-driven parametrization of their PDE (*e.g.* [58, 123]). In this chapter we propose a new formulation of the SiPM PDE that accounts for the position of photon-absorption and allows to infer key insight on the electric field structure within SiPMs. This new parametrization predicts the PDE as a function of the reverse bias voltage and wavelength, corresponding to attenuation lengths in silicon between a few nanometers and several tens of micrometers, specifically accounting for the transition from electron-driven avalanches (close to the surface), to hole-driven avalanches (deeper inside the silicon) in p-on-n SiPMs. The model has been successfully applied to characterize the response of three SiPMs: two Hamamatsu Multi-Pixel Photon Counter (MPPC)s and one Fondazione-Bruno-Kessler (FBK) SiPM, and it can be extended to any other SiPM including n-on-p devices.

5.2.1 Parametrization of the SiPM PDE

5.2.1.1 Model for Single Photon Avalanche Diodes

SiPMs are arrays of SPADs separated by guard rings and other structures, such as trenches to suppress optical CrossTalk [124]. The field at the edge of each SPAD is expected to be distorted by the proximity of the isolation structures [125]. Nevertheless, the small fraction of the SPAD area affected by edge effects and the uniformity of the electric field in the SPAD depletion layer allows to treat the parametrization of the SiPM PDE as a one-dimensional problem [126]. This approximation may not apply to ultra-high-density SiPMs with very small SPADs [125]. Each SiPM SPAD is a reversely biased p-n junction, operated above breakdown. In this configuration, a photo-generated carrier (electron or hole) entering the depletion layer may trigger an avalanche [127]. Not every carrier, however, will induce one. Carriers can travel undisturbed or lose energy by interacting with the lattice, recombining before the junction reaches breakdown [128]. Additionally,

electrons (holes) may be lost if they diffuse to the silicon surface (into the silicon substrate).

It is therefore possible to associate a finite probability of triggering an avalanche to each carrier depending on the SPAD reverse bias voltage V and on the position x in which the carrier enters or is generated in the depletion layer: $\mathrm{P}_e(x,V)$ or $\mathrm{P}_h(x,V)$ [120]. Fig. 5.2 shows the electric field of a typical p-n junction for a p-on-n SiPM simulated with the Lumerical DEVICE simulation package [129]. The electric field has a maximum at the p-on-n transition labeled x_{PN}. The depletion layer starts at d_P (on the P^+ side) and ends at d_W (on the N side), defining the total junction width of $W \equiv (d_W - d_P)$. Fig. 5.2 also shows the combined avalanche triggering probability $\mathrm{P_P}(x,V)$ that an electron-hole pair will trigger an avalanche within the depleted region

$$\mathrm{P_P}(x,V) \equiv \Big(\mathrm{P}_e(x,V) + \mathrm{P}_h(x,V) - \mathrm{P}_e(x,V) \cdot \mathrm{P}_h(x,V)\Big)$$

This probability is electron-driven at $x = d_P$ and hole-driven at $x = d_W$, yielding $\mathrm{P_P}(d_P,V) = \mathrm{P}_e(d_P,V)$ and $\mathrm{P_P}(d_W,V) = \mathrm{P}_h(d_W,V)$, respectively [127]. The probability is smaller on the N side due to the significantly lower impact-ionization-coefficient for holes compared to electrons [130]. Carriers created outside of the depleted region may contribute to the total PDE reaching the depletion layer by drifting or diffusing and subsequently triggering an avalanche. In this case, the probability that a carrier reaches the depleted region depends on its lifetime, on the carrier mobility and on the original position of photo-generation [128, 131].

5.2.1.2 Modelling photon absorption and carrier transport

The probability that a single photon of wavelength λ is absorbed between x and $x + dx$ as a function of the photon attenuation length $\mu(\lambda)$ is:

$$d\mathrm{P_{Abs}}(x) = \frac{1}{\mu} \exp\left(-\frac{x}{\mu}\right) dx \tag{5.2}$$

The photon absorption results in the generation of one or more electron-hole pairs [132]. Depending on the photon attenuation length and on the location and exten-

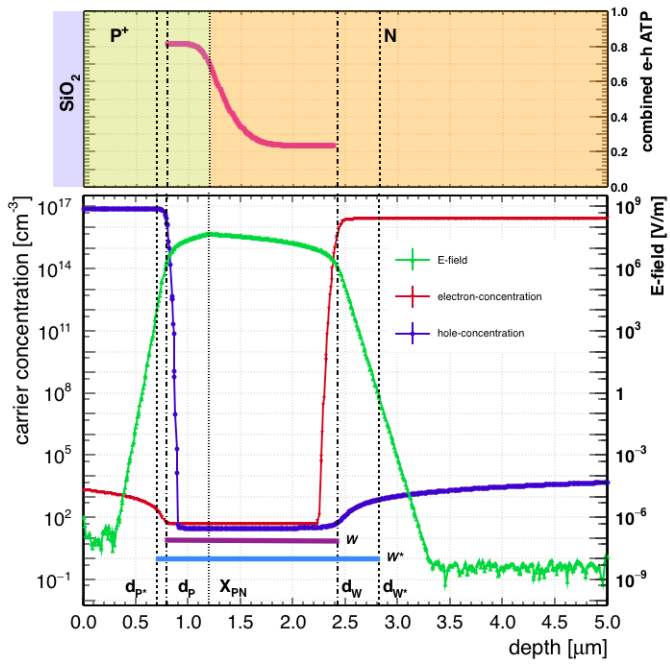

Figure 5.2: p-on-n SPAD simulated with Lumerical DEVICE. The SPAD has an asymmetric constant doping concentration of $N_{P^+} = 7.5 \cdot 10^{16}$ cm^{-3} and $N_N = 2.5 \cdot 10^{16}$ cm^{-3}. The breakdown voltage for this configuration is $V_{BD} = 36.3$ V. Top: Combined electron-hole Avalanche Triggering Probability (ATP): $P_P(x,V)$, within the depletion layer for a bias voltage of 40 V. Bottom: Carrier (electron-hole) concentration and electric field profile. d_P and d_W mark the edges of the depletion layer. Additionally, x_{PN} is the position of maximum electric field, while d_{P^*} and d_{W^*} are the edges of the effective photon collection region. Different factors like carrier mobility and recombination time contribute to defining the exact location of d_{P^*} and d_{W^*}.

sion of the microcell depletion layer, the avalanche process can be reduced to one of these three independent mechanisms [133]:

1. The photon is absorbed in the quasi-neutral upper layer ($x \in [0, d_P]$). The photo-generated electron diffuses (or drifts) to the depleted region triggering an avalanche with probability $P_{\text{tr-e}}(x) \cdot P_e(d_P, V)$, where $P_{\text{tr-e}}(x)$ is the

probability for the electron produced at x to reach the upper depletion layer boundary d_P.

2. The photon is absorbed in the depleted layer ($x \in [d_P, d_W]$). The photo-generated electron-hole pair triggers an avalanche with probability $\mathrm{P_P}(x,V)$.

3. The photon is absorbed in the quasi-neutral lower layer ($x \geq d_W$). The photo-generated hole diffuses (or drifts) to the depleted region triggering an avalanche with probability $\mathrm{P_{tr\text{-}h}}(x) \cdot \mathrm{P}_h(d_W, V)$, where $\mathrm{P_{tr\text{-}h}}(x)$ is the probability for the hole produced at x to reach the lower depletion layer boundary d_W.

The second process is the dominant mechanism for the avalanche breakdown [134]. Nevertheless, the drift and diffusion of minority carriers from the neutral regions contribute to the total PDE, but produce significant delays in the avalanche generation, as shown experimentally in [135] and numerically in [126]. The data reported in this chapter are not directly sensitive to time delays in the avalanche generation (Sec. 5.2.2). Diffusing or drifting electrons (holes), in particular, have the same probability to create avalanches once they enter the depletion layer, regardless of their original creation depth, *i.e.* $\mathrm{P}_e(d_P, V)$ $\left(\mathrm{P}_h(d_W, V)\right)$. We can therefore simplify the transport of the photo-generated carriers in the depleted region by introducing two effective depth parameters: d_{P^*} and d_{W^*}, such that electrons (holes) photo-generated between d_{P^*} and d_P (d_W and d_{W^*}) always reach the depletion layer boundaries at d_P (d_W) (Fig. 5.2). With this simplification the electron and hole transport probabilities $\mathrm{P_{tr\text{-}e}}(x)$ and $\mathrm{P_{tr\text{-}h}}(x)$ become step functions as follows:

$$\mathrm{P_{tr\text{-}e}}(x) = \begin{cases} 1 \text{ if } x \in [d_{P^*}, d_P] \\ 0 \text{ else} \end{cases} \tag{5.3}$$

$$\mathrm{P_{tr\text{-}h}}(x) = \begin{cases} 1 \text{ if } x \in [d_W, d_{W^*}] \\ 0 \text{ else} \end{cases} \tag{5.4}$$

5.2.1.3 Modelling the probability of triggering avalanches within the junction

The SiPM PDE for a wavelength λ can be obtained by combining the probability of photon absorption (Eq. 5.2) with the simplified transport probabilities (Eq. 5.3 and Eq. 5.4) and with the combined electron-hole avalanche triggering probability $\mathrm{P_P}(x,V)$ as:

$$\mathrm{PDE}_\lambda = \varepsilon_0 \cdot \int_{d_{P^*}}^{d_{W^*}} \frac{1}{\mu} \exp\left(-\frac{x}{\mu}\right) \cdot \mathrm{P_P}(x,V)\, dx \tag{5.5}$$

where ε_0 is the optical quantum efficiency, *i.e.* the probability that a photon is transmitted in the silicon. This quantity depends on the SPAD fill factor (Sec. 5.2) and reflectivity [58]. The integral quantity represents instead the internal quantum efficiency , *i.e.* the probability that a photon is absorbed in the sensitive volume of the detector and triggers a self-sustained avalanche process.

The main drawback of Eq. 5.5 is that it cannot be expressed using only measurable quantities. The combined electron-hole avalanche triggering probability $\mathrm{P_P}(x,V)$, for example, can be calculated numerically by solving a differential equation that depends on the generally unknown SPAD electric field [120]. Therefore, an expression of Eq. 5.5, suitable for SiPM characterization, requires a second approximation in addition to the effective model of the quasi-neutral regions introduced in Sec. 5.2.1.2. Precisely, the avalanche triggering probability $\mathrm{P_P}(x,V)$ is simplified with a step function considering its asymptotic values at the microcell depletion layer boundaries such that[2]

$$\mathrm{P_P}(x) \sim \begin{cases} \mathrm{P}_e(d_P) & \text{if } x \in [d_{P^*}, x_{PN}] \\ \mathrm{P}_h(d_W) & \text{if } x \in [x_{PN}, d_{W^*}] \end{cases} \tag{5.6}$$

With Eq. 5.6, Eq. 5.5 can be integrated exactly obtaining:

$$\mathrm{PDE}_\lambda = \mathrm{PDE_{MAX}} \cdot \left(\mathrm{P}_e(d_P) \cdot f_e^* + \mathrm{P}_h(d_W) \cdot (1 - f_e^*) \right) \tag{5.7}$$

[2]From here on to keep the notation simple, we will drop the voltage dependence of these quantities.

where

$$\mathrm{PDE_{MAX}} \equiv \varepsilon_0 \exp\left(-\frac{d_{P^*}}{\mu}\right)\left(1-\exp\left(-\frac{W^*}{\mu}\right)\right) \tag{5.8}$$

with $W^* \equiv \left(d_{W^*} - d_{P^*}\right)$, the length of the effective region in which an absorbed photon can initialize an avalanche process[3]. $\mathrm{PDE_{MAX}}$ represents the saturation PDE for a wavelength λ and it is defined as the product of three quantities: (i) the optical efficiency (Sec. 5.2.1.3), (ii) the probability that a photon is transmitted through the upper quasi neutral layer, and (iii) the probability that a photon is absorbed within the effective depletion zone W^*. The fraction

$$f_e^* \equiv \left[\frac{1-\exp\left(-\frac{(x_{PN}-d_{P^*})}{\mu}\right)}{1-\exp\left(-\frac{W^*}{\mu}\right)}\right] \in [0,1] \tag{5.9}$$

represents the fraction of electron-driven avalanches for a wavelength λ. It depends on $\left(x_{PN} - d_{P^*}\right)$: the length of the region in which avalanches are triggered by an electron. Considering the weak voltage dependence around the breakdown of $\left(x_{PN} - d_{P^*}\right)$ and W^* [131], $\mathrm{PDE_{MAX}}$ and f_e^* will be considered as voltage-independent quantities. An experimental validation of this approximation will be proposed in Sec. 5.2.2. It is worth noting that Eq. 5.5 neglects the multi-carrier production per single photon by assuming a quantum yield of 1. This process that happens in the UV-B, UV-C and Vacuum Ultraviolet (VUV) wavelength range (< 320 nm [132]) may affect the total internal quantum efficiency and a separate work is needed to study PDE_λ in this wavelength range.

5.2.1.4 Inferring the electron-hole avalanche triggering probabilities

The evaluation of $\mathrm{P}_e(d_P)$ and $\mathrm{P}_h(d_W)$ in Eq. 5.7 is a complicated numerical problem [120]. Inspection of Eq. 5.7 shows an elegant way to find $\mathrm{P}_e(d_P)$ experimentally, without the need to know the microcell electric field. In particular, if the attenuation length for a given wavelength is such that $f_e^* \sim 1$ (i.e. short attenuation

[3] $W^* \geq W$ due to the extended junction boundaries (Sec. 5.2.1.2).

length), then Eq. 5.7 reduces to

$$\mathrm{PDE}_{\lambda} \sim \mathrm{PDE}_{\mathrm{MAX}} \cdot \mathrm{P}_e(d_P) \tag{5.10}$$

In this case, PDE_{λ} simply reduces to $\mathrm{P}_e(d_P)$ since $\mathrm{PDE}_{\mathrm{MAX}}$ is assumed to be voltage independent (Sec. 5.2.1.3). The condition $f_e^* \sim 1$ for a p-on-n microcell is well verified at UV wavelengths due to short attenuation lengths [136]. More generally, the condition $f_e^* \sim 1$ could be also verified for longer wavelengths depending of the junction structure. We propose an approximate empirical expression to overcome the difficulty to fit the PDE of UV wavelengths as a function of the reverse bias voltage V. Following an approach similar to the one developed in [137] (see also Sec. 5.2.1.5), $\mathrm{P}_e(d_P)$ can be expressed as

$$\mathrm{P}_e(d_P) = \left[1 - \left(k_e \cdot V \cdot \exp\left(-k_{e2}/\sqrt{V}\right)\right)^{-2}\right] \tag{5.11}$$

where k_e and k_{e2} are two voltage-independent parameters. The problem in evaluating $\mathrm{P}_h(d_W)$ can be solved by introducing a parameter k that represents an effective ratio of the impact-ionization-coefficients [120]. In this way $\mathrm{P}_h(d_W)$ can be derived from $\mathrm{P}_e(d_P)$ as follows

$$\mathrm{P}_h(d_W) = \left[1 - \left(1 - \mathrm{P}_e(d_P)\right)^{\mathrm{k}}\right] \tag{5.12}$$

This equation allows to express Eq. 5.7 in term of $\mathrm{P}_e(d_P)$ and k only[4].

5.2.1.5 Evaluation of the ionization integral and Eq. 5.11

The ionization integral δ (*i.e.* the average number of ionization per carrier pair) can be computed as [138]

$$\delta = \left\langle \int_{d_P}^{x_i} \alpha_e(E)\mathrm{d}x + \int_{x_i}^{d_W} \alpha_h(E)\mathrm{d}x \right\rangle \tag{5.13}$$

[4]It is worth recalling what was stated in Sec. 5.2.1.3 that, even if in the UV-B, UV-C and VUV wavelength range photon avalanches are electron driven in p-on-n SiPMs, the multi-carrier production per single photon may artificially increase the internal junction efficiency. Eq. 5.7 assumes a quantum yield of 1, therefore Eq. 5.10, that is derived from it, can only be used in the UV-A range when this mechanism is not yet relevant [132].

where $\alpha_e(E)$ and $\alpha_h(E)$ are the ionization coefficients of an electron and a hole, respectively, which have originated from an ionization which occurred at x_i, and the average is on i. E is the electric field module.[5] Since $\alpha_e(E) >> \alpha_h(E)$ the previous equation can be simplified as [138]

$$\delta \sim \mathrm{C} \cdot \int_{d_P}^{d_W} \alpha_e(E) \mathrm{d}x \tag{5.14}$$

where C is a constant near unity. The major contribution to the integrand of Eq. 5.14 occurs at fields close to the maximum electric field E_{MAX} [138], therefore Eq. 5.14 can be simplified as

$$\delta \sim \mathrm{C} \cdot \alpha_e(E_{\mathrm{MAX}}) \cdot W \tag{5.15}$$

where $W = (d_W - d_P)$ is the junction width. According to [131], $\alpha_e(E)$ can be parameterized as

$$\alpha_e(E) = A \cdot E \cdot \exp\left(-\frac{B}{E}\right) \tag{5.16}$$

where A and B are two model dependent parameters [139]. Substituting Eq. 5.16 in Eq. 5.15, δ becomes

$$\delta \sim \mathrm{C} \cdot A \cdot E_{\mathrm{MAX}} \cdot \exp\left(-\frac{B}{E_{\mathrm{MAX}}}\right) \cdot W \tag{5.17}$$

The maximum electric field as a function of the reverse bias voltage V is [62]

$$E_{\mathrm{MAX}} = E_{\mathrm{MAX0}}\left(1 + \frac{V}{V_i}\right)^{(1-p)} \sim E_{\mathrm{MAX0}}\left(\frac{V}{V_i}\right)^{(1-p)} \tag{5.18}$$

where E_{MAX0} is the zero-bias maximum electric field, V_i is the built in potential and $p \in [0,1]$ is the ideality factor [131]. The depletion layer width is given by [62]

$$W = W_0\left(1 + \frac{V}{V_i}\right)^{p} \sim W_0\left(\frac{V}{V_i}\right)^{p} \tag{5.19}$$

[5] The ionization coefficients represent the number of electron-hole pairs generated per unit distance and and they are strong function of the electric field

where W_0 is the depletion layer width at zero-bias. The additional simplification in Eq. 5.18 and Eq. 5.19 holds since, after breakdown, $\frac{V}{V_i} >> 1$. Finally, if we combine Eq. 5.18 and Eq. 5.19 with Eq. 5.17, we can write δ as

$$\delta \sim k_e \cdot V \cdot \exp\left(\frac{-k_{e2}}{V^{(1-p)}}\right) \tag{5.20}$$

where k_e and k_{e2} are two parameters that absorb all the constants. The choice of p has no strong influence on the model behaviour. In this work we used $p = \frac{1}{2}$. $\mathrm{P}_e(d_P)$ follows then as [138]

$$\mathrm{P}_e(d_P) = 1 - \delta^{-2} \tag{5.21}$$

or explicitly

$$\mathrm{P}_e(d_P) = \left[1 - \left(k_e \cdot V \cdot \exp\left(-k_{e2}/\sqrt{V}\right)\right)^{-2}\right] \tag{5.22}$$

that matches Eq. 5.11.

5.2.1.6 Data analysis procedure

The procedure to characterize the SiPM PDE for p-on-n junction structures and for different wavelengths is:

- Measure $\mathrm{P}_e(d_P)$ by fitting the SiPM PDE as a function of the reverse bias voltage using short wavelengths (*e.g.* UV-A) and Eq. 5.10 (combined with Eq. 5.11). This sets the three voltage-independent fitting parameters: k_e, k_{e2}, and $\mathrm{PDE_{MAX}}$.

- Fit the SiPM PDE as a function of the reverse bias voltage for the other available wavelengths with Eq. 5.7 and a unique χ^2 minimization. Eq. 5.7 has four fitting parameters $\left(x_{PN} - d_{P^*}\right)$, k, W^* and $\mathrm{PDE_{MAX}}$. The first three parameters are (approximately) wavelength and voltage independent, while $\mathrm{PDE_{MAX}}$ is a voltage-independent, but wavelength-dependent parameter.

5.2.2 Model validation

In this section we will apply the model introduced in Sec. 5.2.1.3 to characterize the voltage and wavelength dependence of the PDE of three SiPMs with the same junction structure (p-on-n). The first SiPM is a Hamamatsu H2017 MPPC whose characterization was reported in [94] (Sec. 5.2.2.1). The PDE of this MPPC was studied in the range $[400-640]$ nm at a temperature of 23.6 °C using a pulse frequency method (corrected for the SiPM correlated avalanche noise [64]) and a calibrated photodiode as reference to calibrate the absolute light flux. The other two SiPMs are: (i) a Hamamatsu VUV4 MPPC (S/N: S13370-6152), and (ii) a FBK Low Field (LF) SiPM (Sec. 5.2.2.2). The last two SiPMs were already tested

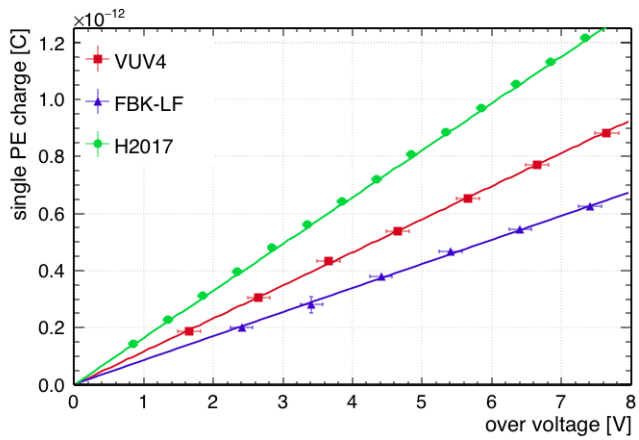

Figure 5.3: Single Photo-electron Equivalent (PE) charge as a function of the over voltage (difference between the reverse bias voltage and the breakdown voltage) for the three tested devices.

in Chapter 3 at 175 nm as possible candidates for the nEXO experiment. The model introduced in this chapter cannot be applied directly in the VUV wavelength range due to the higher quantum yield of VUV photons (Sec. 5.2.1.3). The two SiPMs were therefore tested specifically for this work in a different wavelength range using the following wavelengths: 378 nm, 444 nm and 782 nm. The three wavelengths were obtained with a Hamamatsu Photonics laser controller C10196 operated at 500 Hz with PLP-10 laser heads. The experimental technique used to measure the SiPMs PDE is reported in Chapter 3. Precisely, the average number

of photons detected by the SiPM ($\mu_\lambda^{\text{SiPM}}$) was first measured by counting the number of laser flashes in which no SiPM pulses were detected (N_0). Using Poisson statistics, $\mu_\lambda^{\text{SiPM}}$ can then be expressed as:

$$\mu_\lambda^{\text{SiPM}} = -\ln\left(\frac{N_0}{N_{\text{TOT}}}\right) - \mu_{\text{DN}} \tag{5.23}$$

where N_{TOT} is the total number of laser flashes. This method is independent of correlated avalanches [58] and it requires only correcting for the average number of dark noise pulses in the trigger window (μ_{DN}) [54]. The absolute PDE can then be obtained dividing $\mu_\lambda^{\text{SiPM}}$ for the effective number of photons produced by the pulsed laser at the SiPM location (N_λ), assessed with a reference detector, as:

$$\text{PDE}_\lambda = \left(\frac{\mu_\lambda^{\text{SiPM}}}{N_\lambda}\right) \tag{5.24}$$

The PDE of the Hamamatsu VUV4 MPPC and the FBK LF SiPM were measured at $-40\ ^\circ$C and $-60\ ^\circ$C to prevent dark noise overwhelming the light signal. The dependence of the attenuation length on the temperature in Eq. 5.9 and Eq. 5.8 for the three SiPMs was accounted considering the temperature coefficients reported in [136].

In addition, for each SiPM the single Photo-electron Equivalent (PE) charge ($Q_{1\ \text{PE}}$) was also extrapolated from the single PE gain, as discussed in [54]. $Q_{1\ \text{PE}}$ was then linearly fitted as a function of the bias voltage as $Q_{1\ \text{PE}} = C_D \times (V - V_{BD})$ in order to extract for each SiPM: (i) the single cell capacitance C_D, (ii) the Breakdown Voltage V_{BD} defined as the bias voltage at which the SiPM single PE charge (or gain) is zero. The results are shown in Fig. 5.3 as a function of the over voltage[6]. The extrapolated capacitance and breakdown voltages are reported in Table 5.1 and Table 5.2. The well tested linear dependence in Fig. 5.3 gives an experimental verification of the weak voltage dependence of $\left(x_{PN} - d_{P^*}\right)$ and W^* close to the breakdown voltage (Sec. 5.2.1.3) showing as the changing of the single SPAD junction capacitance (and therefore the changing of the single SPAD junction width) can be

[6]The over voltage is defined as the difference between the reverse bias voltage and the breakdown voltage V_{BD}.

neglected and $\mathrm{PDE_{MAX}}$ (Eq. 5.8) and f_e^* (Eq. 5.9) can be considered as voltage-independent quantities close to the breakdown.

Finally, it is worth noting that the shortest wavelength measured in the next sections is 378 nm whose quantum yield is 1, in agreement with the discussion of Sec. 5.2.1.3.

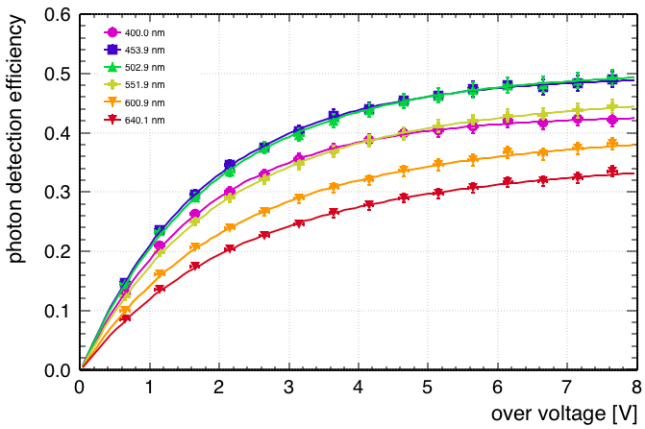

Figure 5.4: Absolute PDE as a function of the over voltage for the Hamamatsu H2017 MPPC for wavelengths in the range $[400-640]$ nm. The complete data-set accounts for a wavelength scan with a resolution of ~ 5 nm (here displayed every 50 nm). The solid lines represent fits performed with Eq. 5.10 for the 400 nm data, and the combined fit with Eq. 5.7 for the other wavelengths.

5.2.2.1 Analysis of the Hamamatsu H2017 MPPC

The absolute PDE of the Hamamatsu H2017 as a function of the over voltage is reported for different wavelengths in Fig. 5.4. The solid lines represent fits performed with Eq. 5.10 and Eq. 5.7. First, the 400 nm data ($\mu(400\text{ nm}) \sim 0.1$ µm) were fitted with Eq. 5.10 (combined with Eq. 5.11) to constrain $\mathrm{P}_e(d_P)$, as described in Sec. 5.2.1.4. The other wavelengths were then fitted using Eq. 5.7, with the $\mathrm{P}_e(d_P)$ constrained by the 400 nm fit, and $\left(x_{PN} - d_{P^*}\right)$, k, W^* and $\mathrm{PDE_{MAX}}$ as free parameters. The measured effective value for $\mathrm{k_{H2017}} = 0.25 \pm 0.06$. The width of the e-triggered avalanche layer is 1.8 ± 0.1 µm and the effective junction

Type	$(x_{PN} - d_{P^*})$ [μm]	W^* [μm]	C_D [fF]
H2017 [94]	1.8 ± 0.1	4.1 ± 0.4	163 ± 1
VUV4 [54]	0.8 ± 0.2	3.9 ± 0.8	116 ± 6
LF [1]	0.145 ± 0.01	2.2 ± 0.1	83 ± 5

Table 5.1: Comparison of the fit parameters derived for the three tested devices (1/2). $\left(x_{PN} - d_{P^*}\right)$ represents the length of the region in which avalanches are triggered by an electron. W^* is the length of the effective region in which an absorbed photon can initialize an avalanche process. C_D is the single cell capacitance extrapolated from the single PE gain.

Type	V_{BD} [V]	W [μm]	k
H2017 [94]	52.2 ± 0.1	1.54 ± 0.01	0.25 ± 0.06
VUV4 [54]	48.3 ± 0.1	1.01 ± 0.05	0.07 ± 0.06
LF [1]	30.6 ± 0.1	0.92 ± 0.06	0.05 ± 0.01

Table 5.2: Comparison of the fit parameters derived for the three tested devices (2/2). V_{BD} is the breakdown voltage. W is the physical junction width derived using: (i) the pixel size, (ii) the fill factor provided by each manufacturer and (iii) C_D (*e.g.* [135]). k is an effective ratio of the impact-ionization-coefficients as reported in [120].

width is $W^* = 4.1 \pm 0.4$ μm. This last quantity can be compared with the physical junction width $W = 1.54 \pm 0.01$ μm derived as shown in [135] from the single cell capacitance C_D (Sec. 5.2.2). W^* is bigger than W in agreement with the effect of carrier drift and diffusion described in Sec. 5.2.1.3. Additionally, $\mathrm{PDE_{MAX}}$ and f_e^* (this last quantity extrapolated using Eq. 5.9) are reported in Fig. 5.5 as a function of the wavelength. f_e^* represents the fraction of electron driven avalanches (Sec. 5.2.1.3). It decreases with increasing wavelength which reflects the fact that longer wavelengths are absorbed deeper in the microcell (closer to the N side) and a considerable contribution to the total PDE thus comes from hole-driven avalanches.

5.2.2.2 Analysis of the Hamamatsu VUV4 MPPC and FBK LF SiPM

The same analysis as for the H2017 SiPM was applied for the Hamamatsu VUV4 MPPC and the FBK LF SiPM. In this case we were only interested in rel-

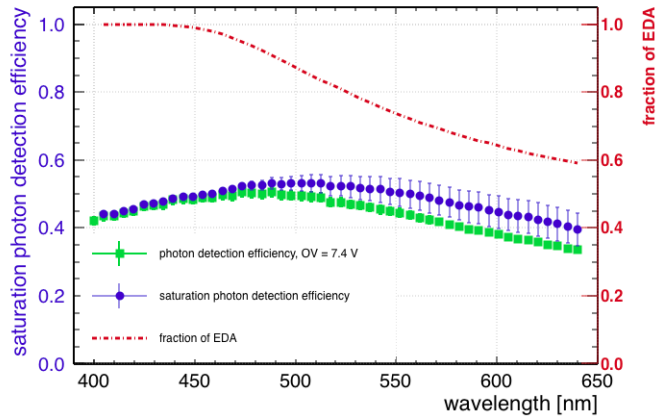

Figure 5.5: Fraction of Electron Driven Avalanches (EDA) (f_e^*, derived using Eq. 5.9 and the fit results reported in Table 5.1 and Table 5.2) and saturation PDE ($\mathrm{PDE_{MAX}}$) plotted as a function of the wavelength for the H2017 Hamamatsu MPPC. Due to the slower saturation of the hole probability ($\mathrm{P}_h(d_W)$) compared to the electron one ($\mathrm{P}_e(d_P)$) (see also Fig. 5.7), the error on the saturation PDE increases with increasing wavelength. For comparison, in this figure is also reported the PDE at the highest over voltage of Fig. 5.4.

ative changes of the PDE for different wavelengths, therefore the absolute light fluxes were not calibrated. In Fig. 5.6 we report the average number of photons detected for these two SiPMs ($\mu_\lambda^{\mathrm{SiPM}}$, Eq. 5.23) as a function of the over voltage. The solid and dashed lines represent fits performed with Eq. 5.10 for the 378 nm data ($\mu(378\ \mathrm{nm}) \sim 0.03\ \mu\mathrm{m}$). The other two wavelengths were fitted together using Eq. 5.7 and the four free parameters introduced in Sec. 5.2.1.6. The effective k values derived from the fit for the FBK LF and the Hamamatsu VUV4 are $\mathrm{k_{LF}} = 0.05 \pm 0.01$ and $\mathrm{k_{VUV4}} = 0.07 \pm 0.06$, respectively[7]. For the FBK LF (Hamamatsu VUV4) the width of the e-triggered avalanche layer is $0.145 \pm 0.01\ \mu\mathrm{m}$

[7]The uncertainty on the parameter k is related to the slow saturation of the hole probability compared with the electron one. See Fig. 5.7. The current generation of SiPMs suffers from correlated avalanche noise that increases with the over voltage as shown in Chapters 3 and 4, therefore SiPMs can be operated only up to few volts of over voltage [64]. The progresses on reducing correlated avalanche noise are however encouraging (*e.g.* [84]) and the next generations of SiPMs should feature a reduced correlated avalanche noise that will allow the operation of these devices at higher over voltages, constraining the error on k and therefore the uncertainty on $\mathrm{P}_h(d_W)$.

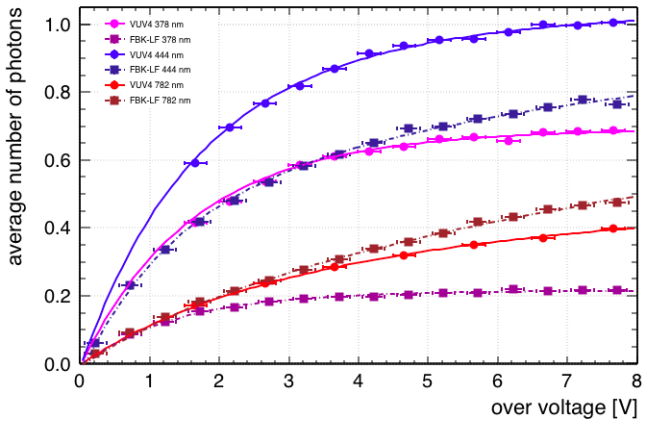

Figure 5.6: Average number of photons detected by the Hamamatsu VUV4 MPPC and the FBK LF SiPM ($\mu_\lambda^{\mathrm{SiPM}}$, Eq. 5.23) as a function of the over voltage for not calibrated light fluxes. The solid and dashed lines represent the fits performed with Eq. 5.10 for the 378 nm data and the combined fit with Eq. 5.7 for the other two wavelengths.

(0.8 ± 0.2 μm) and the effective junction width is 2.2 ± 0.1 μm (3.9 ± 0.8 μm). The effective junction of the Hamamatsu VUV4 is less symmetric than the one of the Hamamatsu H2017. Instead the FBK LF has a smaller electron dominated thickness suggesting a stronger doping asymmetry. Additionally, the physical junction width of the Hamamatsu VUV4 (FBK LF) is 1.01 ± 0.05 μm (0.92 ± 0.06 μm). Both these lengths are smaller than the corresponding effective ones and again compatible with the model described in Sec. 5.2.1.3. In Table 5.1 and Table 5.2 we report a summary of the fit parameters for the three SiPMs. An additional comparison between the three devices can be drawn analyzing their electron/hole avalanche triggering probabilities: $\mathrm{P}_e(d_P)$ and $\mathrm{P}_h(d_W)$, as reported in Fig. 5.7. The $\mathrm{P}_e(d_P)$ of the three SiPMs saturates faster then the corresponding $\mathrm{P}_h(d_W)$. This aspect is related to higher impact-ionization-coefficient of electrons compared to holes [127]. Additionally, Fig. 5.7 shows that the two Hamamatsu devices have almost the same electron avalanche triggering probabilities, while those of the FBK LF are noticeably different. $\mathrm{P}_e(d_P)$ ($\mathrm{P}_h(d_W)$) at fixed over voltage is always larger (smaller) for the FBK LF than for the Hamamatsu MPPCs, indicating that the FBK LF is more

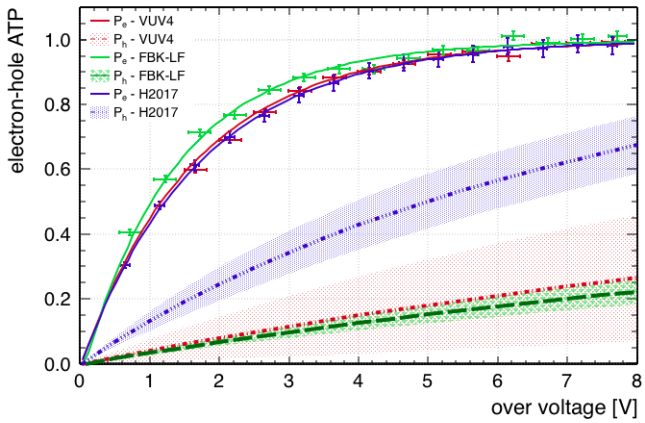

Figure 5.7: Electron and hole Avalanche Triggering Probability (ATP): $P_e(d_P)$ and $P_h(d_W)$, for the three SiPMs analyzed in this chapter. For each $P_e(d_P)$ are also reported the data of Fig. 5.4 and Fig. 5.6 used to obtain the corresponding curve. Each $P_h(d_W)$ is derived using Eq. 5.12. The dashed regions represent the uncertainty on the hole probabilities $P_h(d_W)$ due to the uncertainty on the effective k-values of Table 5.1 and Table 5.2.

sensitive to UV wavelengths since, for these wavelengths, the avalanche mechanism is driven by electrons (Sec. 5.2.1.4). The lower sensitivity of the Hamamatsu VUV4 MPPC in the VUV range was in fact measured in Chapter 3. The reported saturation PDE of the Hamamatsu VUV4 MPPC and the FBK LF SiPM at an average wavelength of 189 ± 7 nm are 14.8 ± 2.8 % and 22.8 ± 4.3 %, respectively[8]. It is worth noting, however, that we cannot conclude that the higher efficiency of the FBK LF is exclusively due to a more optimised internal structure (*i.e.* higher avalanche triggering probability). Surface reflectivity, as well as junction depth, can also play an important role in defining the total PDE, as shown by Eq. 5.8.

5.2.3 Design considerations for the next generation of SiPMs

The model presented in this chapter can be used to extrapolate useful design parameters to build new generations of SiPMs. The avalanche triggering prob-

[8]The Hamamatsu VUV4 MPPC and the FBK LF SiPM were designed to cover the same spectral range.

abilities can in fact be linked to the device micro-physics using the constant k approximation introduced in Sec. 5.2.1.4.

In Sec. 5.2.1.5 we defined the average number of ionization per carrier pair as $\delta \sim \int_{d_p}^{d_W} \alpha_e(x)\,\mathrm{dx}$. This quantity can be experimentally extrapolated from the avalanche triggering probabilities as follows [120]

$$e^{(1-\mathrm{k})\delta} = \frac{\mathrm{P}_e(d_P)}{1-\mathrm{P}_e(d_P)}\left[\frac{(1-\mathrm{P}_e(d_P))^{\mathrm{k}}}{1-(1-\mathrm{P}_e(d_P))^{\mathrm{k}}}\right] \tag{5.25}$$

since $\mathrm{P}_e(d_P)$ and k can be derived from the fitting procedure presented in the previous sections of this chapter. Additionally, not only δ, but also the parameter k is linked to the device micro-physics, since it represents an effective ratio of the ionization coefficient. In Ref. [120] it was defined as

$$\mathrm{k} = \frac{\alpha_h(E)}{\alpha_e(E)} \tag{5.26}$$

where E is the electric field. Therefore δ and k represent two different parameters to inspect the junction characteristics. While the first one is sensitive to the junction electric field module and width, the second one depends mainly from the electric field module. k, in particular, increases with the electric field [120], therefore a

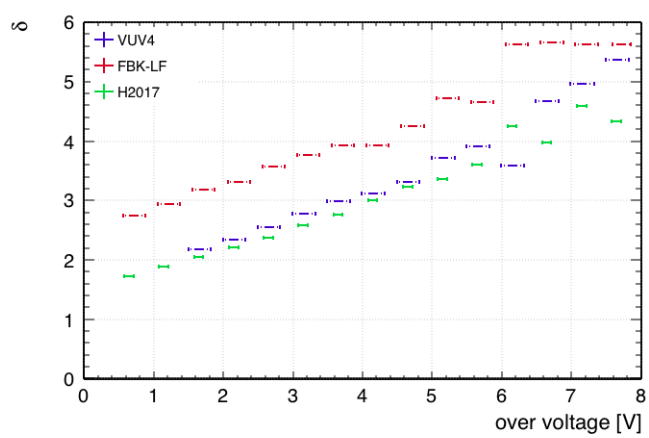

Figure 5.8: Number of ionization carriers produced along the carrier path derived using Eq. 5.25 for the three devices tested in this chapter.

lower k is related, on average, to a lower electric field in the junction.

Fig. 5.8 reports the average number of ionization per carrier pair for the three tested devices extrapolated using Eq. 5.25. The FBK LF has the highest δ. From this follows that even if the junction of the FBK LF has a smaller capacitance (Table 5.1) and field (lower k, Table 5.2) if compared with the ones of the other two SiPMs tested, its junction has a more efficient electric field structure since, on average, a carrier produces more-electron hole pair during the avalanche formation. Therefore, a lower peak field associated with a wider junction is more efficient during the avalanche formation. The superior structure of the FBK LF SiPM is also visible in Fig. 5.7 that shows as the FBK LF electron avalanche triggering probability saturates faster with over voltage if compared with the one of the other two SiPMs.

Figure 5.8 coupled with the extraction of the k and δ parameters proposes a way to optimize new generations of p-on-n SiPMs: reduce the field and increase the junction width is in fact the key to achieve a faster saturation of the electron avalanche triggering probability and therefore a higher ionization efficiency. This configuration can be achieved with p-i-n junction structures rather than simple p-n structures, as shown in [108].

The k and δ parameters can be precisely estimated when performing semiconductor simulations, as shown in Fig. 5.2, since the electric field in the junction is known. Reduce k or, in other words, optimize the electric field in the junction in order to obtain a high δ, will therefore be the key to design new generations of more efficient p-on-n SiPMs.

5.3 Conclusions

In this chapter we have presented a new analytical model to describe the SiPM PDE as a function of the reverse bias voltage. The new model was used to explain the wavelength dependence of the SiPM PDE, attributed to a combination of electron and hole avalanche triggering probabilities. In particular, we have shown that the photo-generated carrier drift and diffusion in the microcell quasi neutral layers can be treated like an effective re-sizing of the microcell depletion layer boundaries, therefore increasing the effective photon collection region. The model was

applied to analyze the response of three p-on-n SiPMs and can naturally be extended to any SiPM, including n-on-p devices. In particular, it shows like a low and wide electric field in the junction is crucial to achieve a faster saturation of the electron probability and a higher ionization efficiency. This aspect will be the key to optimize the electric field in the next generation of SiPMs.

Chapter 6

Nuisance Processes in p-on-n SiPMs

6.1 Introduction

In the previous chapter of this thesis we presented a new model to describe the SiPM Photon Detection Efficiency (PDE) as function of the reverse bias voltage and wavelength. To develop new generation of SiPMs, it is not only crucial to have a better understanding of their avalanche triggering probabilities (Chapter 5), but it is also important to reduce significantly their nuisance processes named: dark noise, after pulse and CrossTalk. In this chapter we will introduce a new theoretical framework based on the model introduced in Chapter 5, that allows to explain the voltage and temperature dependence of all the nuisance processes in SiPM. The new model has been successfully applied to characterize two p-on-n SiPMs: an Hamamatsu VUV4 Multi-Pixel Photon Counter (MPPC), already studied in Chapter 3, and one Fondazione-Bruno-Kessler (FBK) SiPM (FBK VUV HD 1 (LF)), and it can be extended to other SiPMs, including n-on-p devices.

6.2 Nuisance Processes in SiPM

Dark and correlated avalanche noise are among the crucial parameters that characterize SiPMs. Dark Noise (DN) pulses are charge signals generated by the

formation of electron-hole pairs due to thermionic or field enhanced processes, as introduced in Chapter 1. The dark current produced by a p-n junction under reverse bias can be considered, as first approximation, due to three independent mechanisms: (i) Shockley-Read-Hall recombination via traps, (ii) diffusion, (iii) band to band tunneling. The total current is then given by the sum of each of these mechanisms increased by avalanche multiplication. Different models are available in literature to study p-n junction under reverse bias up to the breakdown voltage [62, 140, 141], but no models are available to explain the relationship between the source of the current (the three independent mechanisms listed above) and the pulse rate measured when a Geiger mode device is biased above the breakdown voltage. The complication arises from the fact the probability a cell is discharged i.e. a pulse is produced, depends on the avalanche triggering probability that is a function of the position in which the e-h pair is originally created in the p-n junction depleted region. A model to explain the Geiger mode DN pulse rate, as a function of the applied over voltage, is presented in Sec. 6.3. Additionally, in the same section, we will also show how to infer the Silicon bandgap from dark noise data.

Geiger mode devices don't only suffer from dark noise, but also from Correlated Avalanches (CA). As introduced in Chapter 1, CAs are due to at least two mechanisms: the production of secondary photons during the avalanche in the gain amplification stage detected in nearby cells, and the trapping and subsequent release of charge carriers produced in avalanches. The latter process is usually referred to as afterpulsing, while the former is usually called CrossTalk. CrossTalk photons produce nearly simultaneous avalanches to the primary one (Direct CrossTalk (DiCT)) or delayed by several ns (Delayed CrossTalk (DeCT)) [64]. In general, the subset of the CAs constituted by afterpulses and delayed CrossTalk events is named Correlated Delayed Avalanches (CDAs). The probability a cell is discharged and therefore creates a CDA depends, for both mechanisms, on the avalanche triggering probability that is a function of the position where the carrier is originally produced in the depleted region (for after pulsing events) or where the photon is absorbed (for CrossTalk events). A detailed explanation of the voltage dependence of these nuisance processes in SiPMs will be presented in Sec. 6.4.

6.3 A model to explain the SiPM Dark Noise Rate

The first step to develop a model to explain the voltage and temperature dependence of the SiPM Dark Noise (DN) rate consists in introducing the three mechanisms that are responsible for its formation: diffusion, Shockley-Read-Hall recombination via traps and band to band tunneling. Fig. 6.1 represents a visualization of a symmetric p-on-n junction under reverse bias. The notation used in this chapter is the same introduced in Chapter 5. The depletion region starts at d_P (on the P^+ side)

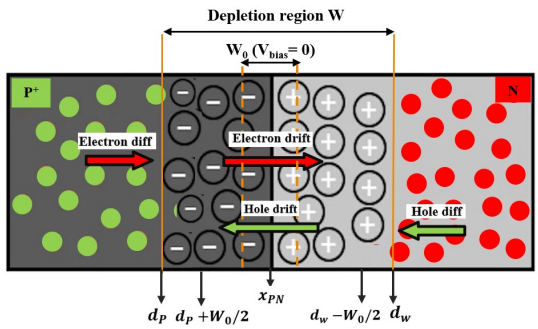

Figure 6.1: Model of the symmetric p-on-n junction used in this chapter.

and ends at d_W (on the N side), defining the total junction width of $W \equiv (d_W - d_P)$. W_0 represents the depleted region width at zero-bias. The electric field has a maximum at the p-on-n transition labeled as x_{PN}.

6.3.1 Diffusive contribution

The diffusive carrier rate can be derived using the ideal diode current density equation as [131]

$$R_{\text{diff}} = \frac{J_s}{q_e}(e^{\frac{q_e V}{k_B T}} - 1) \tag{6.1}$$

where: J_s is the reverse saturation current density; k_B is the Boltzmann constant; T the temperature and q_e is the elementary electron charge. The reverse bias voltage V is taken to be negative. Using Eq. 6.1, and introducing a parameter $\beta \in [0,1]$[141], it is possible to derive the p-n junction electron and hole diffusive carrier rates as follows

$$R_{\text{n-diff}}(d_p) = \beta R_{\text{diff}} \tag{6.2}$$

$$R_{\text{p-diff}}(d_w) = (1-\beta)R_{\text{diff}} \tag{6.3}$$

where each contribution is computed at the respective junction boundary, accordingly to Fig. 6.1.

6.3.2 Band to Band Tunneling

Band to band tunneling describes transitions of electrons which tunnel directly from the valence band to the conduction band [62]. Its contribution to the total carrier rate can be accounted as a Dirac Delta function at the position of the maximum electric field x_{PN} as

$$R_{bbt}(x) = \frac{J_{bbt}}{q_e}\delta(x - x_{PN}) \tag{6.4}$$

J_{bbt} is defined as

$$J_{bbt} = c_{bbt} V \left[\frac{F_m}{F_0}\right]^{\frac{3}{2}} e^{-\frac{F_0}{F_m}} \tag{6.5}$$

where: F_m is the maximum electric field at $x = x_{PN}$; $\delta(x)$ is the Dirac delta function; F_0 is a constant which has a value of 1.9×10^7 V/cm at room temperature, and c_{bbt} is a fit parameter that is assumed to be temperature independent.

6.3.3 Recombination via traps

The recombination via traps carrier rate accounts for the rate at which electrons and holes are captured from the conduction or valence band, respectively. In particular, its contribution to the total carrier rate contains not only the conventional Shockley-Read-Hall mechanism, but also an additional term due to tunneling via traps. It can be written as [62]

$$R_{trap}(x) = (1 + \Gamma(x))R_{srh}(x) \tag{6.6}$$

where $\Gamma(x)$ is a field dependent quantity and it accounts for the effects of tunneling. It is given by

$$\Gamma(x) = 2\sqrt{3\pi}\frac{|F|}{F_\Gamma}\exp\left(\frac{F}{F_\Gamma}\right)^2 \tag{6.7}$$

where: F is the local electric field. F_Γ is a constant that depends on the effective carrier mass (m^*) [142] and temperature T as follows

$$F_\Gamma = \frac{\sqrt{24m^*(k_BT)^3}}{q_e\frac{h}{2\pi}} \tag{6.8}$$

$R_{srh}(x)$ is the Shockley-Read-Hall rate given by [131]

$$R_{srh}(x) = \frac{pn - n_{ie}^2}{\tau_p(n+n_1)+\tau_n(p+p_1)} \tag{6.9}$$

where: p and n are the hole and electron densities; τ_p and τ_n are their lifetimes; $n_1 \sim n_{ie}\exp(-(E_T-E_i)/k_BT)$ and $p_1 \sim n_{ie}\exp((E_T-E_i)/k_BT)$ where n_{ie} is the intrinsic carrier concentration given by [143]

$$n_{ie}^2 = N_cN_v\exp\left[\frac{-E_g}{k_BT}\right] \tag{6.10}$$

with E_g Silicon band gap and N_c and N_v effective densities of states in the conduction and valance band, respectively. E_T represents the trap energy in the band-gap and E_i is the intrinsic Fermi level. In reverse bias condition $n \sim p \sim 0$, therefore $R_{srh}(x)$ is almost constant within the depletion layer boundaries. If we assume to work with a symmetric junction approximation, $R_{srh}(x)$ can be assumed constant except within a distance of $W_0/2$ from the depletion layer boundaries [144], such that

$$R_{srh}(x) \sim \begin{cases} -c_{srh} & \text{if } x \in [d_P + \frac{W_0}{2}, d_W - \frac{W_0}{2}] \\ 0 & \text{otherwise} \end{cases} \tag{6.11}$$

where c_{srh} is derived from Eq. 6.9 and it is defined as[1]

$$c_{srh} \equiv \frac{n_{ie}}{2\tau_c\cosh[(E_T-E_i)/k_BT]} \tag{6.12}$$

The negative sign in Eq. 6.11 implies a negative recombination rate; hence a generation of electron–hole pairs within the reverse-biased space charge region. If we

[1] In Eq. 6.12 we substituted the electron and hole lifetimes with a single lifetime τ_c such that $\tau_c \equiv (\tau_p = \tau_n)$.

assume mid-gap traps (i.e. $E_T = E_i$), Eq. 6.11 becomes

$$R_{srh} \sim -c_{srh} \propto -e^{-\frac{E_g}{2k_B T}} \tag{6.13}$$

This dependence of the Shockley-Read-Hall rate will be tested in Sec. 6.3.7. Using Eq. 6.11, Eq. 6.6 becomes

$$R_{trap}(x) \sim \begin{cases} -(1+\Gamma(x))c_{srh} & \text{if } x \in [d_P + \frac{W_0}{2}, d_W - \frac{W_0}{2}] \\ 0 & \text{otherwise} \end{cases} \tag{6.14}$$

6.3.4 SiPM Dark Noise Rate

The SiPM dark noise rate (R_{DN}), when the device is reverse biased above the breakdown voltage, can be obtained summing the thee independent carrier rates introduced in the previous sections and weighting them for the corresponding avalanche triggering probability. More precisely, in Chapter 5 we showed how it is possible to associate to each carrier (electron or hole) a finite probability of triggering an avalanche depending on the SiPM reverse bias voltage V and on the position x in which the carrier enters or is generated in the depletion layer i.e. $\mathrm{P}_e(x, |V|)$ or $\mathrm{P}_h(x, |V|)$ [120].

The contribution to the total dark noise pulse rate due to the diffusive carrier rates can then be obtained weighting $R_{\text{n-diff}}(d_p)$ and $R_{\text{p-diff}}(d_w)$ with the corresponding boundary avalanche triggering probability i.e. $P_e(d_P, |V|)$ or $P_h(d_W, |V|)$, where $P_e(d_P, |V|)$ ($P_h(d_W, |V|)$) represents the probability an electron (hole) that enters in the depletion layer at $x = d_P$ ($x = d_W$) triggers an avalanche.

The contributions to the total dark noise pulse rate due instead to the recombination via traps and tunneling carrier rates (i.e. $R_{trap}(x)$ and $R_{bbt}(x)$) depend instead on the position where the electron-hole pair (for the recombination via traps rate) or the electron (for the band to band tunneling rate) is originally created in the depletion layer. The corresponding dark noise pulse rate is therefore obtained weighting each carrier rate for its avalanche triggering probability i.e. $P_P(x, |V|)$ or

$P_e(x,|V|)$, respectively. $P_P(x,|V|)$ was defined in Chapter 5 as [59]

$$P_P(x,|V|) \equiv \Big(\mathrm{P}_e(x,|V|) + \mathrm{P}_h(x,|V|) - \mathrm{P}_e(x,|V|) \cdot \mathrm{P}_h(x,|V|)\Big)$$

It represents the probability an electron-hole pair, generated at the position x in the depleted region, triggers an avalanche within a p-n junction reverse biased at a voltage V[2]. The SiPM dark noise pulse rate after breakdown can be written summing the three pulse rates contributions just introduced as follows

$$R_{DN} = \int_{d_P}^{d_W} R_{trap}(x) P_P(x)\, dx + R_{bbt}(x) P_e(x_{PN}) + R_{\text{n-diff}} P_e(d_P) + R_{\text{p-diff}} P_h(d_W) \tag{6.15}$$

where the first integral extends up to the depletion layer boundaries, and the band-to-band tunneling term is accounted as a Dirac Delta function at the position of the maximum electric field (x_{PN}, Sec. 6.3.2). The diffusive contributions are negligible if compared with the generation and band to band tunneling term in Silicon [131], especially under reverse bias condition, therefore the third and fourth terms in Eq. 6.15 can be safely neglected. The latest generation of SiPMs also strongly reduced the band to band contribution to the total dark noise rate whose nature can now be probed only at cryogenic temperatures [145]. In the range of temperatures analysed in Sec. 6.3.7, this term results in fact still subdominant respect to the generation via traps term therefore in what follows it will also be neglected.

Eq. 6.15 can be additionally simplified with the model introduced in Chapter 5. In this way $P_P(x)$ can be written as

$$P_P(x) \sim \begin{cases} \mathrm{P}_e(d_P) & \text{if } x \in [d_P, x_{PN}] \\ \mathrm{P}_h(d_W) & \text{if } x \in [x_{PN}, d_W] \end{cases}$$

Eq. 6.15 therefore reduces to

$$R_{DN} \sim P_e(d_P) \int_{d_P}^{x_{PN}} R_{trap}(x)\, dx + P_h(d_W) \int_{x_{PN}}^{d_W} R_{trap}(x)\, dx \tag{6.16}$$

[2] From here on to keep the notation simple, we will drop the voltage dependence of the avalanche triggering probability, in agreement with the notation used in Chapter 5.

The first integral in Eq. 6.16 can be computed using Eq. 6.14. In this way this term reduces to

$$\begin{aligned}\int_{d_P}^{x_{PN}} R_{trap}(x)\,dx &= -\int_{d_P+\frac{W_0}{2}}^{x_{PN}} (1+\Gamma(x))c_{srh}\,dx = \\ &= -c_{srh}\Big(f_{DN}(W-W_0)\Big) - c_{srh}\int_{d_P+\frac{W_0}{2}}^{x_{PN}} \Gamma(x)\,dx\end{aligned} \tag{6.17}$$

where

$$\Big(x_{PN} - (d_P + \frac{W_0}{2})\Big) \equiv \Big(f_{DN}(W-W_0)\Big) \tag{6.18}$$

with $f_{DN} \in [0,1]$. In the same way the second integral in Eq. 6.16 follows as

$$\begin{aligned}\int_{x_{PN}}^{d_W} R_{trap}(x)\,dx &= -\int_{x_{PN}}^{d_W-\frac{W_0}{2}} (1+\Gamma(x))c_{srh}\,dx = \\ &= -c_{srh}\Big((1-f_{DN})(W-W_0)\Big) - c_{srh}\int_{x_{PN}}^{d_W-\frac{W_0}{2}} \Gamma(x)\,dx\end{aligned} \tag{6.19}$$

where

$$\Big((d_W - \frac{W_0}{2}) - x_{PN}\Big) \equiv \Big((1-f_{DN})(W-W_0)\Big) \tag{6.20}$$

Eq. 6.16 then becomes

$$\begin{aligned}R_{DN} = \Bigg\{ &-c_{srh}P_e(d_P)\left[\Big(f_{DN}(W-W_0)\Big) + \int_{d_P+\frac{W_0}{2}}^{x_{PN}} \Gamma(x)\,dx\right] + \\ &-c_{srh}P_h(d_W)\left[\Big((1-f_{DN})(W-W_0)\Big) + \int_{x_{PN}}^{d_W-\frac{W_0}{2}} \Gamma(x)\,dx\right]\Bigg\}\end{aligned} \tag{6.21}$$

The term multiplied by $P_e(d_P)$ ($P_h(d_W)$) in Eq. 6.21 represents the contribution to the total dark noise rate due to avalanches initialised by an electron (hole). Electrons or holes avalanches therefore give to the total dark noise rate two contributions due to: (i) Shockley-Read-Hall thermal-only recombination; (ii) Shockley-Read-Hall thermal-trap assisted recombination.

6.3.5 Evaluation of the field enhanced recombination integral

To obtain a practical expression for R_{DN}, in what follows we will assume to work with a symmetric step junction for the extraction of the electric field: $(N_a = N_d) \equiv N$ where N_a and N_d are the acceptor and donor concentration of the p-n-junction, respectively. In other words, we will approximate the real junction electric field with the one obtained symmetrizing the junction i.e. substituting its electric field with the symmetric one obtained from a junction with same width W. The electric field in the junction can then be written as

$$F(x) = F_m\Big(1 - 2\frac{|x - x_{PN}|}{W}\Big) \tag{6.22}$$

where F_m is the module of the maximum electric field at $x = x_{PN}$. The first integral in Eq. 6.21 then becomes

$$\begin{aligned}
&\int_{d_P+\frac{W_0}{2}}^{x_{PN}} \Gamma(x)\, dx = \\
&= \frac{\sqrt{3\pi}WF_\Gamma}{2|F_m|}\Big[\exp\Big(\frac{F}{F_\Gamma}\Big)^2\Big]_{d_P+\frac{W_0}{2}}^{x_{PN}} = \\
&= \frac{\sqrt{3\pi}WF_\Gamma}{2|F_m|}\Big[\exp\Big(\frac{F_m}{F_\Gamma}\Big)^2 - \exp\Big(\frac{F_m}{F_\Gamma}\Big(1 - \frac{2}{W}f_{DN}(W - W_0)\Big)\Big)^2\Big]
\end{aligned} \tag{6.23}$$

and the second integral in Eq. 6.21 becomes

$$\begin{aligned}
&\int_{x_{PN}}^{d_W-\frac{W_0}{2}} \Gamma(x)\, dx = \\
&= -\frac{\sqrt{3\pi}WF_\Gamma}{2|F_m|}\Big[\exp\Big(\frac{F}{F_\Gamma}\Big)^2\Big]_{x_{PN}}^{d_W-\frac{W_0}{2}} = \\
&= -\frac{\sqrt{3\pi}WF_\Gamma}{2|F_m|}\Big[-\exp\Big(\frac{F_m}{F_\Gamma}\Big)^2 + \exp\Big(\frac{F_m}{F_\Gamma}\Big(1 - \frac{2}{W}(1 - f_{DN})(W - W_0)\Big)\Big)^2\Big]
\end{aligned} \tag{6.24}$$

6.3.6 Fitting equation for the dark noise rate

Using Eq. 6.23 and Eq. 6.24, Eq. 6.21 becomes

$$R_{DN} = \Bigg\{ -c_{srh}P_e(d_P)\Bigg[\Big(f_{DN}(W-W_0)\Big) + \frac{\sqrt{3\pi}WF_\Gamma}{2|F_m|}\Big[\exp\Big(\frac{F_m}{F_\Gamma}\Big)^2 - \exp\Big(\frac{F_m}{F_\Gamma}\Big(1-\frac{2}{W}f_{DN}(W-W_0)\Big)\Big)^2\Big]\Bigg] +$$
$$-c_{srh}P_h(d_W)\Bigg[\Big((1-f_{DN})(W-W_0)\Big) +$$
$$+\frac{\sqrt{3\pi}WF_\Gamma}{2|F_m|}\Big[\exp\Big(\frac{F_m}{F_\Gamma}\Big)^2 - \exp\Big(\frac{F_m}{F_\Gamma}\Big(1-\frac{2}{W}(1-f_{DN})(W-W_0)\Big)\Big)^2\Big]\Bigg]\Bigg\} \tag{6.25}$$

6.3.6.1 Analysis of dependencies of Eq. 6.25

Despite the complexity, Eq. 6.25 can be simplified and reduced to only three independent parameters using the symmetric junction approximation introduced in Sec. 6.3.5 for the electric field. The avalanche triggering probabilities $P_e(d_P)$ and $P_h(d_W)$ are in fact assumed known and fixed since they can be derived with the method introduced in Chapter 5. F_Γ is a constant. f_{DN} represents the fraction of the junction width in which avalanches are initialized by an electron. It is a fit parameter and, by definition, it is constrained to be $f_{DN} \in [0,1]$. The other unknown quantities in Eq. 6.25 are: the Shockley-Read-Hall rate (c_{srh}), the maximum electric field (F_m) and the junction width (W). c_{srh} is a quantity that is voltage independent, but temperature dependent, while F_m and W are assumed to be temperature independent, but voltage dependent quantities. F_m and W are however not independent. The maximum electric field can in fact be written as [62]

$$F_m = F_{m0} \times (1 - \frac{V}{V_{int}})^{1-p} \tag{6.26}$$

where: F_{m0} is the maximum electric field at zero bias, V_{int} is the built-in potential and p a parameter that depends on the junction type. In Sec. 6.3.5 we assumed to work with a symmetric step junction, therefore $p = \frac{1}{2}$. The value of V_{int} doesn't have a strong influence on the model behaviour and it will be assumed equal to 0.7 V. F_{m0} can be extrapolated from the junction length at zero bias W_0, as fol-

lows [62]

$$F_{m0} \equiv \frac{V_{int}}{(1-p) \times W_0} \tag{6.27}$$

The total junction length $W \equiv (d_W - d_P)$ is then equal to

$$W = \sqrt{\frac{2\varepsilon_0 \varepsilon_r (V_{int} - V)}{q_e} \left[\frac{N_a + N_d}{N_a N_d}\right]} \tag{6.28}$$

where ε_0 and ε_r are the vacuum and relative Silicon dielectric constants. Assuming a symmetric step junction and defining W_0 as

$$W_0 \equiv \sqrt{\frac{4\varepsilon_0 \varepsilon_r V_{int}}{q_e N}} \tag{6.29}$$

W can be written as

$$W = W_0 \sqrt{1 - \frac{V}{V_{int}}} \tag{6.30}$$

Finally, $\left(W - W_0\right)$ in Eq. 6.25 can be written as

$$\left(W - W_0\right) = W_0 \left[\left(1 - \frac{V}{V_{int}}\right)^{\frac{1}{2}} - 1\right] \tag{6.31}$$

As summary, Eq. 6.25 can be reduced to three fitting parameters: the Shockley-Read-Hall rate (c_{srh}), the fraction of the junction width in which avalanches are initialized by an electron (f_{DN}), and the junction width at zero bias (W_0).

6.3.7 Comparison of analytical dark noise calculations with measurements

In this section we will apply the model just introduced to characterize the voltage and temperature dependence of the dark noise rate of two SiPMs: a Hamamatsu VUV4 MPPC (S/N: S13370-6152) and (ii) a FBK VUV HD 1 (FBK LF) SiPM. The dark noise data of the Hamamatsu VUV4 MPPC were presented in Chapter 3. We refer the reader to this chapter for a detailed description of the setup used for their measurements and for the data taking procedure. Additionally, for this study, we measured the temperature dependence of the dark noise rate

of a FBK VUV HD 1 SiPM using the same electronics and techniques presented in Chapter 3. For both devices (Hamamatsu VUV4 MPPC and FBK VUV HD 1 SiPM) the avalanche triggering probabilities in Eq. 6.25 were considered as fixed quantities since they were derived, in Chapter 5, for the same two devices at 233 K and at 213 K, respectively. Additionally, in what follows, we will treat the voltage dependencies of the avalanche triggering probabilities as temperature independent quantities. In this way, for example, the electron avalanche triggering probability for the Hamamatsu VUV4 MPPC at a temperature T ($P_e^T(d_P)$) could be derived from the one measured at 233 K ($P_e^{233\text{ K}}(d_p)$) by only applying a translation to the bias voltage (V) due to the difference between the breakdown voltage at the temperature T (V_{BD}^T) and the one at 233 K ($V_{BD}^{233\text{ K}}$), as follows

$$P_e^T(d_p, |V|) = P_e^{233\text{ K}}\Big(d_p; |V| + (|V|_{BD}^{233\text{ K}} - |V|_{BD}^T)\Big) \tag{6.32}$$

This approximation is justified due to the limited range of temperatures analysed for the two devices (70 K for Hamamatsu VUV4 MPPC and 50 K for the FBK VUV HD 1). The avalanche triggering probabilities in fact depend on the ionization coefficients in Silicon that are expected to have a weak variation in ~ 100 K as shown, for example, in [146]. The fits done with Eq. 6.25 for the Hamamatsu VUV4 MPPC dark noise data are reported in Fig. 6.2. The fit parameter c_{srh} is reported in Fig. 6.3. Note as the five data-set in Fig. 6.2 were fitted with a unique χ^2 minimization performed with MINUIT [79]. According to the discussion of Sec. 6.3.6.1, the parameters W_0 and f_{DN} are in fact in common for the different temperatures, since they are assumed to be temperature and voltage independent parameters. c_{srh} is instead a temperature dependent, but voltage independent parameter. In Fig. 6.3 we also tested the dependence of the parameter c_{srh} against the theoretical behaviour reported in Eq. 6.13. The temperature dependence of the Silicon band-gap in the fitting procedure was accounted as [147]:

$$\mathrm{E}_g(T) = E_g(0) - \frac{\alpha T^2}{T + \beta} \tag{6.33}$$

with $\alpha = 4.73 \times 10^{-4}\,\frac{\text{eV}}{\text{K}}$ and $\beta = 636$ K. At 0 K $E_g(0) = 1.166$ eV. The exponential behavior of Eq. 6.13 is well reproduced by the data. The fit gives a value of

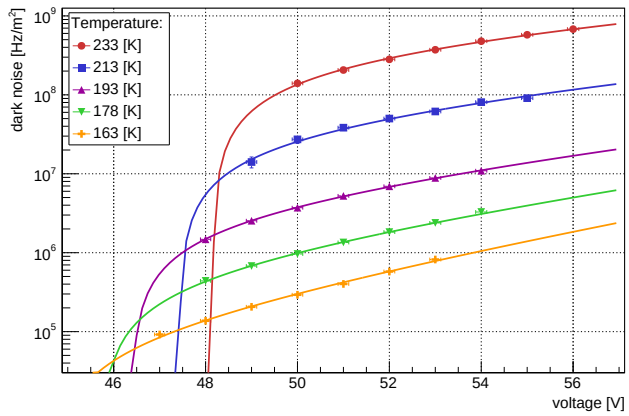

Figure 6.2: Dark Noise Rate as a function of the over voltage for different SiPM temperatures for the Hamamatsu VUV4 MPPC. The solid lines represent fits performed with Eq. 6.25.

$E_g(0) = (1.30 \pm 0.01)$ eV. This value is in slight tension if compared with the theoretical one. At the end of this section possible sources of systematic uncertainty that could affect the bandgap extraction will be listed. For the other two parameters

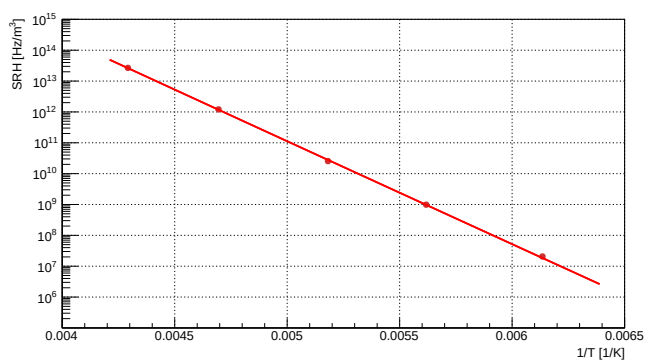

Figure 6.3: Shockley-Read-Hall recombination rate (c_{srh}) as a function of $1/T$ for the Hamamatsu VUV4 MPPC. The parameter c_{srh} was derived by the fits of the dark noise data using Eq. 6.25. The solid line represents a fit with Eq. 6.13.

$W_0 = (2.21 \pm 0.01) \times 10^{-7}$ m, while $f_{DN} = (1.7 \pm 0.2) \times 10^{-3}$. f_{DN} represents the

fraction of the junction width in which avalanches are initialized by an electron and since $f_{DN} \sim 0$ we can conclude that in p-on-n SiPMs DN avalanches are hole driven. A more in depth analysis of Eq. 6.25 also shows as the Shockley-Read-Hall thermal-only rate is subdominant if compared with the Shockley-Read-Hall trap-assisted rate, as also shown in Fig. 6.4. This is interesting since it shows

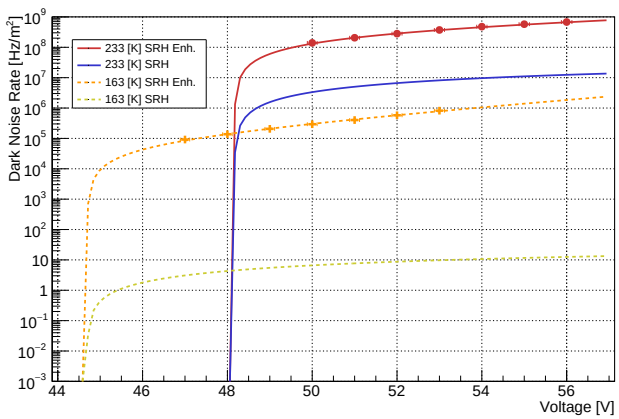

Figure 6.4: Shockley-Read-Hall thermal and trap-assisted (enhanced) rate as a function of the over voltage for the Hamamatsu VUV4 MPPC at 233 K and 163 K. The two contributions were derived from the fitting performed with Eq. 6.25.

as, in p-on-n SiPMs, avalanches are initialized by holes (that additionally have a lower probability to trigger an avalanche if compared with electrons [59]), and are due to Shockley-Read-Hall trap-assisted mechanisms. Eq. 6.25 therefore shows as suppressing the field in Geiger mode devices not only reduces the band to band tunneling contribution, here already negligible, but also the trap-assisted Shockley-Read-Hall contribution that drives the total dark noise rate in the current generation of SiPMs devices. Following the same procedure just introduced for the Hamamatsu VUV4 MPPC, the dark noise data of the FBK VUV HD 1 (FBK LF) and the corresponding fits are reported in Fig. 6.5. As the previous fit, f_{DN} converges to 0, while $W_0 = (2.3 \pm 0.2) \times 10^{-7}$ m. We can therefore conclude that also for the FBK VUV HD 1 the dark noise rate is given by avalanches initialized by holes and due to trap-assisted Shockley-Read-Hall recombination. The parameter c_{srh}

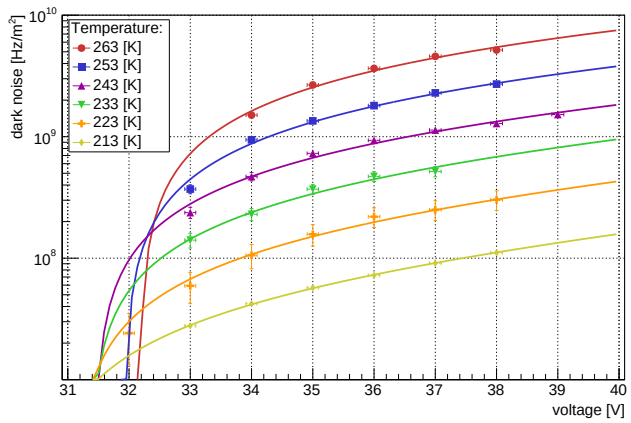

Figure 6.5: Dark Noise Rate as a function of the over voltage for different SiPM temperatures for the FBK VUV HD 1. The solid lines represent fits performed with Eq. 6.25.

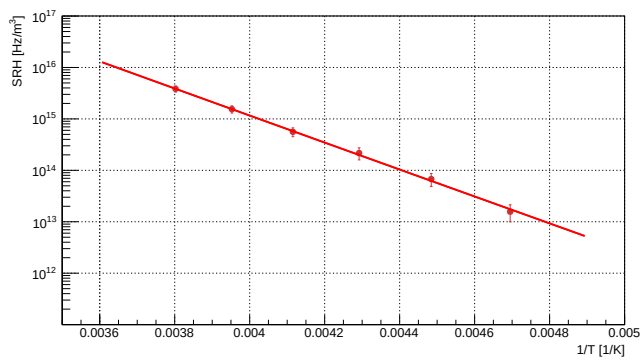

Figure 6.6: Shockley-Read-Hall recombination rate (c_{srh}) as a function of $1/T$ for the FBK VUV HD 1 SiPM. The parameter c_{srh} was derived by the fits of the dark noise data using Eq. 6.25. The solid line represents a fit with Eq. 6.13.

for these fits is reported in Fig. 6.6. The exponential behaviour also in this case is well reproduced. $E_g(0)$ converges to 1.01 ± 0.05 eV that is compatible in 3σ with the expected value. Table 6.1 summarises the common fit parameters derived for the two SiPMs tested in this section. In the table we additionally reported the $\chi^2 \setminus$ NDF (NDF is the Number of Degrees of Freedom) for the two global fittings.

Quantity	Hamamatsu VUV4 MPPC	FBK VUV HD 1 SiPM
f_{DN} [#]	$(1.7 \pm 0.2) \times 10^{-3}$	Compatible with 0
W_0 [m]	$(2.21 \pm 0.01) \times 10^{-7}$	$(2.3 \pm 0.2) \times 10^{-7}$
$E_g(0)$ [eV]	(1.30 ± 0.01)	1.01 ± 0.05
$\chi^2 \setminus$ NDF	0.83	1.02

Table 6.1: Summary of the parameters derived from the fitting of the dark noise data. Additionally, we reported the reduced χ^2 of the global fit with NDF Number of Degrees of Freedom.

The good $\chi^2 \setminus$ NDF shows as the model reproduces well the data. In each global fitting two sources of systematic errors were considered: (i) the error on the SiPM temperature, (ii) the error on the breakdown voltage. The sensors temperature was measured with 4 RTDs placed close to the position of the sensors and in good thermal contact with them (Chapter 3). The RTDs stability was found to be better than 0.05 K. Therefore the temperature was considered fixed in the global fitting routine of the dark noise data. However we cannot exclude a small shift between the average temperature measured by the 4 RTDs (used in the fitting) and the real sensor temperature. The absolute temperature was considered fixed also in the fitting of Fig. 6.6 and Fig. 6.3 used to extrapolate the silicon bandgap. The uncertainty in the absolute SiPM temperature could affect the Silicon bandgap determination since this quantity is extremely sensitive to the absolute values of the temperatures used in the fittings. Overall the temperature is not expected to be the biggest source of systematic uncertainty. The highest uncertainty comes in fact from the breakdown voltage extrapolation. This quantity is extrapolated, for each SiPM, from gain measurements and it is used to shift the zero of the probability (Eq. 6.32) at each temperature. For each translation we considered an error compatible with the statistical uncertainty of the breakdown voltage equal to 0.2 V. We therefore floated the quantity $(|V|_{BD}^{233\ \mathrm{K}} - |V|_{BD}^{T})$ in Eq. 6.32 considering tight boundaries of about 0.2 V around the shifted value due to this uncertainty.

6.4 A model to explain Correlated Avalanches in SiPMs

In the previous section we introduced a model to explain the voltage and temperature dependence of the SiPM Dark Noise rate. In this section we will show how the avalanche triggering probabilities introduced in Chapter 5 and used in the dark noise model can also be used to infer the voltage and temperature dependence of other two SiPMs nuisance processes: Direct CrossTalk and correlated delayed avalanche. More precisely, a model to explain the voltage dependence of the Direct CrossTalk is reported in Sec. 6.4.1, while a model to explain the voltage dependence of the number of correlated delayed avalanches is reported in Sec. 6.4.2. In what follows we will use the same notation introduced in Chapter 5 without introducing it explicitly. We refer therefore the reader to that chapter to have more details.

6.4.1 Direct CrossTalk model

For about half a century it has been known that avalanche processes in Silicon produce light usually called optical CrossTalk (CT). The photons emitted during an avalanche are in the infrared wavelength range [148, 149]. To suppress CT photons SiPMs incorporate trenches and other structures to surround each pixel that act as photon-stopper. It is however still extremely challenging to completely suppress the propagation of infrared light in Silicon due to the high attenuation length of these photons that can be several μm long [136]. DiCT (Direct CrossTalk) and

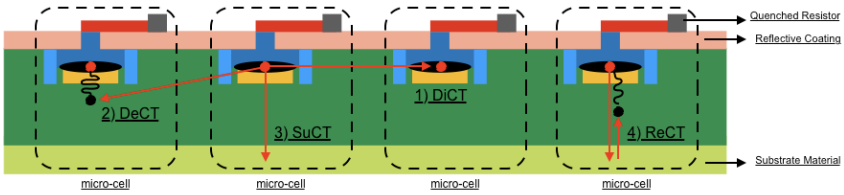

Figure 6.7: Different types of Optical CrossTalk in SiPM. The relative ratio between the different contributions is heavily dependent on the structure of the micro-cell. Overall four types of internal CrossTalk can be identified: Delayed CrossTalk (DeCT), Substrate CrossTalk (SuCT), Direct CrossTalk (DiCT) and Reflection CrossTalk (ReCT). See text for more details.

DeCT (Delayed CrossTalk) are the two mechanisms associated with the production of CT photons, see Fig. 6.7. DiCTs photons occur when photons generated during a triggered avalanche in one micro-cell promptly travel to the amplification region of neighboring micro-cells, where they induce a secondary avalanche. This mechanism happens over a pico-second time scale [64] and it mimics a multiple PE signal. DeCT photons occur instead when photons generated during a triggered avalanche travel deeper in the substrate. Some of them get lost in the substrate (Substrate CrossTalk), but some drift back to the avalanche region, due to the low-field in the Silicon bulk, where they can trigger a subsequent avalanche that can be delayed of several ns from the parent one. Additionally photons can also be reflected back (Reflection CrossTalk), as shown in [150, 151]. The voltage dependence of the number of photons detected by a SiPM as DiCT events i.e. prompt events, can be written as[3]

$$\mathrm{N_{DiCT}} = \chi_1 \times k \frac{C(V - V_{BD})}{q_e} \left[f_{CT} P_e(d_P) + (1 - f_{CT}) P_h(d_W) \right] \tag{6.34}$$

where: χ_1 is a voltage independent parameter that accounts for the probability a photon is detected in the active volume of a pixel (W^*, Chapter 5) in a time scale such that it appears as a prompt signal to the DAQ (miming therefore a multiple PE event)[4]. The quantity $\frac{C(V-V_{BD})}{q_e}$ represents the total number of carriers produced during an avalanche with C single SPAD capacitance and V_{BD} breakdown voltage. Eq. 6.34 therefore assumes as the number of photons produced in an avalanche is proportional (k) to the total number of carriers. The parameter k is assumed to be voltage independent and its temperature dependence is expected to be weak as shown by measurements of the optical CrossTalk at cryogenic temperatures [145]. The quantity in square brackets follows directly from Eq. 5.7 in Chapter 5 and

[3] Differently from Sec. 6.3.4, to simplify the discussion from now on the reverse bias voltage is taken to be positive.

[4] Note as the parameter χ_1 in Eq. 6.34, as well as the ratio between prompt and delayed CT pulses, strongly depends on the overall electronic used to discriminate multiple-PE events. A slow electronic with a high integration time will in fact tend to show higher multiple-PE events if compared with a fast electronics, like the one used for this work (described in Chapter 3), where it is possible to perform better pulse shape reconstruction. The parameter χ_1 in Eq. 6.34 therefore assumes as the division between prompt and delayed CT events is dependent only on the electronic and not on the SiPM voltage or temperature.

represents the probability a photon is absorbed in the electron or hole side of the avalanche region i.e. on the side in which the probability to trigger an avalanche is given by $P_e(d_P)$ or $P_h(d_W)$, respectively. f_{CT} represents therefore the fraction of DiCT events whose avalanche is initialized by an electron. It can be derived directly from f_e^* (Eq. 5.9) performing a Taylor expansion of the exponential. The attenuation length of infrared photons (μ) is in fact large enough compared to the effective photon collection region (W^*) such that

$$f_{CT} = f_e^*(\mu >> W^*) \equiv \left[\frac{1 - \exp\left(-\frac{(x_{PN} - d_{P^*})}{\mu}\right)}{1 - \exp\left(-\frac{W^*}{\mu}\right)} \right] \sim \frac{(x_{PN} - d_{P^*})}{W^*} \in [0,1]$$

The parameter f_{CT}, in agreement with the discussion of the SPAD capacitance reported in Chapter 5, is considered to be voltage and temperature independent. $(x_{PN} - d_{P^*})$ and W^* in fact increase slightly with voltage, due to the increase of the junction boundaries, but their ratio can be considered as a voltage independent quantity, as shown in [143].

The parameters χ_1 and k in Eq. 6.34 cannot be treated as independ parameters in the fitting procedure; therefore Eq. 6.34 will be written as

$$\mathrm{N_{DiCT}} = \eta_1 (V - V_{BD}) \Big[f_{CT} P_e(d_P) + (1 - f_{CT}) P_h(d_W) \Big] \tag{6.35}$$

where the pre-factor η_1 absorbs all the constants. Note as this equation treats as second order processes multi-reflection mechanisms i.e. photons produced in one cell that by reflection or other mechanisms reach n-additional neighbor cells before to trigger an avalanches with $n = 2, 3, \ldots$.

6.4.1.1 Comparison of analytical DiCT calculation with measurements

In this section we will apply the model just introduced to characterize the voltage and temperature dependence of the DiCT optical CrossTalk for the two SiPMs introduced in Sec. 6.3.7 and used for dark noise measurements. We refer the reader to that section for more details. The number of DiCT photons, in unit of Photo-electron Equivalent (PE), can be estimated with the method introduced in Sec. 3.3.4.3 and here summarized. More precisely, the charge distribution of the

prompt pulses obtained from dark data can be used to determine the mean number of Additional Prompt Avalanches (APA)s, N_{APA}, due to Direct CrossTalk as:

$$N_{APA} = \frac{1}{N}\sum_{i=1}^{N}\frac{A_i}{\overline{A}_{1\,PE}} - 1$$

where: A_i is the charge of the prompt pulse i, $\overline{A}_{1\,PE}$ is the average charge of 1 PE pulses and N is the number of prompt avalanches analyzed. N_{APA} is equal to the average number of DiCT photons produced per avalanche detected by the DAQ (N_{DiCT}, Eq. 6.35)[5]. The N_{APA} number in unit of PE, as a function of the over voltage and for different temperatures, is reported in Fig. 6.8 and Fig. 6.9 for the Hamamatsu VUV4 MPPC and for the FBK VUV HD 1 SiPM, respectively. The solid lines in each figure represent fits done with Eq. 6.35. As already introduced in Sec. 6.3.7 for the dark noise fitting, the avalanche triggering probabilities in Eq. 6.35 were considered as fixed quantities, since they were derived in Chapter 5 for the same two devices at 233 K and at 213 K, respectively. The temperature dependence of the avalanche triggering probabilities was accounted in the same way reported in Sec. 6.3.7. We therefore considered the voltage dependence of the avalanche triggering probabilities as a temperature independent quantity by applying a translation to the bias voltage V due to the change of the breakdown voltage with temperature, as shown for example in Eq. 6.32 for the Hamamatsu VUV4 MPPC. Additionally, for each SiPM, the five and six data-sets reported in Fig. 6.8 and Fig. 6.9 were fitted with a unique χ^2 minimization performed with MINUIT [79]. As introduced in fact in Sec. 6.4.1, the parameter f_{CT} is assumed to be a voltage and temperature independent parameter. Table 6.2 summarises the parameters derived from the fit and the ratio $\frac{x_{PN}-d_{P^*}}{W^*}$ extrapolated from

[5]Note as, in principle, it could be possible to have a cascade of DiCT photons due to different cell discharges that mimic multiple-PE signal in the DAQ. This process is not accounted in Eq. 6.35, that instead assumes that multiple-PE events are due to n photons produced by the discharge of the same cell. For example, a photon produced by the discharge of one cell triggers another cell, with a DiCT photon. In a ps time scale, the discharge of the second cell produces a DiCT photons that discharges a third cell. This cascade process gives overall a signal of charge equal to 3 PE that appears as prompt to the DAQ. Unfortunately, it is not possible with the current generation of SiPMs to do coincidence at the ps time scale to discriminate these types of events, therefore we will always assume that multiple-PE events that appear as prompt are due to n photons originated by the discharge of the original cell.

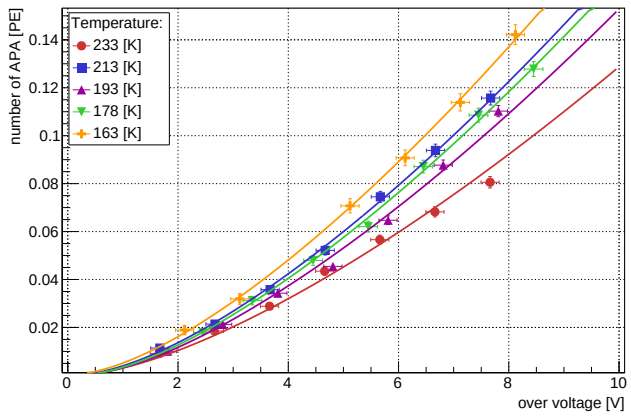

Figure 6.8: Mean number of Additional Prompt Avalanches (APA) due to direct CrossTalk as a function of the over voltage for different SiPM temperatures for the Hamamatsu VUV4 MPPC. The solid lines represent fits performed with Eq. 6.35.

Chapter 5 (Table 5.1 and Table 5.2), accordingly to the discussion of Sec. 6.4.1. The f_{CT} parameter of the Hamamatsu VUV4 MPPC agrees in less than 1σ with the one derived in Chapter 5. The f_{CT} parameter of the FBK VUV HD 1 is instead in slight tension with the one predicted by the data reported in Chapter 5. However, the quality of the fit (χ^2/NDF) does not worsen significantly while constraining this parameter to be equal to the one predicted in Chapter 5. The reason is to be searched in the highly asymmetric junction of the FBK VUV HD 1 that results in a small electron dominated thickness i.e. $(x_{PN} - d_{P^*})$, that gives a lower number of electron driven avalanches (for DiCT mechanisms) if compared with the Hamamatsu VUV4 MPPC. The value of the parameter η_1 reported in Table 6.2 is instead obtained averaging the η_1 parameter derived by the fits performed at each temperature. The small error in the values of η_1 shows as, independently of the device and temperature, each fit converges essentially to the same value. This validates the assumption done in the derivation of the DiCT model in Sec. 6.4.1, where we inferred a weak temperature dependence of this parameter due to the small temperature dependence of other DiCT measurements [145]. The good quality of the fitting is shown by the $\chi^2 \setminus$ NDF, reported in Table 6.2. The sources of systematic

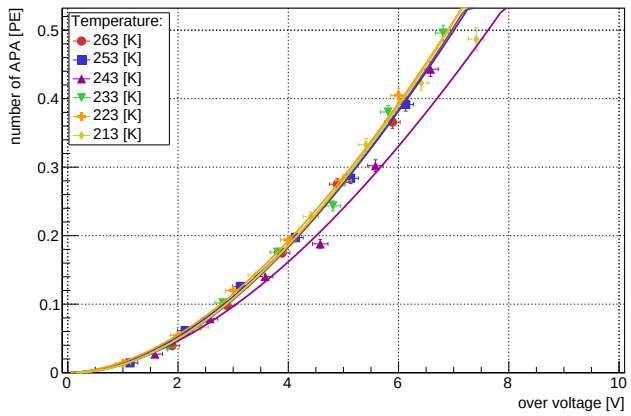

Figure 6.9: Mean number of Additional Prompt Avalanches (APA) due to direct CrossTalk as a function of the over voltage for different SiPM temperatures for the FBK VUV HD 1. The solid lines represent fits performed with Eq. 6.35.

errors for the DiCT measurements and for the fitting routine are compatible with the ones reported in Sec. 6.3.7 for the fitting of the dark noise data. We refer the reader to that section for more details.

Overall from this analysis, we can conclude that, since $f_{CT} \sim 0$ and η_1 is essentially temperature independent, DiCT mechanisms in p-on-n SiPMs have a weak temperature dependence and are initialized by holes. This last aspect agrees with the dark noise discussion reported in Sec. 6.3.7 where we noticed as also dark noise avalanches, in p-on-SiPMs, were initialised by holes.

6.4.2 Correlated Delayed Avalanche Model

Correlated Delayed Avalanches (CDA)s arise at least from two processes: afterpulses and delayed optical CrossTalk. A detailed explanation of the latter mechanism is introduced in Sec. 6.4.1. The former process is instead due to the large number of carriers present in Geiger-mode discharges [152]. Some of them can in fact remain trapped in metastable traps during the avalanche formation. Their subsequent release may produce additional pulses called afterpulses, which contribute to the observed signal. The time distribution between pulses can be used to

Quantity	Hamamatsu VUV4 MPPC	FBK VUV HD 1 SiPM
f_{CT} [#]	0.13 ± 0.02	0.009 ± 0.006
η_1 [V^{-1}]	0.039 ± 0.001	0.340 ± 0.006
$\frac{x_{PN}-d_{P^*}}{W^*}$ [#]	0.2 ± 0.1	0.065 ± 0.006
$\chi^2 \setminus$ NDF	1.6	1.9

Table 6.2: Parameters extracted from the fit of the DiCT data using Eq. 6.35 for the two SiPMs tested: Hamamatsu VUV4 MPPC and FBK VUV HD 1 SiPM. f_{CT} represents the fraction of avalanches initialized by an electron. η_1 is a parameter that accounts for several proportionality factors (see text for more details). $\frac{x_{PN}-d_{P^*}}{W^*}$ represents the ratio between the length of the region in which avalanches are initialized by an electron and the length of the effective photon collection region, defined in Chapter 5. Additionally, we reported the reduced χ^2 of the global fit with NDF Number of Degrees of Freedom.

discriminate the two types of events. An example is reported in Fig. 6.10 for the FBK VUV HD 1 SiPM. Trigger pulses[6] producing prompt CrossTalk are marked

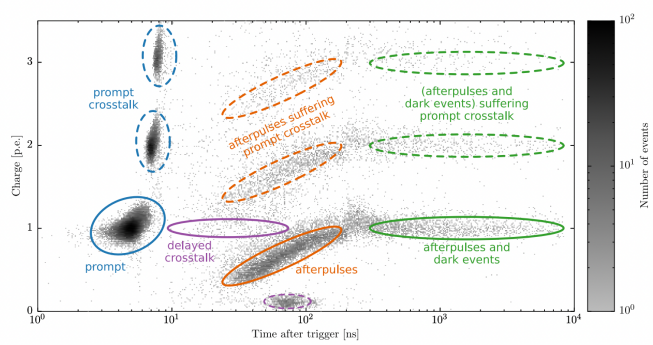

Figure 6.10: Distribution of FBK VUV HD 1 SiPM pulses as a function of the time after the microcell was triggered. See text for a detailed explanation [1].

with blue dashed circle and are measured as pulses with multiple PE amplitudes (Sec. 6.4.1). Avalanches due instead to delayed CrossTalk have amplitudes equal to 1 PE and are marked with a purple circle. Trigger pulses can also suffer from

[6]Trigger pulses are called prompt in Fig. 6.10.

afterpulses represented with an orange circle in Fig. 6.10. The amplitude of the afterpulse events depends on the SPAD recharging time. This last quantity can be estimated directly from Fig. 6.10 fitting the recovery curve of the 1 PE events as follows

$$A = A_{1\ \mathrm{PE}} \times \left(1 - e^{-\frac{t-t_0}{\tau_{\mathrm{SPAD}}}}\right) \tag{6.36}$$

where: $A_{1\ \mathrm{PE}}$ is charge of 1 PE pulses, τ_{SPAD} is microcell recharging time and $t = t_0$ is the time of the prompt pulse. Afterpulse events can also suffer of CrossTalk, but with a lower probability if compared with the trigger pulses, since the cell that produces the afterpulse event has a lower bias voltage due to its recharging time. The orange band structure in Fig. 6.10 is therefore repeated above the 1 PE (orange dashed circle) to represent this contribution. Pulses occurring with larger delay from the primary pulse can originate from either afterpulsing, thermal or field enhanced mechanisms (green circle). They can suffer of prompt CrossTalk and they are represented in Fig. 6.10 as green dashed circles. Pulses marked with a dashed purple circle represent instead pulses who do not get resolved by the DAQ. Fig. 6.10 is constructed requiring: (i) the charge of the trigger pulse to be a single PE equivalent, (ii) the time of the trigger pulse to be equal to the mean trigger time set by the DAQ pre and post-trigger acquisition settings. The first condition is necessary to avoid that multiple-PE events artificially increase the probabilities of the different SiPM nuisance processes, as shown in [85]. The voltage dependence of the number of CDAs due to afterpulses, as a function of the time difference t respect to their primary pulse can be written as

$$\begin{aligned} \mathrm{N}_{\mathrm{CDA}}(t) = & \frac{C(V - V_{BD})}{q_e} \times A_{\mathrm{SiPM}} k_1 \mathrm{N}_{\mathrm{traps}} W \times \frac{e^{-\frac{t}{\tau}}}{\tau} \times \\ & \times \left[f_{CDA} P_e(d_P, V - V_{eff}(t)) + (1 - f_{CDA}) P_h(d_W, V - V_{eff}(t)) \right] \end{aligned} \tag{6.37}$$

where: $A_{\mathrm{SiPM}} k_1 \mathrm{N}_{\mathrm{traps}} W$ represents the trapping probability i.e. the probability a single carrier is trapped. This quantity is assumed to be proportional (k_1) to the trap density $\mathrm{N}_{\mathrm{traps}}$.[7] W represents the junction width, therefore $\mathrm{N}_{\mathrm{traps}} W$ represents

[7] For simplicity, in the text we assumed that each carrier trapped is also realised. This condition can be relaxed introducing an effective k_1 that accounts for the probability that not only a carrier is trapped, but also it is realised. k_1 is assumed to be a voltage independent parameter. It is however a

the total number of traps per m^2. This number has a voltage dependence, since W increases slightly with voltage. In what follows we will parameterize W as done in Sec. 6.3.6.1 such that

$$W = W_0\sqrt{1+\frac{V}{V_{int}}} \tag{6.38}$$

with W_0 junction length at zero bias and $V_{int} = 0.7$ V. V_{int} doesn't have a strong influence on the model behaviour, as already noticed in Sec. 6.3.6.1. A_{SiPM} is the SiPM active area. The quantity $\frac{e^{-\frac{t}{\tau}}}{\tau}$ accounts for the exponential decay of the number of afterpulse events with time i.e. the exponential realise of the trapped carriers with time [153]. τ represents an afterpulsing time constant often called afterpulsing lifetime and it depends on the temperature as shown, for example, in Chapter 3. The quantity inside the square brackets of Eq. 6.37 represents instead the probability a carrier produces a self sustained avalanche. More precisely, the first (second) term of the sum in Eq. 6.37 represents the probability a single carrier triggers an avalanche with probability $P_e(d_P, V - V_{eff}(t))$ ($P_h(d_W, V - V_{eff}(t))$). $f_{CDA} \in [0,1]$ represents the fraction of afterpulse events whose avalanche is initialized by an electron. The effective voltage $V_{eff}(t)$ in the avalanche triggering probabilities accounts for the reduced avalanche probability due to the cell recharging time: τ_{SPAD}, such that

$$V_{eff}(t) \equiv V - \left((V - V_{BD}) \times (1 - e^{-\frac{t}{\tau_{\text{SPAD}}}}) + V_{BD}\right) \tag{6.39}$$

with V bias voltage and t elapsed time from the primary pulse at which the trapped charge is realised. Practically, as it will be shown in Sec. 6.4.2.1, its effect is negligible in p-on-n SiPMs. Finally, the first term in Eq. 6.37: $\frac{C(V-V_{BD})}{q_e}$, represents the total number of carriers produced during an avalanche that depends on the SPAD capacitance C and breakdown voltage V_{BD}, as already introduced in Sec. 6.4.1. Some of the parameters in Eq. 6.37 cannot be treated as independent in the fitting

temperature dependent parameter, since the trapping probability, like the trapping lifetime τ [152], depends on the SiPM temperature.

procedure, therefore Eq. 6.37 can be simplified as follows

$$\begin{aligned} \mathrm{N_{CDA}}(t) =& \eta_2 \times e^{-\frac{t}{\tau}}(V - V_{BD}) \times \sqrt{1 + \frac{V}{V_{int}}} \times \\ & \times \left[f_{CDA} P_e(d_P, V - V_{eff}(t)) + (1 - f_{CDA}) P_h(d_W, V - V_{eff}(t)) \right] \end{aligned} \tag{6.40}$$

where the parameter η_2 absorbs all the constant. This parameter is assumed to be voltage independent, but temperature dependent, since the trapping probability can be function of the temperature.

6.4.2.1 Comparison of analytical CDA calculation with measurements

In this section we will apply the model just introduced to characterize the voltage and temperature dependence of the number of correlated delayed avalanches for the two SiPMs used for the dark noise rate and DiCT measurements reported in Sec. 6.3.7 and Sec. 6.4.1.1, respectively. More precisely, dark noise and CDAs events can be distinguished by studying the time distribution of dark events relative to the primary pulse using the method introduced in Chapter 3 and in [85]. This technique requires the charge of the primary pulse to be a single PE equivalent and allows to compute the observed pulse rate $\mathrm{R}(t)$, as a function of the time difference t from the primary pulse ($t = 0$) as follows

$$\mathrm{R}(t) = \mathrm{R_{DN}}(t) + \mathrm{R_{CDA}}(t)$$

where $\mathrm{R_{DN}}$ is the rate of dark noise pulses and $\mathrm{R_{CDA}}$ is the rate of CDAs per pulse. An example of the measured time distribution for the Hamamatsu VUV4 MPPC at different over voltages, for a temperature of 233 K, is reported in Fig. 6.11. We refer the reader to Chapter 3 to have a detailed explanation of the construction of this figure. The DN rate can then be estimated from Fig. 6.11, performing a weighted mean of the asymptotic rates at long times i.e. between 10^3 and 10^4 ns for 233 K. The number of CDAs in a fixed time window of length Δt can be derived as

$$\mathrm{N_{CDA}}(\Delta t) = \int_0^{\Delta t} \Big(\mathrm{R}(t) - \mathrm{R_{DN}}(t) \Big) \, \mathrm{dt}$$

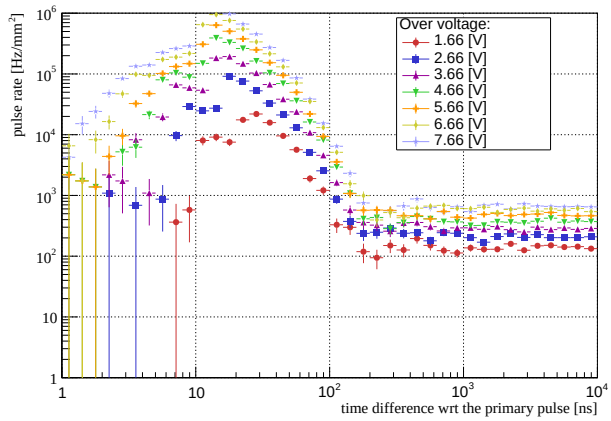

Figure 6.11: Observed pulse rate $\mathrm{R}(t)$ of the Hamamatsu VUV4 MPPC as a function of the time difference with respect to (wrt) the primary pulse for a temperature of 233 K.

where $\mathrm{R_{DN}}$ is the DN rate. Each pulse rate in Fig. 6.11 can then be integrated to obtain the number of CDAs per pulse as a function of the over voltage and time difference respect to its primary pulse. More precisely, the number of CDAs at a given time t_i respect to the primary pulse can be obtained integrating the rate (R_i) at the time t_i for a length equal to the corresponding bin width (Δt_i) as follows

$$\mathrm{N_{CDA}}(t_i) = \left(\mathrm{R}_i - \mathrm{R_{DN}}\right) \times \Delta t_i \tag{6.41}$$

The number of CDAs for different times t_i for the Hamamatsu VUV4 MPPC is presented in Fig. 6.12 as a function of the applied over voltage. The data-sets were fitted together with a unique χ^2 minimization performed with MINUIT to test the theoretical behaviour predicted by Eq. 6.40. According to the discussion of Sec. 6.4.2, τ, η_2 and f_{CDA} are in fact voltage independent parameters. The first dataset reported in Fig. 6.12 corresponds to 28.4 ns. Before this time, as shown in Fig. 6.11, the rate distribution at 233 K suffers from a combination of pulse reconstruction inefficiency and afterpulses too small to get resolved by the DAQ from their primary pulse (Chapter 3). After 112.9 ns, the rate distribution is instead dominated by dark noise events and the afterpulse rate is hidden from this

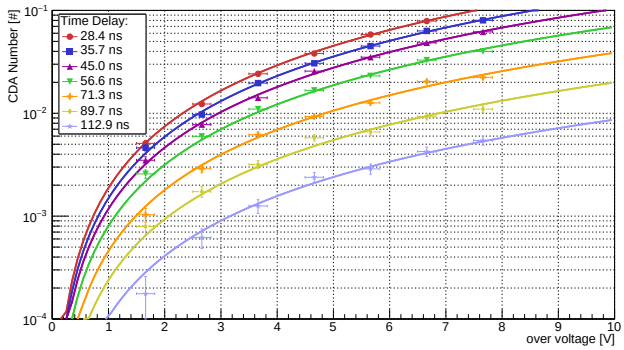

Figure 6.12: Number of Correlated Delayed Avalanches (CDA) per primary pulse (derived from Fig. 6.11) for the Hamamatsu VUV4 MPPC as a function of the over voltage. The number of CDAs was plotted for different times t_i with respect to (wrt) the primary pulse at a temperature of 233 K.

other nuisance process. The fits in Fig. 6.12 result in an afterpulsing time constant τ for the Hamamatsu VUV4 at 233 K of 24 ± 2 ns. In the fitting procedure τ_{SPAD} was fixed to 35 ns. The cell recovery time was in fact derived from the charge vs time to next pulse plot, as shown in Sec. 6.4.2. The η_2 parameter, common to all the fits, was found to be $(0.0301 \pm 0.0003)\ \mathrm{V}^{-1}$. The f_{CDA} fit parameter instead converges to 0. This fact is crucial, since it shows as after pulse events in p-on-n SiPMs, like Dark Noise and DiCT events, are hole driven processes. The f_{CDA} parameter was found to be compatible with 0 not only at 233 K, but also at the other temperatures tested for this study. Due to this experimental fact, the translation of the bias voltage due to cell recharging time i.e. $V - V_{eff}(t)$ in Eq. 6.40 has a negligible effect, since to hole probability saturates slowly if compared with the electron one, as shown in Chapter 5. From this follows that in p-on-n SiPM afterpulse events at different times respect to their primary pulses can be combined and fitted together without the need to discriminate them from a timing prospective. More precisely, the total number of CDAs ($\mathrm{N_{CDA}}$) in a window of length Δt can be

fitted as follows

$$\mathrm{N_{CDA}} \sim \sum_i \mathrm{N_{CDA}}(t_i) =$$
$$= \eta_2 \times (V - V_{BD}) \times \sqrt{1 + \frac{V}{V_{int}}} \times \left[f_{CDA} P_e(d_P) + (1 - f_{CDA}) P_h(d_W) \right] \tag{6.42}$$

where we dropped the V_{eff} dependence in the avalanche triggering probabilities. Fig. 6.13 reports the total number of correlated delayed avalanches for the Hamamatsu VUV4 as a function of the applied over voltage, and for different temperatures. The $\mathrm{N_{CDA}}$ number was derived integrating the corresponding rate plot until its baseline, i.e. until the rate plot starts to be dominated by dark noise events, as shown in Fig. 6.11. The solid lines in Fig. 6.13 represent fits performed with Eq. 6.42. The f_{CDA} parameter was fitted as a common parameter for the five tem-

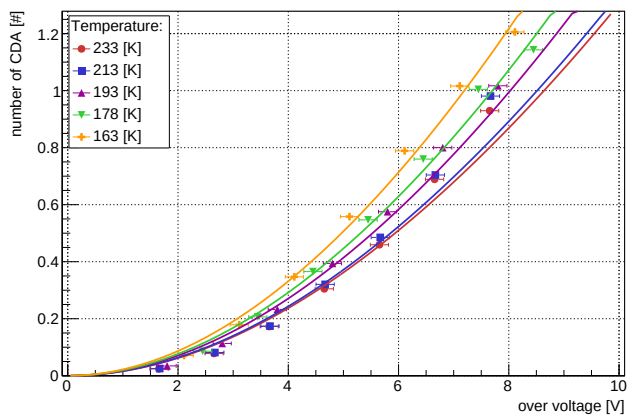

Figure 6.13: Total number of Correlated Delayed Avalanches (CDA) per primary pulse for the Hamamatsu VUV4 MPPC as a function of the over voltage, for different temperatures. Solid lines represent fits performed with Eq. 6.42.

peratures and it was found to be compatible with zero, as already anticipated at the beginning of this section. The reduced χ^2 of the fit was found to be bigger than 10. This last quantity is dominated by the disagreement of the fit with the data at the two higher temperatures, removing in fact these 2 datasets from the common

fitting routing gives a reduced χ^2 smaller than 3. The fit was therefore found to improve with decreasing temperature. This aspect is thought to be related to the increased afterpulse carrier lifetime with temperature. The efficiency of the pulse finding algorithm, used for the construction of the rate plot, increases with decreasing temperature, since afterpulses are realised, on average, at longer times respect to the trigger pulse and they can then carry a higher charge. It is therefore easier for the pulse-finding algorithm to identify correctly these pulses. Moreover, the lower dark noise rate at cryogenic temperatures allows to better discriminate afterpulses that otherwise would be hidden by the SiPM dark noise rate.

A similar analysis was also done for the FBK VUV HD 1 SiPM. Its pulse rate, at 233 K, for different over voltages is reported in 6.14. Fig. 6.15 instead reports

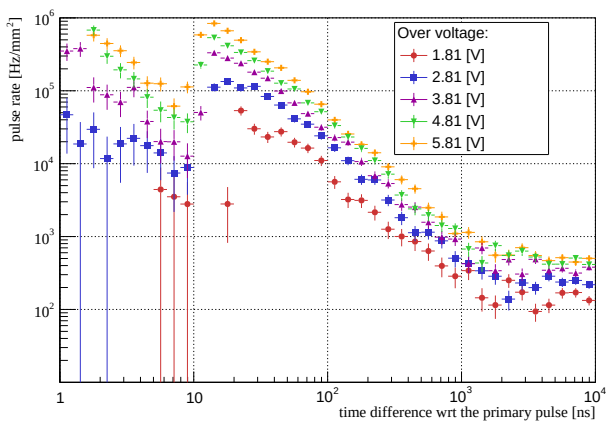

Figure 6.14: Observed pulse rate $R(t)$ of the FBK VUV HD 1 SiPM as a function of the time difference with respect to (wrt) the primary pulse for a temperature of 233 K.

the total number of correlated delayed avalanche for this SiPM as a function of over voltage and temperature with additionally the fit performed with Eq. 6.42. In agreement with the analysis of the Hamamatsu VUV4, also for the FBK VUV HD 1 the N_{CDA} number was derived integrating the corresponding rate plot until its baseline, i.e. until the rate plot starts to be dominated by dark noise events. For this device, f_{CDA} was found to be compatible with 0, as in the previous case, resulting therefore in hole driven afterpulses also for this p-on-n SiPM. The reduced χ^2 for these

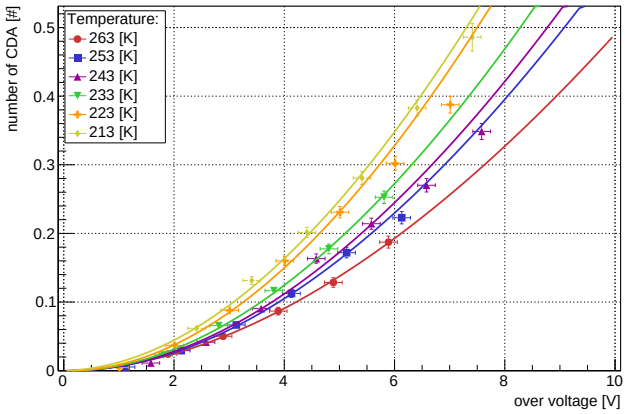

Figure 6.15: Total number of Correlated Delayed Avalanches (CDA) per primary pulse for the FBK VUV HD 1 SiPM as a function of the over voltage, for different temperatures. Solid lines represent fits performed with Eq. 6.42.

fits was found to be 2.35, resulting significantly improved respect to the one of the Hamamatsu VUV4 MPPC, particularly at higher temperatures. A possible explanation of this trend, not mentioned before, is the low probability of DeCT of this SiPM compared to the Hamamatsu VUV4 MPPC, as shown in Fig. 6.16. In this section we in fact implicitly assumed that the rate plot was completely dominated by afterpulse events. This is, on average, the case since this plot is constructed only accounting on the time differences between pulses and not on their different charges. For example an event with higher integrated charge (i.e. a DiCT from an afterpulse event) would be accounted in the rate plot as a single entry at a certain time t respect to the primary pulse neglecting its higher integrated charge. The rate plot therefore accounts for the effective pulse rate after the trigger pulse i.e. the afterpulse rate, without considering additional nuisance processes that could be related to it. This assumption may become weaker for SiPMs with a significant contribution of DeCT events in their CDA rate because DeCT and afterpulse events are uncorrelated between each other and they both contribute to the rate plot. This is not the case for the FBK VUV HD 1, as shown in Fig. 6.16, for which the amount of DeCT is negligible respect to the afterpulse rate. The Hamamatsu VUV4 MPPC

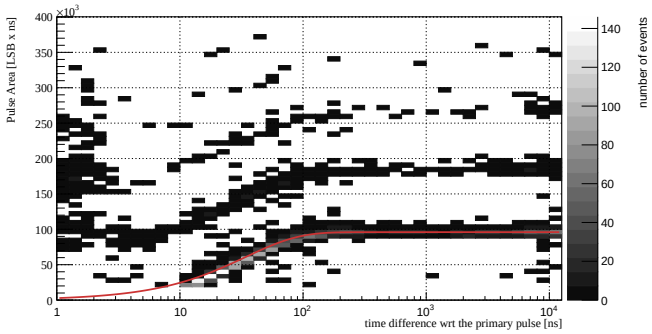

Figure 6.16: FBK VUV HD 1 charge distribution of first pulses following single PE trigger pulses as a function of the time difference with respect to (wrt) their primary pulse for 233 K and for an over voltage of 4.81 ± 0.13 V. The grey scale represents the number of events in each bin on a logarithmic scale. The solid red line shows a fit of the afterpulsing events and is used to measure the recovery time of one cell, equal to 35 ± 5 ns.

instead, as shown in Fig. 3.6 of Chapter 3, has a component of DeCT that affects the time distribution at short times after the trigger pulse, i.e. < 100 ns. This can explain the lower quality of the fits of the Hamamatsu VUV4, if compared with the ones of the FBK VUV HD 1, since Eq. 6.42 was derived assuming to work with afterpulse-only events. In principle DeCT events after the trigger pulse could be removed by a careful selection based on the pulse charges before to construct the corresponding rate plot. DeCT events carry in fact 1 full PE charge, differently from afterpulse events. This discrimination however becomes less powerful if a DeCT event happens at a time t from the trigger pulse close to 2 or 3 times the single PE SPAD recovery time. In this case, not only DeCT events, but also afterpulse events carry essentially a full 1 PE charge, therefore the discrimination is not effective and could cut afterpulse events rather than true DeCT events. Overall, in addition to the sources of uncertainties just introduced for the CDA fittings, the two sources of systematic errors listed for the dark noise measurements, and reported in Sec. 6.3.7, apply also to these fittings. We refer the reader to that section for more details. Table 6.3 summarises the fit results of this section.

Quantity	Hamamatsu VUV4 MPPC	FBK VUV HD 1 SiPM
f_{CDA} [#]	Compatible with 0	Compatible with 0
$\chi^2 \setminus$ NDF	> 10	2.35

Table 6.3: Parameters extracted from the fit of the afterpulse data using Eq. 6.42 for the two SiPM tested: Hamamatsu VUV4 MPPC and FBK VUV HD 1 SiPM. f_{CDA} represents the fraction of after pulse events initialized by an electron. Additionally, we reported the reduced χ^2 of the global fits with NDF Number of Degrees of Freedom.

Quantity	Hamamatsu VUV4 MPPC	FBK VUV HD 1 SiPM
f_{DN} [#]	$(1.7 \pm 0.2) \times 10^{-3}$	Compatible with 0
f_{CT} [#]	0.13 ± 0.02	0.009 ± 0.006
f_{CDA} [#]	Compatible with 0	Compatible with 0
$\frac{x_{PN}-d_{P^*}}{W^*}$ [#]	0.2 ± 0.1	0.065 ± 0.006

Table 6.4: Summary of the f parameters derived in this chapter. Additionally, we also reported the value $\frac{x_{PN}-d_{P^*}}{W^*}$ derived in Chapter 5 for the two SiPMs. It represents the ratio between the length of the region in which avalanches are initialized by an electron and the length of the effective photon collection region.

6.5 Conclusions

In this chapter we have presented a new analytical framework to describe several nuisance processes in SiPM. The new models are based on the concept of the avalanche triggering probability, derived in Chapter 5, and they predict with a minimum set of floating parameters all the nuisance processes in SiPM named: direct CrossTalk, correlated delayed avalanches and dark noise rate. Table 6.4 summarises the f parameters derived in this chapter. In the three cases $f \sim 0$; therefore all the nuisance processes in p-on-n SiPM can be considered initialised by holes i.e. they have a voltage dependence that is compatible with the corresponding $P_h(d_W)$ probability derived in Chapter 5. This is probably a consequence of the higher absorption volume of holes compared to electron in p-on-n SiPMs since the doping of the P side is, on average, higher if compared with the one of the N

side. Additionally, we have shown how the source of the dark noise rate in Geiger mode devices cannot be completely reduced to thermal Shockley-Read-Hall rate, but it needs to account for a strong component of enhancement due to trap-assisted contributions. The three models were applied to analyze the response of two p-on-n SiPMs and they can naturally be extended to any SiPM, including n-on-p devices. Furthermore, they provide key insight into the electric field structure within SiPMs, which can explain the limitation of existing devices and can be used to optimize the performance of future SiPMs.

Chapter 7

Conclusions

Next-generation noble liquid Xe detectors are emerging as the most promising candidates for neutrinoless double beta decay search due to their scalability for very large target masses and potential for extremely low background operations.

Over the last years, the nEXO collaboration has designed a new tonne-scale ($0\nu\beta\beta$) decay experiment conceived to push the search to the next frontier. The nEXO detector is based on a Time Projection Chamber (TPC) filled with five tonnes of Liquid Xenon (LXe) (5109 Kg) enriched 90% at ^{136}Xe. A careful selection of the TPC material, with also the intrinsic capability to simultaneously detect signal and background, will be the primary strength of the nEXO detector. Its design is conservative and very few assumptions of material radio-purity were made beyond what was already experimentally demonstrated and measured with its precursor: the EXO-200 detector. Additionally, the nEXO experiment is designed to provide the best possible energy resolution for a LXe TPC with a final design goal of 1% energy resolution (σ/Q) for the $0\nu\beta\beta$ decay of ^{136}Xe (Q-value at 2458.07 ± 0.31 keV). In order to achieve this objective the nEXO TPC needs to read out with high efficiency both the charge clouds and the light produced by the LXe ionization and scintillation, respectively. nEXO plans to use VUV sensitive Silicon Photo-Multipliers (SiPMs) as photon-sensors for the detection of the 175 nm scintillation light of LXe.

SiPM technology represents an unprecedented attempt to create an ideal solid-state photon detector combining the low-light detection capabilities of the previous

device generations with all the benefits of a solid-state sensor. In contrast to the widely used Photomultiplier Tubes (PMTs), SiPMs are low-voltage powered, optimal for operation at cryogenic temperatures, and have low radioactivity levels with high gain stability ($\sim 10^6$) over the time in operational conditions. For these reasons, not only the nEXO experiment, but also other large-scale low-background cryogenic experiments, such as DarkSide-20k, are migrating to a SiPM-based light detection system. This work was focused on two aspects that are now under study by the nEXO collaboration: (i) Analysis of the characteristics of several SiPMs candidates for nEXO; (ii) Theoretical study of Geiger properties of SiPMs. More precisely, in Chapters 3 and 4 we studied two SiPMs as possible candidates light sensors for the nEXO experiment: the Hamamatsu VUV4 MPPC and the newest generation of FBK devices: the FBK VUV HD 3 SiPM. For each device various features such as: dark noise, gain, correlated avalanches and direct CrossTalk were measured, with new dedicated setups, at 163 K and compared against the nEXO requirements for the light detection subsystem. For the Hamamatsu VUV4 MPPC we also measured its Photon Detection Efficiency (PDE) at 175 nm. The PDE of the FBK VUV HD 3 SiPM could not be finalized in this work due to an ongoing study of the light beam profile in one of the new commissioned setup. As summary, both devices meet the nEXO Dark and Correlated Avalanche noise requirements at 163 K giving comparable performances. Additionally, the FBK VUV HD 3 device, with its triple doping technology, suppresses significantly the sensor after-pulsing probability allowing to increase the operational over-voltage of these devices of 1 V if compared with its previous generation (FBK VUV HD 1), while fulfilling the nEXO requirements. The results of the Hamamatsu VUV4 and FBK VUV HD 3 characterization were then used, at the end of Chapter 4, to estimate the nEXO energy resolution as a function of the SiPM over voltage including also the contribution of the charge channel. In [1] the nEXO collaboration in fact showed as the first generation of FBK devices (FBK VUV HD 1) satisfies the requirement on the nEXO energy resolution (1% energy resolution for the $0\nu\beta\beta$ decay of ^{136}Xe), but in a limited over voltage range (up to 3 V of over voltage). At the end of Chapter 4, using a 20% baseline value for the nEXO detector light collection efficiency, we have shown that, if the PDE of the FBK VUV HD 3 will be the same of its previous generation, it would allow to consider this device as an excellent candi-

date for the nEXO experiment, not only because it satisfies the 1% nEXO energy resolution requirement, but because it does that up to 4 V of over voltage. The choice of the FBK VUV HD 3 SiPM, if compared with its previous generation, would therefore be beneficial since it would result in a higher S/N for the overall light detection channel. The Hamamatsu VUV4 MPPC instead, due to it lower efficiency, marginally satisfies the energy resolution requirement considering a 20% baseline value for the nEXO detector light collection efficiency. This suggests that, with modest improvements in its efficiency, or with an overall higher baseline value for the light collection efficiency in the nEXO experiment, the Hamamatsu VUV4 MPPC could be considered as a possible alternative to FBK SiPMs.

The last two chapters of this thesis (Chapters 5 and 6) are part of a broader study that is not only limited to the nEXO experiment, but it looks forward the next generation of noble liquid detectors. The outcome of this study will be the development of a new Back Side Illuminated SiPM light sensor to dramatically improve energy and timing resolution of future noble liquid detectors, significantly enhancing their background rejection capabilities relative to the current generation of dark matter and double beta decay experiments. More precisely, the second part of this thesis explored from a theoretical prospective Geiger mode properties of SiPMs. The first step was the derivation of the model presented in Chapter 5. In this chapter in fact we introduced a physics motivated parameterization of the avalanche triggering probability that describes the PDE of a SiPM as a function of its reverse bias voltage, at different wavelengths. This parameterization was based on the fact that in p-on-n SiPMs the induced avalanches are electron-driven in the UltraViolet (UV) range, while they become increasingly hole-driven towards the infrared range. In particular, the model was able to predict the SiPM PDE as a function of the reverse bias voltage and wavelength, corresponding to attenuation lengths in silicon between a few nanometers and several tens of micrometers, specifically accounting for the transition from electron-driven avalanches (close to the surface), to hole-driven avalanches (deeper inside the silicon). Additionally we demonstrated as a low and wide electric field in the junction is crucial to achieve a faster saturation of the electron probability and therefore a higher ionization efficiency.

The framework introduced in Chapter 5 was then used in Chapter 6 to explain

not only the voltage dependence of the SiPM efficiency, but also the temperature dependence of the principal SiPM nuisance processes named: direct CrossTalk, correlated delayed avalanches and dark noise rate. In particular, in this chapter we showed how all the nuisance processes in p-on-n SiPM are initialised by holes, probably due to the higher absorption volume of holes compared to electrons in p-on-n SiPM. Additionally, we have shown how the source of the dark noise rate in Geiger mode devices can not only be reduced to Shockley-Read-Hall thermal recombination, but it has also a strong component of enhancement due to trap-assisted recombination.

The models presented in Chapters 5 and 6 were tested to analyze the response of two p-on-n SiPMs and they can naturally be extended to any SiPM, including n-on-p devices. Overall the last two chapters of this work show as SiPMs are an extremely promising technology that still needs a strong research and development work to improve its current weaknesses: high correlated avalanche noise and low photon detection efficiency for vacuum ultraviolet wavelengths. Next generation double beta decay and dark matter liquid based cryogenic experiments need in fact unprecedented light detection efficiency and excellent background discrimination strategies to succeed in their respective searches. This work wants therefore to show the great potential that this technology can still offer and why it is worth keep developing it for the experiments to come.

Bibliography

[1] nEXO collaboration, A. Jamil, and et al. VUV-Sensitive Silicon Photomultipliers for Xenon Scintillation Light Detection in nEXO. *IEEE Transactions on Nuclear Science*, 65(11):2823–2833, 2018. ISSN 0018-9499. doi:10.1109/TNS.2018.2875668. → pages xi, xiv, xx, 33, 34, 55, 56, 62, 64, 70, 71, 81, 83, 96, 97, 101, 119, 148, 161

[2] nEXO Collaboration, S. Al Kharusi, and et al. nEXO Pre-Conceptual Design Report. http://arxiv.org/abs/1805.11142, 2018. → pages xiii, xiv, 2, 8, 9, 11, 14, 15, 17, 19, 20, 23, 24, 27, 30, 31, 33, 40, 41, 43

[3] S. M. Bilenky and C. Giunti. Neutrinoless double-beta decay: A brief review. *Modern Physics Letters A*, 27(13):1–22, 2012. ISSN 02177323. doi:10.1142/S0217732312300157. → pages xiii, 6, 7, 12, 13, 14

[4] P. Vogel. Neutrinoless double beta decay. In *AIP Conference Proceedings*, volume 870, pages 124–131. AIP, 2006. doi:10.1063/1.2402604. → pages xiii, 8, 16

[5] M. Agostini and et al. Discovery probability of next-generation neutrinoless double-β decay experiments. *Physical Review D*, 96(5), 2017. ISSN 24700029. doi:10.1103/PhysRevD.96.053001. → pages xiii, 5, 6, 13, 15, 16, 17, 18

[6] Z. Li and et al. Simulation of charge readout with segmented tiles in nEXO. *Journal of Instrumentation*, 14(09):P09020–P09020, 2019. ISSN 1748-0221. doi:10.1088/1748-0221/14/09/P09020. → pages xiv, 25, 26

[7] M. Szydagis and et al. NEST: a comprehensive model for scintillation yield in liquid xenon. *Journal of Instrumentation*, 6(10):P10002–P10002, 2011. ISSN 1748-0221. doi:10.1088/1748-0221/6/10/P10002. → pages xiv, 19, 35

[8] G. Anton and et al. Measurement of the scintillation and ionization response of liquid xenon at MeV energies in the EXO-200 experiment. *Physical Review C*, 101(6):065501, 2020. ISSN 2469-9985. doi:10.1103/PhysRevC.101.065501. → pages xiv, 20, 35, 36, 41

[9] M. Redshaw and et al. Mass and Double-Beta-Decay Q-value of ^{136}Xe. *Physical Review Letters*, 98(5):053003, 2007. ISSN 0031-9007. doi:10.1103/PhysRevLett.98.053003. → pages 1, 24, 33, 36, 96

[10] nEXO collaboration, J. B. Albert, and et al. Sensitivity and discovery potential of the proposed nEXO experiment to neutrinoless double-β decay. *Physical Review C*, 97(6):065503, 2018. ISSN 2469-9985. doi:10.1103/PhysRevC.97.065503. → pages 1, 2, 43

[11] J. B. Albert and et al. Investigation of radioactivity-induced backgrounds in EXO-200. *Physical Review C - Nuclear Physics*, 92(1):1–10, 2015. ISSN 1089490X. doi:10.1103/PhysRevC.92.015503. → page 2

[12] M. Auger and et al. The EXO-200 detector, part I: detector design and construction. *Journal of Instrumentation*, 7(05):P05010–P05010, 2012. ISSN 1748-0221. doi:10.1088/1748-0221/7/05/P05010. → pages 2, 22

[13] E. Aprile and T. Doke. Liquid xenon detectors for particle physics and astrophysics. *Rev. Mod. Phys.*, 82:2053–2097, 2010. doi:10.1103/RevModPhys.82.2053. → pages 2, 19, 37

[14] A. Gando and et al. Search for Majorana Neutrinos Near the Inverted Mass Hierarchy Region with KamLAND-Zen. *Physical Review Letters*, 117(8): 1–6, 2016. ISSN 10797114. doi:10.1103/PhysRevLett.117.082503. → pages 2, 22

[15] J. B. Albert and et al. Search for Neutrinoless Double-Beta Decay with the Upgraded EXO-200 Detector. *Physical Review Letters*, 120(7):72701, 2018. ISSN 10797114. doi:10.1103/PhysRevLett.120.072701. → pages 2, 23

[16] L. Baudis and et al. Characterisation of Silicon Photomultipliers for liquid xenon detectors. *Journal of Instrumentation*, 13(10):P10022, 2018. ISSN 1748-0221. doi:10.1088/1748-0221/13/10/P10022. → pages 2, 28, 44

[17] I. Ostrovskiy and et al. Characterization of Silicon Photomultipliers for nEXO. *IEEE Transactions on Nuclear Science*, 62(4):1825–1836, 2015. ISSN 0018-9499. doi:10.1109/TNS.2015.2453932. → pages 3, 28

[18] DarkSide Collaboration, C. E. Aalseth, and et al. DarkSide-20k: A 20 tonne two-phase LAr TPC for direct dark matter detection at LNGS. *The European Physical Journal Plus*, 133(3):131, 2018. ISSN 2190-5444. doi:10.1140/epjp/i2018-11973-4. → pages 3, 28, 72

[19] K. Eguchi and et al. First results from kamland: Evidence for reactor antineutrino disappearance. *Phys. Rev. Lett.*, 90:021802, 2003. doi:10.1103/PhysRevLett.90.021802. → page 5

[20] B. Aharmim and et al. Combined analysis of all three phases of solar neutrino data from the Sudbury Neutrino Observatory. *Physical Review C*, 88(2):025501, 2013. ISSN 0556-2813. doi:10.1103/PhysRevC.88.025501.

[21] A. B. McDonald. Nobel lecture: The sudbury neutrino observatory: Observation of flavor change for solar neutrinos. *Rev. Mod. Phys.*, 88: 030502, 2016. doi:10.1103/RevModPhys.88.030502.

[22] T. Kajita. Nobel lecture: Discovery of atmospheric neutrino oscillations. *Rev. Mod. Phys.*, 88:030501, 2016. doi:10.1103/RevModPhys.88.030501. → page 5

[23] B. Kayser. Neutrino Physics. *CERN Yellow Reports: School Proceedings*, 2:177–218, 2005. ISSN 2519805X. doi:10.23730/CYRSP-2017-002.177. → page 5

[24] S. Hannestad. Neutrino physics from precision cosmology. *Progress in Particle and Nuclear Physics*, 65(2):185–208, 2010. ISSN 01466410. doi:10.1016/j.ppnp.2010.07.001. → page 7

[25] J. Alves and et al. Planck 2015 results. *Astronomy and Astrophysics*, 594, 2016. ISSN 14320746. doi:10.1051/0004-6361/201629543. → page 7

[26] R. Wendell and et al. Atmospheric neutrino oscillation analysis with subleading effects in Super-Kamiokande I, II, and III. *Physical Review D*, 81(9):092004, 2010. ISSN 1550-7998. doi:10.1103/PhysRevD.81.092004. → page 7

[27] A. Gando and et al. Constraints on θ_{13} from A Three-Flavor oscillation analysis of Reactor Antineutrinos at KamLAND. *Physical Review D*, 83 (5):052002, 2011. ISSN 1550-7998. doi:10.1103/PhysRevD.83.052002. → page 7

[28] O. M. Njoya. *Search for The Double Beta Decay Modes of 134 Xe with the First Year of Phase II Data from EXO-200 and Development of Laser-Driven In-Situ Electron Lifetime Monitoring for nEXO*. PhD thesis, Stony Brook University, 2018. → pages 8, 18, 21

[29] Murray Gell-Mann, Pierre Ramond, and Richard Slansky. COMPLEX SPINORS AND UNIFIED THEORIES. pages 266–272. 2010. doi:10.1142/9789812836854_0018. → page 9

[30] K. S. Babu and V. S. Mathur. Radiatively induced seesaw mechanism for neutrino masses. *Physical Review D*, 38(11):3550–3553, 1988. ISSN 0556-2821. doi:10.1103/PhysRevD.38.3550. → page 9

[31] R. N. Mohapatra and et al. Neutrino mass and spontaneous parity nonconservation. *Physical Review Letters*, 44(14):912–915, 1980. ISSN 00319007. doi:10.1103/PhysRevLett.44.912. → page 9

[32] M. K. Parida and et al. Singlet Fermion Assisted Dominant Seesaw with Lepton Flavor and Number Violations and Leptogenesis. *Advances in High Energy Physics*, 2017(10):1–24, 2017. ISSN 1687-7357. doi:10.1155/2017/4023493. → page 9

[33] H. Päs and W. Rodejohann. Neutrinoless double beta decay. *New Journal of Physics*, 17(11):115010, 2015. ISSN 1367-2630. doi:10.1088/1367-2630/17/11/115010. → page 9

[34] G. Benato. Effective Majorana mass and neutrinoless double beta decay. *The European Physical Journal C*, 75(11):563, 2015. ISSN 1434-6044. doi:10.1140/epjc/s10052-015-3802-1. → page 9

[35] J. Schechter and J. W. F. Valle. Neutrinoless double-β decay in SU(2)×U(1) theories. *Physical Review D*, 25(11):2951–2954, 1982. ISSN 0556-2821. doi:10.1103/PhysRevD.25.2951. → page 10

[36] E. J. Chun and et al. Probing leptogenesis. *International Journal of Modern Physics A*, 33(05n06):1842005, 2018. ISSN 0217-751X. doi:10.1142/S0217751X18420058. → pages 10, 11, 12

[37] W. Buchmüller and et al. LEPTOGENESIS AS THE ORIGIN OF MATTER. *Annual Review of Nuclear and Particle Science*, 55(1):311–355, 2005. ISSN 0163-8998. doi:10.1146/annurev.nucl.55.090704.151558. → page 10

[38] E. W. Kolb and M. S. Turner. *The early universe*. Frontiers in Physics. Westview Press, Boulder, CO, 1990. doi:10.1201/9780429492860. → page 10

[39] G. A. White. The sakharov conditions. In *A Pedagogical Introduction to Electroweak Baryogenesis*, 2053-2571, pages 2–1 to 2–2. Morgan Claypool Publishers, 2016. doi:10.1088/978-1-6817-4457-5ch2. → page 11

[40] G. R. Farrar and M. E. Shaposhnikov. Baryon asymmetry of the Universe in the standard model. *Physical Review D*, 50(2):774–818, 1994. ISSN 0556-2821. doi:10.1103/PhysRevD.50.774. → page 11

[41] S. Davidson and A. Ibarra. A lower bound on the right-handed neutrino mass from leptogenesis. *Physics Letters B*, 535(1-4):25–32, 2002. ISSN 03702693. doi:10.1016/S0370-2693(02)01735-5. → page 11

[42] E. Kh Akhmedov and et al. Baryogenesis via Neutrino Oscillations. *Physical Review Letters*, 81(7):1359–1362, 1998. ISSN 0031-9007. doi:10.1103/PhysRevLett.81.1359. → page 12

[43] DUNE Collaboration. Long-Baseline Neutrino Facility (LBNF) and Deep Underground Neutrino Experiment (DUNE) Conceptual Design Report Volume 2: The Physics Program for DUNE at LBNF. 2, 2015. → page 12

[44] C. Bauer and et al. Background-free search for neutrinoless double-β decay of ^{76}Ge with GERDA. *Nature*, 544(7648):47–52, 2017. ISSN 0028-0836. doi:10.1038/nature21717. → page 14

[45] G. Cowan and et al. Asymptotic formulae for likelihood-based tests of new physics. *European Physical Journal C*, 71(2), 2010. ISSN 14346052. doi:10.1140/epjc/s10052-011-1554-0. → page 17

[46] M. Schumann. Dual-phase liquid xenon detectors for dark matter searches. *Journal of Instrumentation*, 9(08):C08004–C08004, 2014. ISSN 1748-0221. doi:10.1088/1748-0221/9/08/C08004. → page 19

[47] K. Fujii and et al. High-accuracy measurement of the emission spectrum of liquid xenon in the vacuum ultraviolet region. *Nuclear Instruments and Methods in Physics Research Section A*, 795:293–297, 2015. ISSN 01689002. doi:10.1016/j.nima.2015.05.065. → pages 19, 27, 43, 62, 78, 87, 105

[48] E. Conti and et al. Correlated fluctuations between luminescence and ionization in liquid xenon. *Physical Review B*, 68(5):054201, 2003. ISSN 0163-1829. doi:10.1103/PhysRevB.68.054201. → page 20

[49] J. Farine. First results from EXO-200. *Nuclear Physics B - Proceedings Supplements*, 235-236:255–260, 2013. ISSN 09205632. doi:10.1016/j.nuclphysbps.2013.04.019. → page 20

[50] M. Szydagis and et al. Enhancement of NEST capabilities for simulating low-energy recoils in liquid xenon. *Journal of Instrumentation*, 8(10): C10003–C10003, 2013. ISSN 1748-0221. doi:10.1088/1748-0221/8/10/C10003. → page 21

[51] J. B. Albert and et al. Sensitivity and discovery potential of the proposed nEXO experiment to neutrinoless double- β decay. *Physical Review C*, 97 (6):1–23, 2018. ISSN 24699993. doi:10.1103/PhysRevC.97.065503. → pages 21, 27

[52] D.S. Leonard and et al. Systematic study of trace radioactive impurities in candidate construction materials for EXO-200. *Nuclear Instruments and Methods in Physics Research Section A*, 591(3):490–509, 2008. ISSN 01689002. doi:10.1016/j.nima.2008.03.001. → page 23

[53] R. Neilson and et al. Characterization of large area APDs for the EXO-200 detector. *Nuclear Instruments and Methods in Physics Research Section A*, 608(1):68–75, 2009. ISSN 01689002. doi:10.1016/j.nima.2009.06.029. → page 25

[54] nEXO collaboration, G. Gallina, and et al. Characterization of the Hamamatsu VUV4 MPPCs for nEXO. *Nuclear Instruments and Methods in Physics Research Section A*, 940:371–379, 2019. ISSN 01689002. doi:10.1016/j.nima.2019.05.096. → pages 25, 43, 106, 117, 119

[55] M. Jewell and et al. Characterization of an Ionization Readout Tile for nEXO. *Journal of Instrumentation*, 13(01):P01006–P01006, 2018. ISSN 1748-0221. doi:10.1088/1748-0221/13/01/P01006. → pages 25, 26

[56] I. Ostrovskiy and et al. Characterization of Silicon Photomultipliers for nEXO. *IEEE Transactions on Nuclear Science*, 62(4):1825–1836, 2015. ISSN 0018-9499. doi:10.1109/TNS.2015.2453932. → page 28

[57] E. Garutti. Silicon photomultipliers for high energy physics detectors. *Journal of Instrumentation*, 6(10):C10003, 2011. ISSN 1748-0221. doi:10.1088/1748-0221/6/10/C10003. → pages 28, 43

[58] A. N. Otte, D. Garcia, T. Nguyen, and D. Purushotham. Characterization of three high efficiency and blue sensitive silicon photomultipliers. *Nuclear Instruments and Methods in Physics Research Section A*, 846:106–125, 2017. ISSN 01689002. doi:10.1016/j.nima.2016.09.053. → pages 28, 62, 64, 107, 111, 117

[59] G. Gallina and et al. Characterization of SiPM Avalanche Triggering Probabilities. *IEEE Transactions on Electron Devices*, 66(10):4228–4234, 2019. doi:10.1109/TED.2019.2935690. → pages 28, 71, 80, 81, 104, 106, 132, 139

[60] F. Corsi and et al. Electrical Characterization of Silicon Photo-Multiplier Detectors for Optimal Front-End Design. *IEEE Nuclear Science Symposium Conference Record*, pages 1276–1280, 2006. ISSN 1082-3654. doi:10.1109/NSSMIC.2006.356076. → pages 28, 50

[61] F. Acerbi and et al. Silicon Photomultipliers: Technology Optimizations for Ultraviolet, Visible and Near-Infrared Range. *Instruments*, 3(1):15, 2019. doi:10.3390/instruments3010015. → page 29

[62] G.A.M. Hurkx and et al. A new analytical diode model including tunneling and avalanche breakdown. *IEEE Transactions on Electron Devices*, 39(9): 2090–2098, 1992. ISSN 00189383. doi:10.1109/16.155882. → pages 31, 114, 127, 129, 135, 136

[63] A. Ferri and et al. Performance of FBK low-afterpulse NUV silicon photomultipliers for PET application. *Journal of Instrumentation*, 11(03): P03023–P03023, 2016. ISSN 1748-0221. doi:10.1088/1748-0221/11/03/P03023. → page 32

[64] J. Rosado, V.M. Aranda, F. Blanco, and F. Arqueros. Modeling crosstalk and afterpulsing in silicon photomultipliers. *Nuclear Instruments and Methods in Physics Research Section A*, 787:153–156, 2015. ISSN 01689002. doi:10.1016/j.nima.2014.11.080. → pages 32, 60, 116, 120, 127, 143

[65] L. Fabris. *Novel readout design criteria for SiPM-based radiation detectors*. PhD thesis, Universita degli studi di Bergamo, 2015. → pages 33, 103

[66] J. Seguinot and et al. Liquid xenon scintillation: photon yield and Fano factor measurements. *Nuclear Instruments and Methods in Physics*

Research Section A, 354(2-3):280–287, 1995. ISSN 01689002. doi:10.1016/0168-9002(94)01236-9. → page 37

[67] G. Gallina and F. Retière. Characterisation of a new generation of VUV low-light sensors. *EPJ Web of Conferences*, 227, 2020. doi:10.1051/epjconf/202022702002. → page 43

[68] F. Arneodo and et al. Cryogenic readout for multiple vuv4 multi-pixel photon counters in liquid xenon. *Nuclear Instruments and Methods in Physics Research Section A*, 893:117 – 123, 2018. ISSN 0168-9002. doi:https://doi.org/10.1016/j.nima.2018.03.022. → page 44

[69] https://www.omega.com. → page 44

[70] https://www.hamamatsu.com. → pages 44, 45

[71] https://www.knightoptical.com. → page 44

[72] https://www.esourceoptics.com. → pages 44, 45

[73] https://www.newport.com. → page 44

[74] CAEN. Waveform Recording Firmware Register. https://www.caen.it/products/dt5730/. → pages 45, 52, 76, 80

[75] MIDAS Collaboration. Maximum Integrated Data Acquisition System. https://midas.triumf.ca. → pages 45, 76

[76] http://www.minicircuits.com/pdfs/MAR-6SM+.pdf, . → pages 45, 76

[77] http://www.pelhamresearchoptical.com. → page 45

[78] http://resonance.on.ca. → pages 45, 74

[79] R. Brun and F. Rademakers. ROOT. An object oriented data analysis framework. *Nuclear Instruments and Methods in Physics Research Section A*, 389(1-2):81–86, 1997. ISSN 01689002. doi:10.1016/S0168-9002(97)00048-X. → pages 50, 79, 137, 145

[80] Y. Du and F. Retiere. After-pulsing and cross-talk in multi-pixel photon counters. *Nuclear Instruments and Methods in Physics Research, Section A*, 596(3):396–401, 2008. ISSN 01689002. doi:10.1016/j.nima.2008.08.130. → page 50

[81] F. Retiere and et al. Characterization of Multi Pixel Photon Counters for T2K Near Detector. *Nuclear Instruments and Methods in Physics Research, Section A*, 610(1):378–380, 2009. ISSN 01689002. doi:10.1016/j.nima.2009.05.124. → pages 51, 105

[82] A. Ghassemi, K. Sato, and K. Kobayashi. MPPC, Hamamatsu Technical Note. https://www.hamamatsu.com/resources/pdf/ssd/mppc_kapd9005e.pdf, 2017. → page 52

[83] http://www.waynekerrtest.com/index.php. → page 53

[84] F. Acerbi and et al. Cryogenic Characterization of FBK HD Near-UV Sensitive SiPMs. *IEEE Transactions on Electron Devices*, 64(2):521–526, 2017. ISSN 0018-9383. doi:10.1109/TED.2016.2641586. → pages 56, 120

[85] A. Butcher and et al. A method for characterizing after-pulsing and dark noise of PMTs and SiPMs. *Nuclear Instruments and Methods in Physics Research Section A*, 875:87–91, 2017. ISSN 01689002. doi:10.1016/j.nima.2017.08.035. → pages 58, 59, 71, 90, 149, 151

[86] Hamamatsu Photonics. Photomultiplier Tubes, Basics and Applications . https://www.hamamatsu.com/resources/pdf/etd/PMT_handbook_v3aE.pdf, 2007. → page 62

[87] K. Yamamoto and et al. New improvements to a specialized Multi-Pixel Photon Counter (MPPC) for neutrinoless double-beta decay and dark matter search experiments. ICHEP, ID:450 https://www.hamamatsu.com/sp/ssd/microsite/MPPC/ICHEP_MPPC_panel_160731.pdf, 2016. → pages 63, 64, 67, 68

[88] https://geant4.web.cern.ch. → page 64

[89] G. Collazuol and et al. Studies of silicon photomultipliers at cryogenic temperatures. *Nuclear Instruments and Methods in Physics Research Section A*, 628(1):389–392, 2011. ISSN 01689002. doi:10.1016/j.nima.2010.07.008. → page 64

[90] E. B. Johnson and et al. Characteristics of CMOS avalanche photodiodes at cryogenic temperatures. *IEEE Nuclear Science Symposium Conference Record*, 92024:2108–2114, 2009. ISSN 10957863. doi:10.1109/NSSMIC.2009.5402104. → page 64

[91] Si EUV Photodiode Transfer Standard. https://www.nist.gov/laboratories/tools-instruments/si-euv-photodiode-transfer-standard. → page 64

[92] P. Lv and et al. Reflectance of Silicon Photomultipliers at Vacuum Ultraviolet Wavelengths. *IEEE Transactions on Nuclear Science*, 67(12): 2501–2510, 2020. ISSN 0018-9499. doi:10.1109/TNS.2020.3035172. → pages 65, 66, 67, 105

[93] C. Piemonte. A new Silicon Photomultiplier structure for blue light detection. *Nuclear Instruments and Methods in Physics Research, Section A*, 568(1):224–232, 2006. ISSN 01689002. doi:10.1016/j.nima.2006.07.018. → page 67

[94] O. Girard and et al. Characterisation of silicon photomultipliers based on statistical analysis of pulse-shape and time distributions. http://arxiv.org/abs/1808.05775, 2018. → pages 67, 88, 116, 119

[95] https://www.alionscience.com. → page 74

[96] https://osioptoelectronics.com. → page 74

[97] https://www.uniblitz.com. → page 75

[98] https://www.acktar.com. → page 75

[99] https://www.ti.com/product/OPA695, . → page 76

[100] https://www.tek.com, . → page 76

[101] https://www.keysight.com, . → page 77

[102] https://www.ti.com/product/ADS1248. → page 77

[103] W. L. Wiese and J. R. Fuhr. Accurate Atomic Transition Probabilities for Hydrogen, Helium, and Lithium. *Journal of Physical and Chemical Reference Data*, 38(3):565–720, 2009. ISSN 0047-2689. doi:10.1063/1.3077727. → page 77

[104] V. Kaufman and B. Edlén. Reference Wavelengths From Atomic Spectra in the Range 15 Å to 25000 Å. *Journal of Physical and Chemical Reference Data*, 3(4):825–895, 1974. ISSN 0047-2689. doi:10.1063/1.3253149. → page 77

[105] P. J. Naish and S. Hartwell. Exponentially Modified Gaussian functions-A good model for chromatographic peaks in isocratic HPLC? *Chromatographia*, 26(1):285–296, 1988. ISSN 00095893. doi:10.1007/BF02268168. → page 79

[106] B. Kjornrattanawanich and et al. Temperature dependence of the EUV responsivity of silicon photodiode detectors. *IEEE Transactions on Electron Devices*, 53(2):218–223, 2006. ISSN 00189383. doi:10.1109/TED.2005.862500. → pages 95, 96

[107] Marvin R. Querry and et al. Water (H2O). In *Handbook of Optical Constants of Solids*, number 2, pages 1059–1077. Elsevier, 1997. doi:10.1016/B978-012544415-6.50095-9. → page 95

[108] F. Acerbi and S. Gundacker. Understanding and simulating SiPMs. *Nuclear Instruments and Methods in Physics Research, Section A*, 926 (September 2018):16–35, 2018. ISSN 01689002. doi:10.1016/j.nima.2018.11.118. → pages 104, 124

[109] Characterization of Single-Photon Time Resolution: From Single SPAD to Silicon Photomultiplier. *IEEE Transactions on Nuclear Science*, 61(5): 2678–2686, 2014. ISSN 0018-9499. doi:10.1109/TNS.2014.2347131. → page 103

[110] F. Sun, Y. Xu, Z. Wu, and J. Zhang. A simple analytic modeling method for SPAD timing jitter prediction. *IEEE Journal of the Electron Devices Society*, 7:1–1, 2019. ISSN 2168-6734. doi:10.1109/JEDS.2019.2895151. → page 103

[111] F. Nolet and et al. Quenching Circuit and SPAD Integrated in CMOS 65 nm with 7.8 ps FWHM Single Photon Timing Resolution. *Instruments*, 2 (4):19, 2018. doi:10.3390/instruments2040019. → page 104

[112] S. Parent. Single Photon Avalanche Diodes and Vertical Integration Process for a 3D Digital SiPM using Industrial Semiconductor Technologies. In *2018 IEEE Nuclear Science Symposium and Medical Imaging Conference Proceedings (NSS/MIC)*, pages 1–4. IEEE, 2018. doi:10.1109/NSSMIC.2018.8824571. → page 104

[113] E. Engelmann. Spatially Resolved Dark Count Rate of SiPMs. *The European Physical Journal C*, 123, 2018. doi:10.1140/epjc/s10052-018-6454-0. → page 105

[114] M. Hoenk. Delta-doped back-illuminated CMOS imaging arrays: progress and prospects. In E. L. Dereniak and et al., editors, *Proc. SPIE*, volume 7419, page 74190T, 2009. doi:10.1117/12.832326. → page 105

[115] S. Nikzad and et al. High-efficiency UV/optical/NIR detectors for large aperture telescopes and UV explorer missions: development of and field observations with delta-doped arrays. *Journal of Astronomical Telescopes, Instruments, and Systems*, 3(03):1, 2017. doi:10.1117/1.JATIS.3.3.036002. → page 105

[116] T. Heindl and et al. The scintillation of liquid argon. *EPL (Europhysics Letters)*, 91(6):62002, 2010. doi:10.1209/0295-5075/91/62002. → page 105

[117] H. G. Moser and et al. Development of back illuminated SiPM at the MPI semiconductor laboratory. *Proceedings of Science*, (January), 2007. doi:10.22323/1.051.0005. → page 105

[118] C. Merck and et al. Back Illuminated Drift Silicon Photomultiplier as Novel Detector for Single Photon Counting. In *2006 IEEE Nuclear Science Symposium Conference Record*, volume 3, pages 1562–1565. IEEE, 2006. doi:10.1109/NSSMIC.2006.354196.

[119] D. R. Schuette and et al. Hybridization process for back-illuminated silicon Geiger-mode avalanche photodiode arrays. page 76810P, 2010. ISBN 9780819481450. doi:10.1117/12.849356. → page 105

[120] R. J. McIntyre. On the avalanche initiation probability of avalanche diodes above the breakdown voltage. *IEEE Transactions on Electron Devices*, 20 (7):637–641, 1973. ISSN 0018-9383. doi:10.1109/T-ED.1973.17715. → pages 105, 108, 111, 112, 113, 119, 123, 131

[121] P. P. Webb and McIntyre R. J. Properties of Avalanche Photodiodes. *RCA Review*, 35:1–5, 1974. → page 105

[122] A. Gola and et al. NUV-Sensitive Silicon Photomultiplier Technologies Developed at Fondazione Bruno Kessler. *Sensors*, 19(2):308, 2019. ISSN 1424-8220. doi:10.3390/s19020308. → page 106

[123] G. Zappalà and et al. Study of the photo-detection efficiency of FBK High-Density silicon photomultipliers. *Journal of Instrumentation*, 11(11): P11010–P11010, 2016. ISSN 1748-0221. doi:10.1088/1748-0221/11/11/P11010. → pages 106, 107

[124] C. Piemonte and et al. Performance of NUV-HD Silicon Photomultiplier Technology. *IEEE Transactions on Electron Devices*, 63(3):1111–1116, 2016. ISSN 00189383. doi:10.1109/TED.2016.2516641. → page 107

[125] F. Acerbi and et al. High Efficiency, Ultra-High-Density Silicon Photomultipliers. *IEEE Journal of Selected Topics in Quantum Electronics*, 24(2):1–8, 2018. ISSN 1077-260X. doi:10.1109/JSTQE.2017.2748927. → page 107

[126] A. Gulinatti and et al. Modeling photon detection efficiency and temporal response of single photon avalanche diodes. In *Photon Counting Applications, Quantum Optics, and Quantum Information Transfer and Processing II*, 2009. ISBN 9781424436811. doi:10.1117/12.820661. → pages 107, 110

[127] W.G. Oldham, R.R. Samuelson, and P. Antognetti. Triggering phenomena in avalanche diodes. *IEEE Transactions on Electron Devices*, 19(9): 1056–1060, 1972. ISSN 0018-9383. doi:10.1109/T-ED.1972.17544. → pages 107, 108, 121

[128] M. Mazzillo and et al. Quantum Detection Efficiency in Geiger Mode Avalanche Photodiodes. *IEEE Transactions on Nuclear Science*, 55(6): 3620–3625, 2008. ISSN 0018-9499. doi:10.1109/TNS.2008.2007483. → pages 107, 108

[129] Lumerical Solutions. Lumerical Device. http://www.lumerical.com. → page 108

[130] S. L. Miller. Ionization Rates for Holes and Electrons in Silicon. *Physical Review*, 105(4):1246–1249, 1957. ISSN 0031-899X. doi:10.1103/PhysRev.105.1246. → page 108

[131] S.M. Sze and KWOK.K.NG. *Physics of Semiconductor Devices Physics of Semiconductor Devices*, volume 10. 1995. ISBN 978-3-319-03001-2. doi:10.1007/978-3-319-03002-9. → pages 108, 112, 114, 128, 130, 132

[132] L. R. Canfield and et al. Absolute silicon photodiodes for 160 nm to 254 nm photons. *Metrologia*, 35(4):329–334, 1998. ISSN 00261394. doi:10.1088/0026-1394/35/4/19. → pages 108, 112, 113

[133] W. J. Kindt. *Geiger mode avalanche photodiode arrays: For spatially resolved single photon counting*. PhD thesis, Delft University of Technology, 1999. → page 109

[134] A. Gulinatti and et al. A physically based model for evaluating the photon detection efficiency and the temporal response of SPAD detectors. *Journal of Modern Optics*, 58(3-4):210–224, 2011. ISSN 0950-0340. doi:10.1080/09500340.2010.536590. → page 110

[135] K. Boone, Y. Iwai, F. Retière, and C. Rethmeier. Delayed avalanches in Multi-Pixel Photon Counters. *Journal of Instrumentation*, 12(07): P07026–P07026, 2017. ISSN 1748-0221. doi:10.1088/1748-0221/12/07/P07026. → pages 110, 119

[136] A. G. Martin. Self-consistent optical parameters of intrinsic silicon at 300 k including temperature coefficients. *Solar Energy Materials and Solar Cells*, 92:1305–1310, 2008. ISSN 0927-0248. doi:10.1016/j.solmat.2008.06.009. → pages 113, 117, 142

[137] M. Biroth and et al. An analytical approach to predict fundamental cryogenic properties of silicon photomultipliers. ICASIPM, https://indico.gsi.de/event/6990/session/9/contribution/22/material/slides/0.pdf, 2018. → page 113

[138] R. J. McIntyre. Theory of Microplasma Instability in Silicon. *Journal of Applied Physics*, 32(6):983–995, 1961. ISSN 0021-8979. doi:10.1063/1.1736199. → pages 113, 114, 115

[139] M. Biroth and et al. Modeling and Characterization of SiPM Parameters at Temperatures between 95 K and 300 K. *IEEE Transactions on Nuclear Science*, 64(6):1619–1624, 2017. ISSN 00189499. doi:10.1109/TNS.2017.2695405. → page 114

[140] G.A.M. Hurkx. On the modelling of tunnelling currents in reverse-biased p-n junctions. *Solid-State Electronics*, 32(8):665–668, 1989. ISSN 00381101. doi:10.1016/0038-1101(89)90146-9. → page 127

[141] G.A.M. Hurkx and et al. A new recombination model describing heavy-doping effects and low-temperature behaviour. *International Technical Digest on Electron Devices Meeting*, pages 307–310, 1989. ISSN 0163-1918. doi:10.1109/IEDM.1989.74285. → pages 127, 128

[142] G.A.M. Hurkx and et al. A New Recombination Model for Device Simulation Including Tunneling. *IEEE Transactions on Electron Devices*, 39(2):331–338, 1992. ISSN 15579646. doi:10.1109/16.121690. → page 130

[143] D. Neamen. *Semiconductor Physics And Devices*. McGraw-Hill Series in Electrical and Computer Engineering. McGraw-Hill Education, 2003. ISBN 9780072321074. → pages 130, 144

[144] P. U. Calzolari and S. Graffi. A theoretical investigation on the generation current in silicon p-n junctions under reverse bias. *Solid-State Electronics*, 15(9):1003–1011, 1972. ISSN 00381101. doi:10.1016/0038-1101(72)90143-8. → page 130

[145] F. Acerbi and et al. Silicon photomultipliers and single-photon avalanche diodes with enhanced NIR detection efficiency at FBK. *Nuclear Instruments and Methods in Physics Research, Section A*, (2017), 2017. ISSN 01689002. doi:10.1016/j.nima.2017.11.098. → pages 132, 143, 146

[146] D. J. Massey and et al. Temperature Dependence of Impact Ionization in Submicrometer Silicon Devices. *IEEE Transactions on Electron Devices*, 53(9):2328–2334, 2006. ISSN 0018-9383. doi:10.1109/TED.2006.881010. → page 137

[147] J. Van Zeghbroeck. *Principles of Semiconductor Devices*. Bart Van Zeghbroeck, 2011. URL https://books.google.ca/books?id=hw3YtwEACAAJ. → page 137

[148] R. Mirzoyan and et al. Light emission in Si avalanches. *Nuclear Instruments and Methods in Physics Research Section A*, 610(1):98–100, 2009. ISSN 01689002. doi:10.1016/j.nima.2009.05.081. → page 142

[149] M. L. Knoetig and et al. SiPM Avalanche Size and Crosstalk Measurements with Light Emission Microscopy. *IEEE Transactions on Nuclear Science*, 61(3):1488–1492, 2014. ISSN 0018-9499. doi:10.1109/TNS.2014.2322957. → page 142

[150] I. Rech and et al. Optical crosstalk in single photon avalanche diode arrays: a new complete model. *Optics Express*, 16(12):8381, 2008. ISSN 1094-4087. doi:10.1364/OE.16.008381. → page 143

[151] I. Rech and et al. A New Approach to Optical Crosstalk Modeling in Single-Photon Avalanche Diodes. *IEEE Photonics Technology Letters*, 20 (5):330–332, 2008. ISSN 1041-1135. doi:10.1109/LPT.2007.915654. → page 143

[152] A. Para. Afterpulsing in Silicon Photomultipliers: Impact on the Photodetectors Characterization. *Journal of Instrumentation*, 9(10):

T10004–T10004, 2014. ISSN 1748-0221.
doi:10.1088/1748-0221/9/10/T10004. → pages 147, 150

[153] Y. Du and F. Retière. After-pulsing and cross-talk in multi-pixel photon counters. *Nuclear Instruments and Methods in Physics Research, Section A*, 596(3):396–401, 2008. ISSN 01689002.
doi:10.1016/j.nima.2008.08.130. → page 150